Università degli Studi Roma Tre
Dipartimento di Matematica e Fisica

Corso di Laurea in Fisica

Tesi di Laurea Magistrale in Fisica

Design and characterization of the UV-extended custom SiPM arrays for the Mu2e electromagnetic calorimeter

–

Relatore interno:
Prof. Fabrizio Petrucci

Candidata:
Eleonora Diociaiuti

Relatore esterno:
Dott. Stefano Miscetti

Anno Accademico 2015/2016

A mamma e papà

Contents

Introduction

In this thesis, the simulations and tests carried out for the optimization and design of the electromagnetic calorimeter of the Mu2e (Muon to electron conversion) experiment are presented.
Mu2e is a proposed experiment, hosted in the the Muon Campus of the Fermi National Accelerator Laboratory (FNAL) in Batavia, United States, that proposes to measure the ratio between the rate of the neutrinoless conversion of muons into electrons in the field of a nucleus and the rate of ordinary muon capture on the nucleus:

$$R_{\mu e} = \frac{\Gamma\left(\mu^- N \rightarrow e^- N\right)}{\Gamma\left(\mu^- N \rightarrow \text{all captures}\right)} \tag{1}$$

The signature of this process is a mono-energetic electron with an energy nearly equivalent to the muon rest mass. Mu2e should collect 7.52×10^{17} stopped muons in three years of running, with the goal of improving the result of previous generation experiments (SINDRUM II) by a factor of 10^4 (from $R_{\mu e} < 7\times10^{-13}$ to $R_{\mu e} < 6\times10^{-17}$).
In July 2016, the Mu2e experiment has received the US Department of Energy (DOE) Critical-Decision 3 (CD-3) approval that indicates the start of the construction period. The experiment should start data taking in 2020.
This thesis is organized in 7 chapters.
In the first chapter, a recollection of the physics motivations for the searches of CLFV processes ($\mu \rightarrow e\gamma,\ \mu\, N \rightarrow e\, N, \mu \rightarrow 3e$) with muons is presented.
In the second chapter, the measurements of the negative muon conversion process is addressed focusing on its distinctive signature and on the expected background.
In the third chapter, the experimental technique developed by Mu2e is explained and compared to recent CLFV search experiments. An overall description of the experimental setup is then given introducing the Superconducting Solenoid Magnetic System and its different components: the Production, the Transport and the Detector solenoids.
In the fourth chapter, the requirements and the technical choices for the electromagnetic calorimeter are discussed, focusing on its particle identification and background rejection capabilities.

The fifth chapter is devoted to the different typologies of silicon photosensor with a particular focus on the Silicon Photomultipliers (SiPMs).
In the sixth chapter, the results from a test beam performed, during 2015 at the Beam Test Facility (BTF) in LNF, on a crystal matrix prototype read out by SiPMs are reported.
The original part of this thesis is concentrated in the seventh chapter where my contribution on SiPMs and crystals tests is reported. First of all the measurements of the SiPM I-V curves and the breakdown voltage are addressed. Due to the possibility to discriminate a single photoelectron with a properly amplified SiPM, its gain has also been measured. Moreover, the results from the neutron irradiation campaign carried out at the HZDR Zentrum in Dresden are reported. The observed increase of the current drawn by the irradiated SiPM suggested that, in order to meet the fixed requirements, sensors will need to be cooled down during the data taking. Finally, the measurements carried out to characterize the crystals are reported.

Chapter 1

Charged Lepton Flavor Violation

1.1 The Standard Model

A complete description of the elementary particle physics and of their interactions is possible in term of a well-defined gauge theory, the Standard Model (SM) [1]. It is a non-abelian gauge theory incorporating quantum electrodynamics, Glashow-Weinberg-Salam theory of electroweak processes and quantum chromodynamics. The SM is based on the gauge symmetry group $SU(3)_C \times SU(2)_L \times U(1)_Y$, where the index C stands for color charge, L refers to the fact that $SU(2)_L$ only acts on the left handed components of the fields and Y refers to the hypercharge.
The two building blocks of the matter are quarks and leptons. These sub-atomic particles are 1/2-spin fermions, arranged into three "families", or generations, as shown in Table 1.1.
Each family contains three color replicas of the weakly charged doublets of quarks

Electric charge	First Generation	Second Generation	Third Generation
+2/3	u	c	t
-1/3	d	s	b

Particle	Generation	Electric charge	Lepton flavor number (L_i)
e^-	I	-1	$L_e = 1$
ν_e	I	0	$L_e = 1$
μ^-	II	-1	$L_\mu = 1$
ν_μ	II	0	$L_\mu = 1$
τ^-	III	-1	$L_\tau = 1$
ν_τ	III	0	$L_\tau = 1$

Table 1.1: *Quarks and leptons in the SM*

and a colorless weakly charged doublet containing a neutrino and a charged lepton. The 1-spin force carriers are the photon γ, which mediates the electromagnetic force, the W^+,W^- and Z^0 gauge bosons of the weak interactions and eight gluons g, which mediate the strong interactions.
In order to explain the spontaneous breaking of the $SU(2)_L \times U(1)_Y$ electroweak sector, which give origin to the $U(1)_{EM}$, the Higgs mechanism is introduced.
Starting from the '70s until now, the SM explained most of the known phenomena in particle physics, including the discovery of the Higgs Boson at the LHC at CERN in 2012 [2] [3]. However it incorporates only three out four fundamental forces (gravity is not included) and cannot explain neutrino masses. This means that the Standard Model is not yet a complete theory.

1.2 Charged Lepton Flavor Violation (CLFV)

1.2.1 LFV, CLFV and Neutrino masses

Before the discovery of neutrino oscillations, lepton flavor changing processes were forbidden in the Standard Model and lepton flavor numbers L_e, L_μ and L_τ were considered as conserved. In the SM the lepton flavor has a value of +1 for the leptons and −1 for the antileptons, i.e. the muons has $L_\mu = 1$ and L_e, $L_\tau = 0$. In this scenario the unitary matrix Pontecorvo-Maki-Nakagawa-Sakata (PMNS), which relates weak eigenstates with mass eigenstate, is diagonal:

$$\begin{pmatrix} \nu_e \\ \nu_\mu \\ \nu_\tau \end{pmatrix} = V_{PMNS} \begin{pmatrix} \nu_1 \\ \nu_2 \\ \nu_3 \end{pmatrix} \tag{1.1}$$

A possible parametrization of the V_{PMNS} is now reported:

$$V_{PMNS} = \begin{pmatrix} 1 & 0 & 0 \\ 0 & c_{23} & s_{23} \\ 0 & -s_{23} & c_{23} \end{pmatrix} \begin{pmatrix} c_{13} & 0 & s_{13}e^{-i\delta} \\ 0 & 1 & 0 \\ -s_{13}e^{+i\delta} & 0 & c_{13} \end{pmatrix} \begin{pmatrix} c_{12} & s_{12} & 0 \\ -s_{12} & c_{12} & 0 \\ 0 & 0 & 1 \end{pmatrix} \tag{1.2}$$

In 1998 the Super Kamiokande experiment [4] showed for the first time the existence of $\nu_\mu \rightarrow \nu_\tau$ oscillations in the sector of the atmospheric neutrinos.
Combining these results with others from solar, beam and reactor experiment, a clear evidence of the existence of oscillation in flight between different flavors of neutrinos (and antineutrinos) was proven. In the Standard Model neutrinos and antineutrinos are described respectively by chiral left-handed and right-handed eigenstates, but allowing the possibility of flavor oscillation ($P(\nu_\mu \rightarrow \nu_\tau) \neq 0$) a super-position of mass

eigenstates is produced. Hence, neutrino oscillations represent an evidence of Lepton Flavor Violation (LFV), whose rate are obtained from the PMNS matrix.
Instead, the rate of Charged Lepton Flavor Violation (CLFV) processes is model dependent. An example is provided by the minimal extension to the Standard Model (SME), where neutrino masses are generated by introducing three right-handed SU(2) singlet fields and three new Yukawa couplings. Let us consider the CLFV $\mu \to e\gamma$ process, reported in Figure 1.1. IN SME its branching ratio is negligible, because the amplitude is proportional to the neutrinos mass-squared differences:

$$BR(\mu \to e\gamma) = \frac{3\alpha}{32\pi}\left|\sum_{i=2,3} U^*_{\mu i} U_{ei} \frac{\Delta m^2_{1i}}{M^2_W}\right| < 10^{-54} \tag{1.3}$$

where $U^*_{\mu i}$ and U_{ei} are elements of the PMNS matrix, Δm^2_{1i} are the neutrino mass-squared and M_W the W-boson mass. In this extension similar results are obtained for

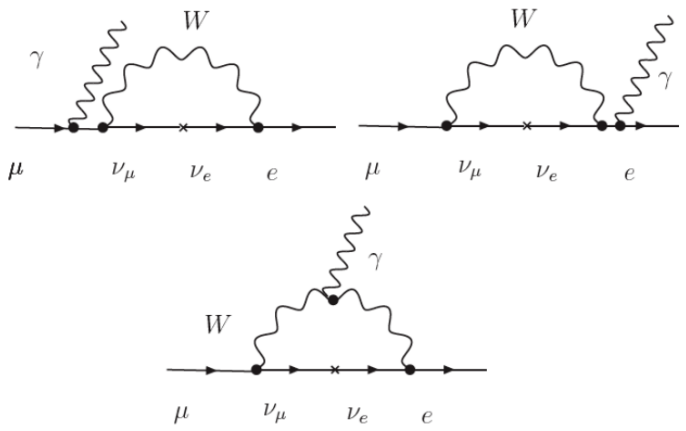

Figure 1.1: *Feynman diagram for the $\mu \to e\gamma$ (in the minimal extended Standard Model).*

the $\mu^- N \to e^- N$ conversion process. However, in several alternative New Physics scenarios, much higher rates are expected for CLFV processes, with values that could be measured with values that could be measured by current and next generation experiments.

1.2.2 CLFV in muon decays

Indipendent model Lagrangian extension

In 1937, when the muon was discovered, it was believed to be the Yukawa meson. Soon afterwards, however, the leptonic nature of the muons was proved since its lifetime was too long and its interaction cross section too weak. Morevover, it was believed that the muon was an excited state of the electron and therefore could become

de-excited by emitting photons. If this hypothesis were correct, the muon would decay into an electron and a photon. Experimental searches by Hincks and Pontecorvo (1948) did not observe the process $\mu \rightarrow e\gamma$ but set an upper limit on the $BR < 10\%$. Since the concept of flavor was not introduced yet, it was supposed that muon could decay into an electron and two other identical neutral particles: the neutrinos.
Several experiments tried to observe muon to electron neutrinoless conversion but the results have never been positive: the concept of lepton flavor conservation was thus introduced for these two particles, and then extended to the τ lepton.
In addiction, muons are the most sensitive probes to CLFV processes because of their long life time ($\approx 2.2\mu$s) and because they are relatively easy to produce. In Figure 1.2 the experimental limits of the most studied processes, that is $\mu \rightarrow e\gamma$, $\mu \rightarrow eee$ and $\mu N \rightarrow eN$ are reported. The experimental sensitivity improved with time as long as new experiments were conducted. In the same figure the expected sensitivity for next generation experiments is also shown. For the conversion process, the current upper

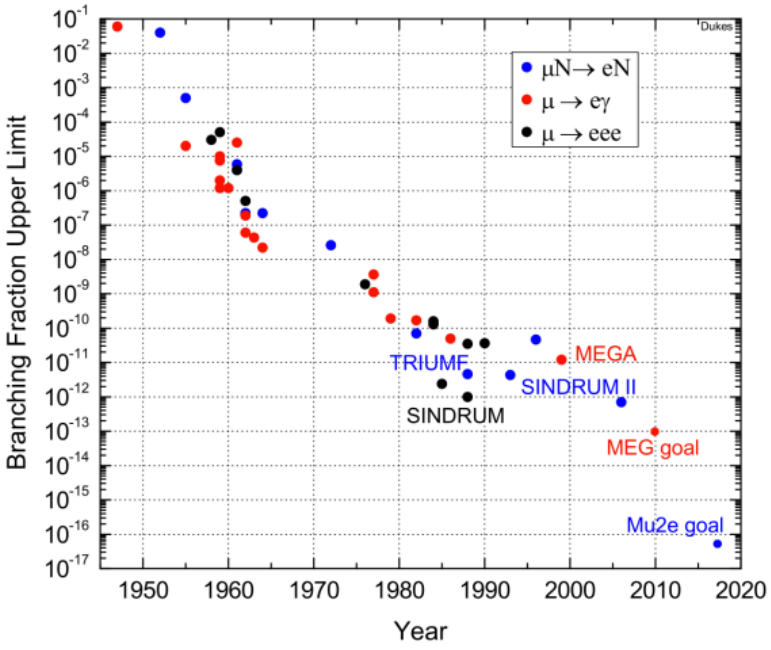

Figure 1.2: *CLFV processes search with muons.*

limit has been set by the SINDRUM II experiment in 2006 at PSI:

$$BR(\mu^- Au \rightarrow e^- Au) < 7 \times 10^{-13}, @90\%\ CL \tag{1.4}$$

1.3 CLFV Independent Lagrangian and New Physics models

It is possible to estimate the sensitivity of CLFV processes to new physics in a model-indipendent way adding to the Standard Model Lagrangian effective operators, which violate lepton flavor [5]:

$$\mathcal{L}_{CLFV} = \frac{m_\mu}{(1+\kappa)\Lambda^2}\overline{\mu}_R\sigma_{\mu\nu}e_L F^{\mu\nu} + \frac{\kappa}{(1+k)\Lambda^2}\overline{\mu}_L\gamma_\mu e_L\left(\sum_{q=u,d}\overline{q}_L\gamma^\mu q_L\right) \tag{1.5}$$

this effective Lagrangian is a sum of "loop" and "contact" terms. L, R indicate the chirality of the different Standard Model fermion fields, $F_{\mu\nu}$ is the photon field strength and m_μ is the muon mass.
The cofficents of the two types of operators are parameterized by two independent constants: the Λ parameter, with dimensions of mass, which is meant to represent the effective mass scale of the new degrees of freedom, and the dimensionless parameter κ, which governs the relative size of the two different types of operators. The first one is the magnetic field operator, which mediates directly process such as $\mu \to e\gamma$ and at order α $\mu \to eee$ and $\mu N \to eN$, and the second one is the four-fermion operator, which mediates at the leading order muon into electron conversion and $\mu \to eee$ (Figure 1.3).

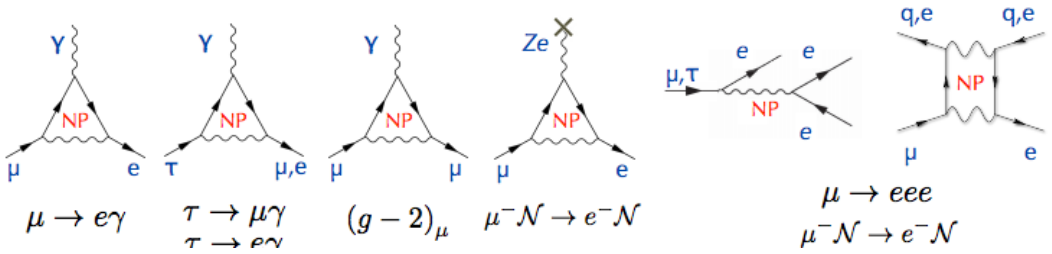

Figure 1.3: *Representation of the vertices and interactions of some CLFV processed, which NP contribution could be measurable. The first four diagrams are madiated by magnetic field operators while the latter two by four-fermion operator.*

Considering $\kappa << 1$, the first term, containing the flavor-changing magnetic moment operator, is dominant; if $\kappa >> 1$, the second term, the four-fermion interaction operator, is dominant. The first term arises from loops with an emitted photon (real in $\mu \to e\gamma$ and virtual in the other two cases) and can mediate all three rare muon processes. The second term includes contact terms and a variety of other processes not resulting in an on-mass-shell photon. Therefore, $\mu N \to eN$ and $\mu \to eee$ processes

are sensitive to New Physics regardless of the relative contributions of the first and second terms.
In Figure 1.4, areas of the $\Lambda - \kappa$ plane, as explored by several experiments (MEG for $\mu \rightarrow e\gamma$ and Mu2e for μ conversion), are shown.
The MEG experiment, for example, will probe Λ up to 1000-2000 TeV for $\kappa \ll 1$, but

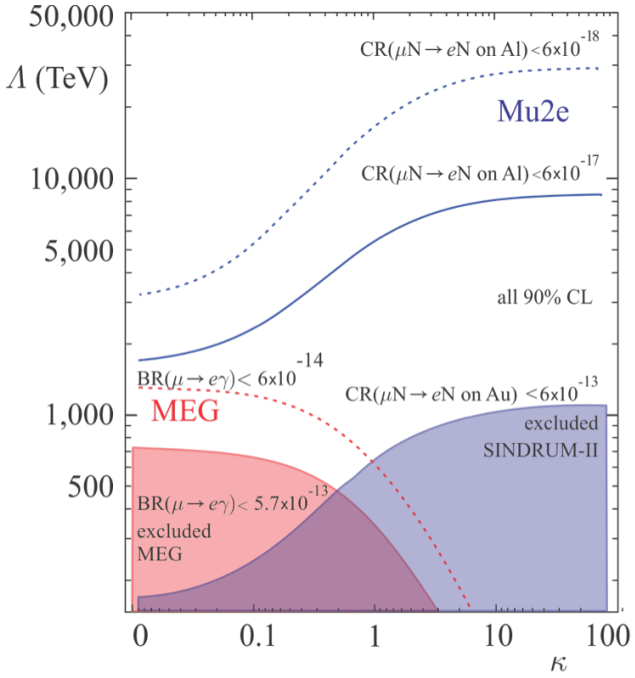

Figure 1.4: *Current and future limits expected for $\mu N \rightarrow eN$ process as a function of Λ and κ.*

its sensitivity is lower considering $\kappa \gg 1$. On the other hand the Mu2e experiment will test Λ values from 2000 up to 10000 TeV over all values of κ.
Λ is not immediately comparable to the mass scale reach of direct searches: considering a magnetic momentum interaction, the mass M is related to Λ by the expression:

$$\frac{1}{\Lambda^2} \propto \frac{g^2 e}{16\pi^2 M^2} \tag{1.6}$$

where e is the electromagnetic coupling constant. Considering the four-fermion operator the relation is:

$$\frac{1}{\Lambda^2} \propto \frac{g^2}{M^2} \tag{1.7}$$

where g is the weak interaction coupling constant. The mass M accessible studying CLFV processes is above the one that can be reached at LHC. This implies that the CLFV importance is independent from possible future discovery at the TeV scale.

Moreover, an observation of New Physics at LHC will correspond to a precise measurement both at MEG and Mu2e, thus helping to identify the underlying theory responsible of the process. Moreover, if MEG observes a signal, Mu2e should as well, helping to constrain Λ and κ. A null result from MEG, on the other side, does not preclude a Mu2e discovery.

CLFV and the New Physics Models

The discovery of a lepton number violating process, but also a better constraint on the Branching Ratio, could give strong indications on which New Physics model is preferred.
Some examples of NP models and their effect on CLFV process are reported in the following.

SO(10) SUSY Grand Unified Model: The supersymmetric version of the Standard Model with weak-scale supersymmetry (SUSY)-breaking parameters lead to large rates for CLFV processes. For example it is possible to relate the $\mu^- N \rightarrow e^- N$ rate in titanium as a function of SO(10) SUSY GUT breaking parameter [7], taking into account θ_{13} value and Higgs mass with different hypothesis of the neutrino Yukawa couplings, as shown in Figure 1.5.
The red vertical lines represent the present limit given by MEG , the expected result for the MEG upgrade (dashed) and the expected result for a conceptual $\mu \rightarrow e\gamma$ experiment. Horizontal black lines, instead, represent limit on μ-to-e conversion rate from SINDRUM II result and Mu2e/COMET planned results. Project X, now PIP-II, is a set of still conceptual experiments working with a beam improved by a factor 10 in intensity currently under study at Fermilab. SUSY, in fact, predict a muon-to-electron conversion through a penguin diagram with two sleptons in the loop, as reported in Figure 1.6. In particular in the SUSY model a slepton is in the loop and a chargino exchanges a photon with the nucleus, while in heavy neutrino model an heavy neutrino is in the loop and a W boson exchanges a photon with the nucleus.

Higgs-induced flavor violation: Some New Physics models includes LFV processes induced by Higgs exchange. Compared to $\mu \rightarrow e\gamma$ and $\mu \rightarrow eee$, muon conversion is more sensitive because of the Yukawa couplings result smaller in the first two cases [8]. As shown in the right side of the Figure 1.7 a tree-contribution involving light quark or a loop-induced effect of heavy quarks to the gluons can induce the conversion.

The muon conversion in nucleus is also the most sensitive channel for the study

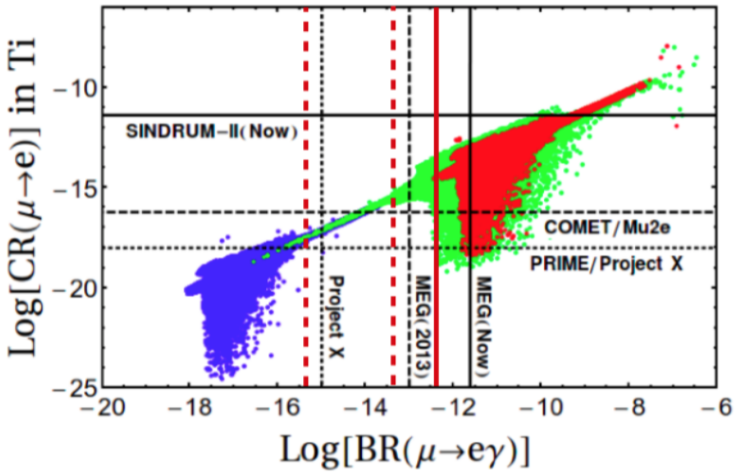

Figure 1.5: *Muon Conversion Rate CR$\mu \rightarrow e$)in Titanium as a function of the BR($\mu \rightarrow e\gamma$) for the PMNS-like neutrino Yukawa coupling in mSUGRA (red), Non Universal Higgs Mass (green) and for CKM-like neutrino Yukawa coupling (blue) for tan$\beta = 10$.*

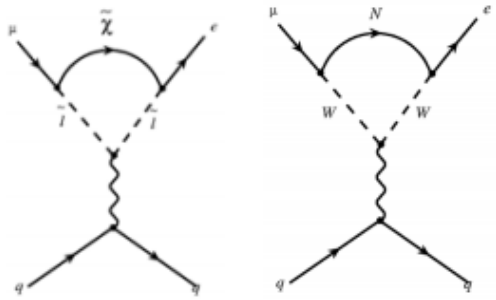

Figure 1.6: *Feynman diagram for the $\mu N \rightarrow eN$ process in the SUSY (right) and heavy netrino (right) model.*

of Yukawa couplings $|Y_{mue}|$ and $|Y_{e\mu}|$. In the left side of the Figure 1.7 the thin blue dashed lines are contours of constant BR($h \rightarrow \mu e$), while the thick red line is the projected Mu2e limit.

Littlest Higgs model with T-parity (LHT): The Higgs boson is considered an exact Goldstone boson under several symmetries. In the Littlest Higgs model with T-parity (LHT), the Higgs boson is considered an exact Goldstone boson under several symmetries. Only if the symmetries are all broken (collective symmetry breaking, CSB), the Higgs pick up a contribution to its mass. To avoid fine tuning from electroweak precision data, a discrete symmetry (analogous to SUSY) and called T-parity, is introduced. The scanning of the parameters of this model provides measurable BR

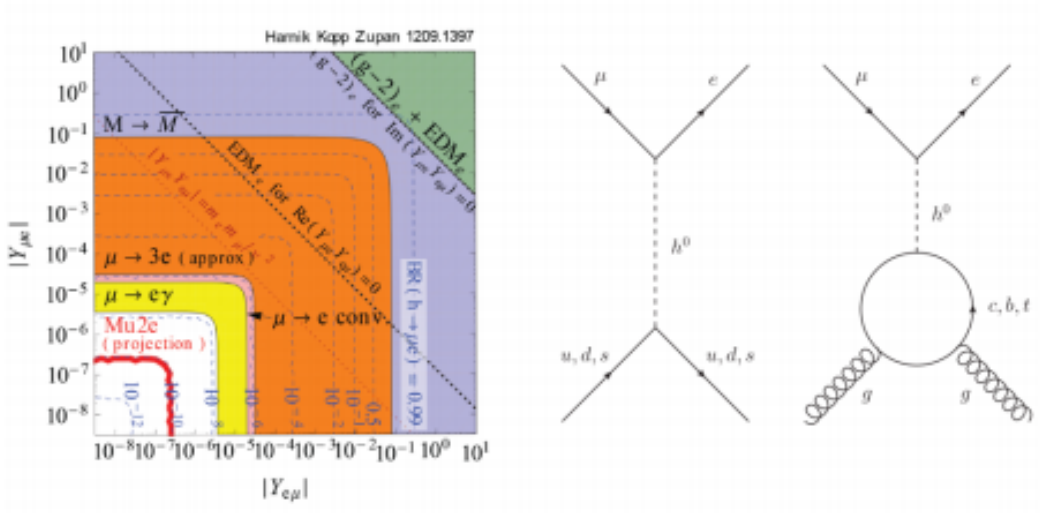

Figure 1.7: *Left: constraints on the flavor-violating Yukawa couplings a 125 GeV Higgs boson. Right: Higgs-induced LFV for a muon conversion.*

both for $\mu \to e\gamma$ and for $\mu N \to eN$ [9]. In Figure 1.8 the blue line represents the MSSM dipole contribution, the solid green lines are the present (solid) and expected (dashed) upper limits by MEG and the yellow solid line is the SINDRUM II upper limit. Mu2e would cover all the parameters of this scan and in case of no observation the validity of this theory will be negligible.

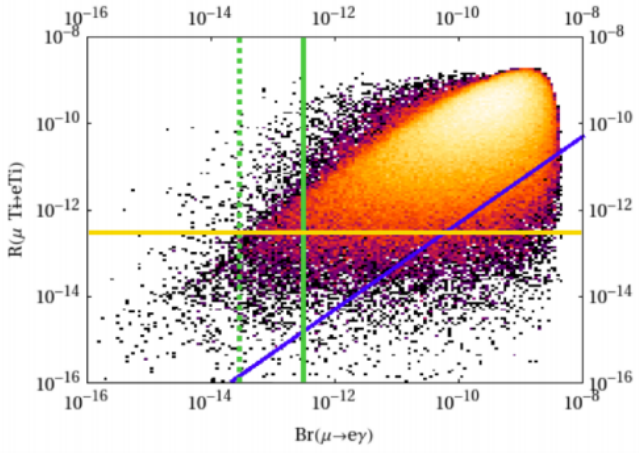

Figure 1.8: *Correlation between $\mu \to e\gamma$ and $\mu \to e$ conversion in Titanium obtained from a general scan over the LHT parameters.*

Scalar Leptoquark model: Models with scalar leptoquarks at the TeV scale can,

through top mass enhancement, modify the $\mu \rightarrow$ e conversion rate and BR ($\mu \rightarrow e\gamma$) while satisfying all known experimental constraints from collider and quark flavor physics. In Figure 1.9 the reachs in the new coupling λ for a range of scalar leptoquark masses are compared for the $\mu \rightarrow e$ conversion rate with the sensitivity of Mu2e and BR($\mu \rightarrow e$) at the sensivity of the MEG upgrade.

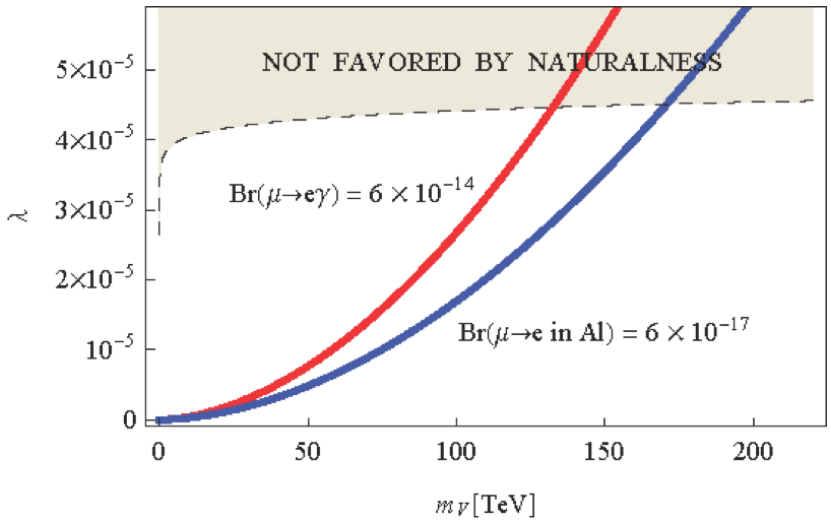

Figure 1.9: *The combination of couplings λ as a function of the scalar leptoquark mass for the $\mu \rightarrow e$ conversion rate (CR) in Al at the sensitivity of Mu2e and BR($\mu \rightarrow e$) at the sensitivity of the MEG upgrade.*

Heavy neutrinos: Neutrino oscillation provides the first proof of CLFV interactions. However, rates for CLFV processes are not immediately related to neutrino masses, because they strongly depends on the undergoing mechanism. The presence of new heavy neutrino mass states, different from mass eigenstates ν_1, ν_2, ν_3, is related to a muon conversion process through the neutrino oscillation in Feynman loop reported in Figure 1.6.

Left-Right Symmetric Models: Left-Right symmetric models are extensions of the Standard Model useful to restore parity at short distances. A recent study [11] predicts the high CLFV rates assuming a new mass breaking scale at around 5 TeV. From the correlation between the BR for the MEG upgrade and $R_{\mu e}$ for Mu2e it is possible to cover the full phase space of this theory: as shown in Figure 1.10 the observation of $\mu \rightarrow e\gamma$ with a branching ratio of 10^{-13} would imply a muon-to-electron conversion rate around of 10^{-14}, and then several hundreds of events in the Mu2e experiment. The red and magenta shaded regions are constrained by MEG

and SINDRUM-II respectively and the vertical and horizontal dashed lines indicate projected limits from the MEG upgrade and Mu2e/COMET.

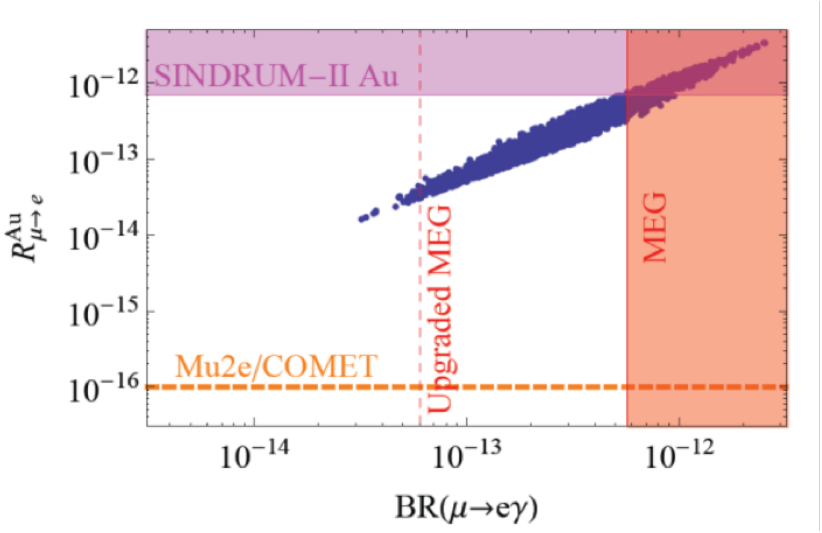

Figure 1.10: *Correlation between the branching ratio for $\mu \to e\gamma$ and the muon-to-electron conversion rate in gold in a left-right symmetric model.*

Chapter 2

Negative muon conversion: signal and backgrounds

The aim of the Mu2e experiment is the search of the conversion of a muon to an electron in the field of a nucleus. This is a coherent process since the muon recoils off the entire nucleus, that can be studied using the kinematic of a two-body decay. In the Mu2e experiment, muons are fired at a thin Al target, where they are stopped and form muonic atoms with the muons rapidly cascading down to the 1S state [12]. Radiative capture, decay or eventually conversion of the muon takes place with a mean lifetime that has been measured in various materials and ranges from less than ~ 100 ns (high-Z nuclei) to over~ 2 μs (low-Z nuclei).
Given that the mass of a nucleus is large compared to that of the electron, the recoil terms are small and the conversion electron is therefore mono-energetic with an energy slightly less than the muon rest mass:

$$E_e = m_\mu c^2 - E_b(Z) - \frac{E_\mu^2}{2m_N} \tag{2.1}$$

where Z and A are the number of protons and nucleons in the nucleus,
$E_b \simeq Z^2\alpha^2 m_\mu/2$ is the atomic binding energy of the muon and $E_\mu = m_\mu - E_b$ is the nuclear recoil energy. Considering the muonic aluminum $E_e = 104.97$ MeV and the muon life time is 864 ns [13].

The Mu2e experiment will measure the quantity:

$$R_{\mu e} = \frac{\Gamma\left(\mu^- N \rightarrow e^- N\right)}{\Gamma\left(\mu^- N \rightarrow \text{all captures}\right)} \tag{2.2}$$

that is the conversion rate of the μ-e coherent conversion process in a nucleus field, which is defined as the ratio of muon conversion events normalized to the number

of muon captures. This normalization is used in order to cancel many details of the nuclear wavefunction [14].

There are many processes that can mimic the muon-to-electron conversion experimental signature, in particular:

- Intrinsic processes scaling with beam intensity like muon decay in orbit (DIO) and radiative muon capture (RMC).
- Processes that are delayed because of particles that spiral slowly down the muon beam line, such as antiprotons.
- Prompt processes where the detected electron is nearly coincident in time with the arrival of a beam particle at the muon stopping target (radiative pion capture, RPC).
- Electrons or muons initiated by cosmic rays.
- Events resulting from reconstruction errors induced by additional activity in the detector from conventional processes.

2.1 Muon decays in orbit (DIO)

Muon decay in orbit represents one of the most important background source for the $\mu^- N \to e^- N$ process. Differently from the free muon decay, where the electron energy would not exceed 52.8 MeV, when the electron and two neutrinos are emitted in opposite directions, in a DIO the outgoing electron can exchange momentum with the Al nucleus and have, with very small probability, a maximum energy close to the one of the conversion electron. The DIO energy spectrum has been calculated in [15] and is reported in Figure 2.1. The nuclear recoil slightly distorts the Michel peak and originates the small tail that extends out to the conversion energy. Looking at the DIO spectrum on a log scale, it can be seen that the occurrence of DIO electrons above 100 MeV is still at an appreciable level and is relevant when compared to a signal with a branching ratio of $\mathcal{O}(10^{-17})$.
To date, there are no measurements of DIO spectrum near the conversion electron energy, because of the high muon rate needed. However, a recent theoretical calculation [12], which takes into account nuclear effects, gives an uncertainty near the endpoint smaller than 20%.

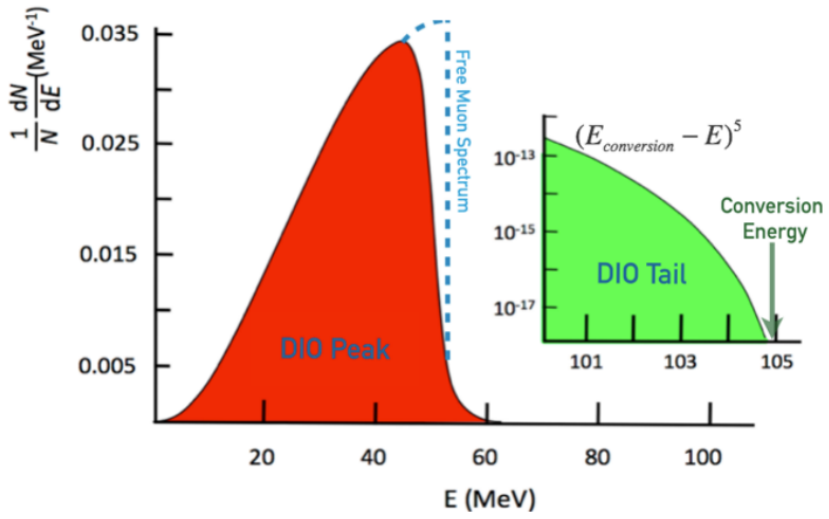

Figure 2.1: *Electron energy spectrum from muon DIO in aluminum. The dotted line represent the spectrum of the free muon decay.*

2.2 Radiative muon capture (RMC)

The muon can be absorbed by the nucleus of the target, emitting a high energy photon through :

$$\mu\, N(Z,A) \rightarrow \gamma\ \nu_\mu\, N(Z-1,A) \tag{2.3}$$

these photons that can convert to an electron-positron pair in the stopping target or other surrounding material, producing an electron near the conversion electron energy. It is possible to reduce the impact of this process choosing the target material, to ensure that the photon energy is below the conversion electron energy. For example the RMC endpoint energy is 101.9 MeV, about 3.1 MeV below the conversion electron energy.

2.3 Radiative pion capture (RPC)

Pions can produce background through the capture by the nucleus:

$$\pi^-\, N\ \rightarrow \gamma N* \tag{2.4}$$

the kinematical endpoint is near the pion rest mass energy with a broad distribution that peaks at about 110 MeV. If the photon then converts, an electron-positron pair is produced and in the case of an asymmetric conversion, the outgoing electron can be near the conversion energy and mimic a conversion electron. It has to be noted that the pion has a a lifetime smaller than few tens of ns, while the bound muon has a

mean lifetime of the order of several hundreds of ns. The RPC background is reduced using a pulsed proton beam and searching for the conversion electrons at delayed time when virtually all pions have been decayed or annihilated in the material.

2.4 Cosmic rays

Particles like muons, electrons and photons from cosmic rays can be considered as a source of background for the muon-to-electron conversion search. If they have trajectories that appear to originate in the stopping target they can fake a muon conversion electron. To remove this background an incoming cosmic ray is identified and rejected using a passive shielding and veto counters. This background scales with the signal time window and not with the beam intensity.

2.5 Antiprotons

Antiprotons, which can be generated along with the muons by the parent proton beam or by cosmic rays, can be coincident in time with a conversion electron, mimicking the energy of a conversion electron signal. The products of their interaction with the matter can be also a source of background.

2.6 Mis-recontruction and environmental backgrounds

Track reconstruction can be affected by the presence of spurious hits in the detector, causing tails in the energy resolution response function. Thus, low-energy DIO electrons can possibly move into the signal momentum window. Muon beam, multiple DIO electrons within a narrow time window, emission of photons from RMC, neutrons and protons can originate additional the hits in the tracking detector, spoiling the resolution. A detailed detector simulation is used to estimate the background level including these effects on the energy resolution. The rate of background activity scales linearly with beam intensity. Systematic uncertainties are assigned to account for the uncertainties in the rate of this background activity.

Chapter 3

The Mu2e experiment

The goal of the Mu2e experiment is to search for the neutrinoless, coherent conversion of muons into electrons in the field of a nucleus and improve of four orders of magnitude the previous sensitivity set by SINDRUM II experiment [16] ($R_{\mu e} = 7 \times 10^{-13}$). This corresponds to a limit on the ratio between the conversion and nuclear muon capture rates $R_{\mu e}$ of :

$$R_{\mu e} < 6 \times 10^{-17} \text{ @ 90\% C.L} \tag{3.1}$$

that is equivalent to a Single Event Sensitivity (SES) of $(2.69 \pm 0.04) \times 10^{-17}$. The SES is defined as that conversion rate for which, considering 3.6×10^{20} Proton On target (POT) and 6.7×10^{17} stopped muons, the expected number of events will be one[1].

3.1 Comparison with other recent experiments

For the $\mu \rightarrow e\gamma$ reaction, the most recent results are provided by the MEG experiment which is planning to start a new run with an upgraded apparatus in 2017. The SINDRUM II experiment has set the best upper limit for the muon-to-electron coherent conversion. COMET, a Mu2e analogous experiment, is in a development phase at J-PARC, aiming to reach a similar sensitivity.

3.1.1 The MEG experiment

The MEG experiment, built at Paul Scherrer Institute (PSI) in Villigen, Switzerland, searchs for the lepton flavor violating muon decay, $\mu \rightarrow e\gamma$ with a sensitivity of $\sim 4 \times 10^{-13}$ [17]. The PSI provides the world most intense continuous muon beams

[1] Considering the product of efficiency × acceptance of k =13% and the fraction of muons that decays, it is obtained that SES×k×muon stopped×0.4=0.999908.

delivering a μ^+ beam, with an intensity of $\sim 3\times10^7\,\mu^+/s$, on a thin target where they stop and decay at rest. The experimental signature is the back-to-back emission and in time coincidence of positron and a photon both of energy equals to 53 MeV ($m_\mu/2$).

A schematic of the MEG apparatus is shown in Figure 3.1 [18]: a superconducting

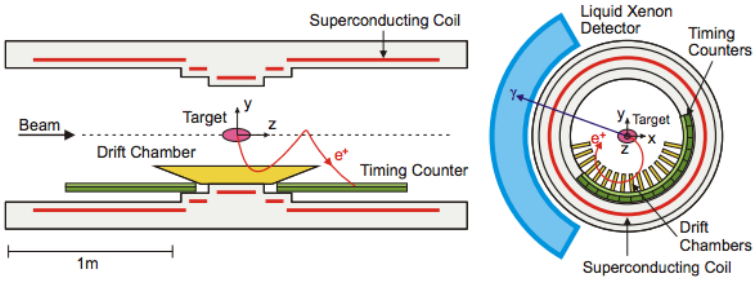

Figure 3.1: *Schematic view of the MEG detector showing one simulated signal event coming from the stopping target.*

magnet, COBRA (COnstant Bending RAdius), generates a gradient magnetic field, with the field strength gradually decreasing at increasing distance along the magnet axis from the centre. This configuration is optimized to sweep low-momentum positrons from Michel decays rapidly out of the magnet, and to keep the bending radius of the positron trajectories only weakly dependent on their emission angle within the acceptance region.

The positron track parameters are measured by a very low mass Drift CHamber (DCH) designed to minimize the multiple scattering . The positron time is measured by a Timing Counter (TC) consisting of scintillator bars read out by PhotoMultiplier. For γ-ray detection, an innovative detector has been developed using Liquid Xenon (LXe) as a scintillation material viewed by PMTs submersed in the liquid. This detector provides accurate measurements of the γ-ray energy and of the time and position of the interaction point. In Table 3.1 resolutions and efficiency for all observable are reported.

The sources of background in this experiment can be divided in two typologies, accidental and correlated:

- **Accidental background:** it is due to the time coincidence of a positron emitted by standard muon decay $\mu^+ \to e^+\overline{\nu}_\mu\nu_e$ and a photon from radiative muon decay $\mu^+ \to e^+\gamma\overline{\nu}_\mu\nu_e$ or positron annihilation in flight $e^+e^- \to \gamma\gamma$. The number of accidental coincidences is dominant and scales with the square of the muon rate and it is proportional to the energy, time and relative direction resolutions of the experiment [19].

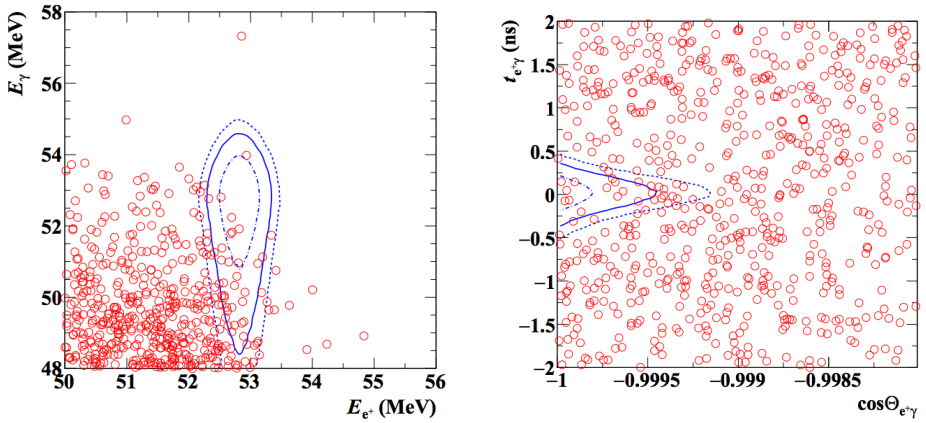

Figure 3.2: *Event distributions for MEG data from 2009 to 2013 in the* (E_e, E_γ) *and* $(t_{e\gamma}, cos\Theta_{e\gamma})$ *planes. The blue lines represent signal PDF at 1,1.64 and 2* σ*.*

- **Correlated background:** it is given by radiative muon decay: the positron and the photon are emitted back-to-back and they are, then, coincident in time. This background results dominant at the very end of the kinematic edge, where the two neutrinos share almost zero energy.

In the run from 2009 to 2011, 3.6×10^{14} muons have been stopped on target. In Figure 3.2 the event distributions for the 2009-2013 full dataset on the (E_{e^+}, E_γ) and $(cos\Theta_{e\gamma}, t_{e^+\gamma})$-planes are reported. It is expected to observe a signal of CLFV around 54 MeV in in the (E_e, E_γ)plane, and around $t_{e\gamma} = 0$ and $cos\Theta_{e\gamma} = -1$ in the $(t_{e\gamma}, cos\Theta_{e\gamma})$ plane, where $t_{e\gamma}$ is the arrival time difference between the photon and the positron and $\Theta_{e\gamma}$ is the emitting angle of the two particles. The data collected show no excess of events compared to background expectations within the signal contour and allow to set a new upper limit on the BR of this decay of 4.2×10^{-13} (at 90% CL) [20], which represents the world best limit.
As shown in Tab. 3.1, while the photon detector and the timing counter almost met their requirements, the resolutions of the positron spectrometer are significantly worse than the design values, with consequences also on the relative $e - \gamma$ timing. A major improvement in the sensitivity to the $\mu \rightarrow e\gamma$ decay by an order of magnitude, down to $\sim 5 \times 10^{-14}$ [21], requires a higher muon stopping rate and improved detectors efficiencies, to achieve a better single event sensitivity. From the experimental point of view some improvements are foreseen (as also reported in in Table 3.1):

- Increasing the number of stopping muons on target ($7 \times 10^7 \mu^+$/s)
- Reducing the target thickness (140 μm) to minimize the material traversed by photons and positrons on their trajectories towards the detector;

- Replacing the positron tracker, reducing its radiation length and improving its granularity and resolutions by means of a new cylindrical Drift Chamber. This also improve the position tracking and the timing evaluation by measuring the e^+ trajectory to the TC interface;
- Improving the timing counter granularity for better timing and reconstruction;
- Extending the γ ray detector acceptance and γ ray energy, position and timing resolution for shallow events replacing the PMTs with VUV-sensitive SiPMs;
- Integrating splitter, trigger and DAQ while maintaining a high bandwidth.

Right now MEG II detector is in a construction phase, the full detector is expected to be ready for the run in 2017.

Variable	Design	Monte Carlo	Obtained	Foreseen MEG^{UP}
Resolution				
Positron (e)				
σ_{E_e} (keV)	200	315	306	130
σ_{ϕ_e,θ_e} (mrad)	5(ϕ_e),5(θ_e)	8(ϕ_e),9(θ_e)	9(ϕ_e),9(θ_e)	5.3(ϕ_e),3.7(θ_e)
σ_{z_e,y_e} (mm)	1	2.9(z_e),1(y_e)	2.4(z_e),1.2(y_e)	-
σ_{t_e} (ps)	50	65	102	-
Photon (γ)				
σ_{E_γ} (%)	1.2	1.2	1.7	1.0
$\sigma_{u_\gamma,v_\gamma}$ (mm)	4	5	5	2.6 (u),2.2(v)
σ_{w_γ} (mm)	5	6	5	5
σ_{t_γ} (ps)	43	69	67	-
Combined (e-γ)				
$\sigma_{t_{e\gamma}}$(ps)	66	95	122	84
$\sigma_{\theta_{e\gamma}}$(mrad)	11	16	17	-
Efficiency				
ϵ_e(%)	90	40	40	88
ϵ_γ(%)	60	63	63	69
ϵtrg(%)	100	99	99	99

Table 3.1: *List of resolution and efficiency for the MEG experiment and foreseen MEG^{UP} experiment*

3.1.2 SINDRUM II

This experiment has currently set the best upper limit on the process $\mu N \rightarrow eN$ $R_{\mu e} < 7 \times 10^{-13}$ in muonic gold.
The muon beam was produced by a 590 MeV proton beam hitting a carbon production target. The backward produced particles (π, μ and e) were then transported by a secondary beam line to a degrader connected to the transport solenoid with a 1.2 T magnetic field.
Here, the muon beam was stopped on a target (in the first stage made of titanium and then gold) and the helical trajectories of the emitted electrons were reconstructed by two drift chambers. Trigger and timing were provided by scintillation and Cherenkov hodoscopes. A schematic view of the experiment is reported in Figure 3.3.
The most important source of intrinsic background in this experiment comes from

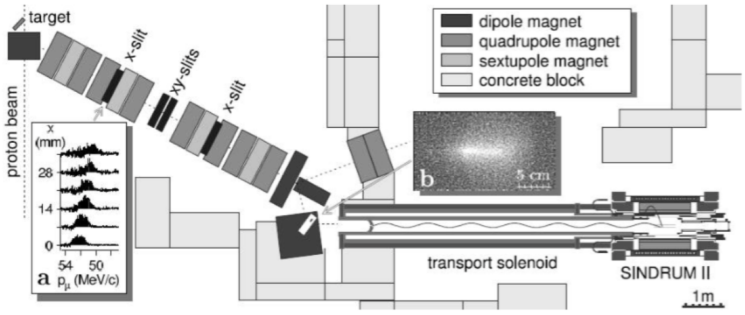

Figure 3.3: *Schematic plain view of the SINDRUM II experiment.*

the muon decay in orbit. However the e^- momentum distribution drops steeply toward the endpoint and the process can be suppressed sufficiently with a momentum resolution around 1% [16].
The main source of background is provided by the *prompt background* related to particles originated at the primary production target which cause high energy background when arriving in the region of the stopping target. Some example of prompt background are:

- Electrons originated from in-flight muons decaying near the stopping target: They can have an energy $E > 100$ MeV if the muon has a momentum $p > 77$ MeV, thus mimicking a CE signal.
- Secondary electrons from radiative pion capture: electrons can be produced via pair production generated by electron emitted when pions stops in the target.
- Secondary electrons from antiprotons annihilation.

- Beam electrons incident on the muon target and scattering into the detector region

These prompt backgrounds were eliminated at SINDRUM II by vetoing candidate signals in time coincidence with particles entering the detector. Veto counters were also used to detect cosmic rays which could mimic a conversion electron. The background generated by antiprotons was eliminated lowering the proton beam energy ($< 600 MeV$).
In Figure 3.4 , momentum distributions of electrons and positrons before and after the RPC background subtraction are reported. Measurement shows no indication for μ-e conversion.

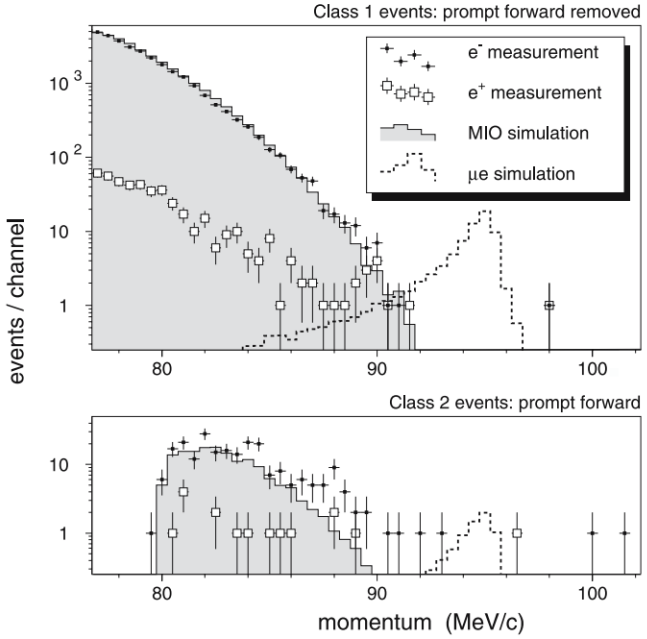

Figure 3.4: *Momentum distributions of electrons and positron before (bottom) and after (top) RPC cuts . Measured distributions are compared with the results of simulations of muon decay in orbit and μ-e conversion*

3.1.3 COMET

The COMET experiment at J-Park has the same Mu2e goal: it will try to improve of a factor 10^4 the sensitivity of $R_{\mu e}$ of the neutrinoless, coherent transition of a muon to an electron in the field of an aluminium nucleus. The muon beam will be produced from the pions created after collisions of the 8 GeV proton beam on a graphite target. As sketched in Figure 3.5 the experiment will be divided in two

different phases [22]: in phase-I the muon momentum and charge are selected using a muon transport solenoid before being stopped in an aluminium target at the centre of a cylindrical drift chamber in a 1 T magnetic field. In a three month running period, 1.3×10^{16}muons will be stopped, this will be enough to reach the design single event sensitivity of Phase-I which, in the absence of a signal, translates to a 90% confidence level branching ratio limit of 7.2×10^{-15}. This is 80 times better than the current MEG limit.

The Phase-I detector will be completed with prototypes of the Phase-II straw tracker

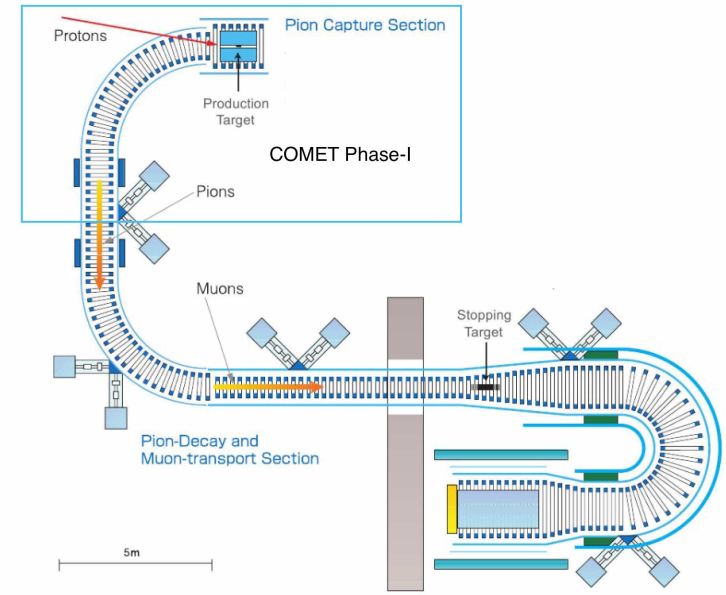

Figure 3.5: *Schematic layout of COMET and COMET Phase-I (not in scale).*

and the electron calorimeter. This will provide a valuable experience with the prototype detectors that will also be exploited to characterize the beam and measure backgrounds to the muon conversion signal to ensure that the Phase-II single event sensitivity of 2.6×10^{-17} can be achieved. Indeed, the experiment requires an intense muon source, coming from a pulsed proton beam with high inter-bunch extinction factor. This experiment is also unique in its choice of a 180° C-shaped muon transport. The second C turn after the stopping target will strongly reduce the background from muon capture on the target. However this assumes that almost all the muon will stop on the target since no muon dump is present. The COMET Phase-II is not approved yet.

3.2 Mu2e experimental setup

The Mu2e apparatus is extensively documented in its Technical Design Report [23]. As shown in Figure 3.6 the layout of the system shows a typical S-shape : the entire system is surrounded by the Superconducting Solenoid Magnet System. In order to limit backgrounds from muons that might stop on gas atoms and to reduce the contribution of multiple scattering for low momentum particles the inner bore of the solenoids are evacuated to 10^{-4} Torr. The solenoids are organized into 3 sub-systems:

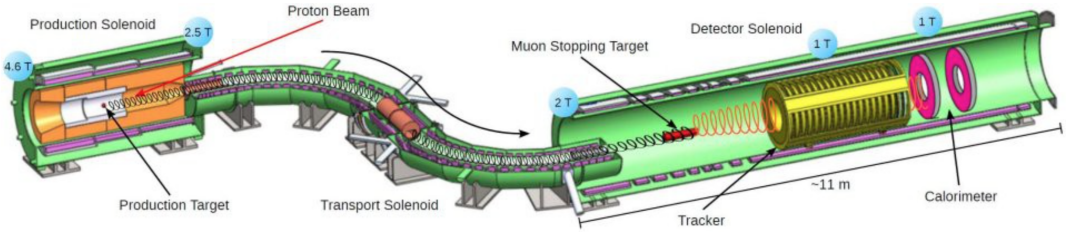

Figure 3.6: *Schematic view of the experimental apparatus.*

- **Production Solenoid (PS)**
- **Transport Solenoid (TS)**
- **Detector Solenoid (DS)**

The 8 GeV proton beam (i.e. above the antiproton production threshold energy) coming from the Fermilab accelerator system enters the PS, hitting the production target. The reaction products with a selected charge are transported through the S-shaped Transport Solenoid, which is long enough to allow the decay of almost all hadrons and allows to suppress line-of-sight particles. The resulting negative muon beam enters the Detector Solenoid and hits the aluminum stopping target: the muons can then be either captured by the atoms and decay (40%) or captured by the nucleus (60%) or convert into electrons. Electrons momentum and energy from Decay in Orbit (DIO) and Conversion Electrons (CE) events are measured by the cylindrical-shaped tracker and by the two-disks calorimeters, respectively.
Downstream of the proton beam pipe, outside the PS, an extinction monitor is used to measure the number of protons in between two subsequent proton pulses. The Detector Solenoid is surrounded by a cosmic ray veto system. Outside the DS, a stopping target monitor is used to measure the total number of muon captures.
In order to achieve the designed single event sensitivity, the produced muon beam must meet strict requirements:

- High rate: a larger number of stopped muons is essential to improve previous experiments results. The present proposed rate is of $4.21 \times 10^{10} \mu^-/\text{s}$.
- Pulsed structure: in order to suppress the prompt background, the muons hitting the stopping target should be distributed in a narrow time burst (< 200 ns), each one separated by the other by intervals of $\sim 1.5\ \mu$s (larger than the muonic aluminum lifetime). The result of SINDRUM II experiment was ultimately limited by the presence of the veto counters, necessary for the suppression of the prompt background. Mu2e, instead, will take data 670 ns after the injection bursts, to let the prompt background (especially pion capture) to subside. The data- taking time window will then close 925 ns after, just before the arrival of the next bunch. Given the time scheme provided by the Fermilab accelerator complex, the muon capture time in Al maximizes the total number of muons on target.
- Extinction: between-bursts extinction is fundamental to suppress background generated by unwanted beam between pulses.
- A high precision detector for momentum selection

The timing structure of the beam is reported in Figure 3.7: the proton beam hits the production target with bursts 200 ns large and separated from the next one by ~ 1700 ns. The detector system starts taking data 670 ns after the arrive of the proton pulse, when almost all pions are decayed.

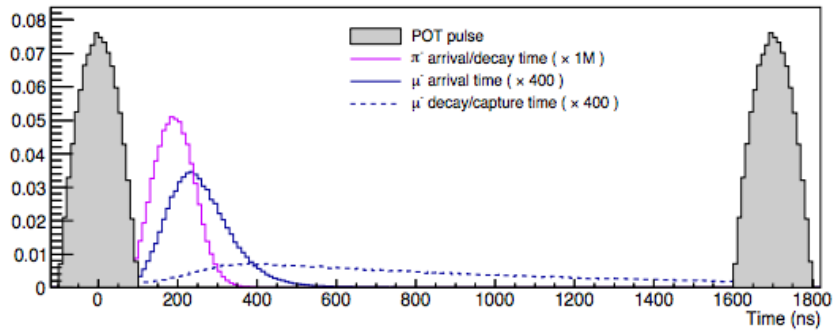

Figure 3.7: *Timing structure of the Mu2e beam.*

3.2.1 Accelerator system

An high intensity, pulsed proton beam to produce an intense beam of low energy muons with a given time structure is required by the experiment.

Some modifications to the existing Fermilab acceleration system are required. Protons and antiprotons were accelerated in different steps while Tevatron was working (Figure 3.8):

1. **Cockcroft-Walton generator**: it turns hydrogen gas into H-ions by flowing it into a container lined with molybdenum electrodes: a matchbox-sized, oval-shaped cathode and a surrounding anode, separated by 1 mm and held in place by glass ceramic insulators. A magnetron is used to generate a plasma to form H- near the metal surface. A 750 keV electrostatic field is applied by the Cockcroft-Walton generator, and the ions are accelerated out of the container.

2. **Linear Accelerator (Linac):** it accelerates the particles to 400 MeV ($\sim 0.7c$). Right before entering the next accelerator, the H-ions pass through a carbon foil, becoming H+ ions (protons).

3. **Booster ring:** it is a 468 m circumference circular accelerator that uses magnets to bend beams of protons in a circular path. The protons coming from the Linac travel around the Booster about 20000 times in 33 ms so that they repeatedly experience electric fields. With each revolution the protons pick up more energy, leaving the Booster with 8 GeV.

4. **Main Injector:** it has three main functions: accelerate protons from 8 GeV to 150 GeV, delivers protons for antiproton production, and accelerate antiprotons, coming from the Antiproton Source, to 150 GeV

In Figure 3.9 the accelerator complex providing proton beam to the Mu2e experiment is reported: protons are acquired from the Booster during the available portions of the Main Injector, now named recycler RING, timeline when slip-stacking operations are underway for the NOνA experiment. Booster protons containing 81 batches of 53 MHz bunches, are extracted into the MI-8 beamline and injected into the Recycler Ring. As each batch circulates in the Recycler Ring it is re-bunched with a 2.5 MHz RF system to form four bunches with the bunch characteristics required by the Mu2e experiment. After the 2.5 MHz bunch formation, the beam is extracted from the Recycler, one bunch at a time, and transported to the Delivery Ring (the old antiproton source). The beam is then resonantly extracted into the M4 beamline where it is transported to the Mu2e production target.

3.2.2 Production Solenoid

The production solenoid is a high field superconducting magnet with a graded field varying from 4.6 T to 2.5 T. The solenoid is approximately 4 m long and has an inner

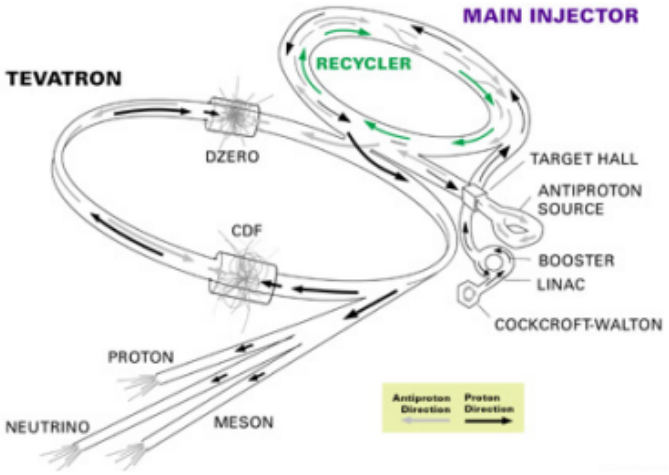

Figure 3.8: *Sketch of the various Fermilab accelerator components employed when Tevatron was running.*

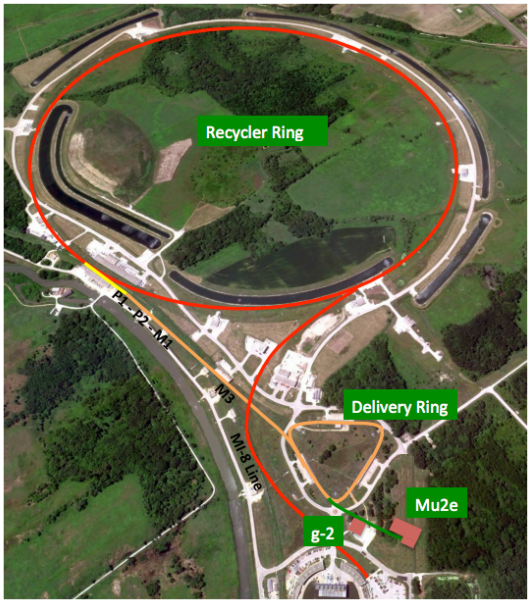

Figure 3.9: *The components of the Fermilab accelerator complex used to acquire protons for the Mu2e experiment.*

bore diameter of about 1.5 m evacuated to 10^{-5} Torr.
In order to limit the radiation damage of the PS coils a bronze shield structure is placed between the inner bore and the PS coil. As shown in Figure 3.10 proton beam enters in the middle of the PS and strikes a radiatively cooled Tungsten target, producing mostly pions. The production target consists of a tungsten rod, 160 mm long and

with a 6.3 mm diameter, placed within a titanium support ring. The tungsten has been chosen as target material because of its thermal properties: the high melting point and the low thermal expansion coefficient.
The axially graded magnetic field, creating a "magnetic bottle", reflects the charged particles, emitted in the opposite side with respect to the TS entrance, toward the low B-field region where the PS is linked to the TS.

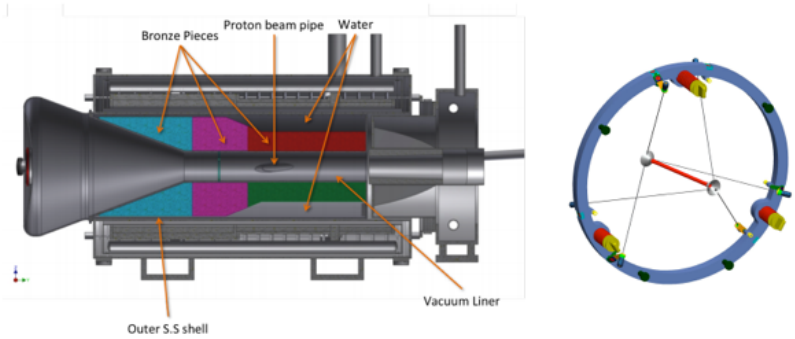

Figure 3.10: *Left:View of the Production Solenoid. Right:Schematic 3D view of the tungsten production target and its titanium support wheel.*

3.2.3 Transport Solenoid

The S-shaped Transport Solenoid efficiently transmits low energy negatively charged muons from the Production Solenoid to the Detector Solenoid. Due to the presence of absorbers and collimators, high energy negatively charged particles, positively charged particles and line-of-sight neutral particles are nearly all eliminated before reaching the Detector Solenoid. The Transport Solenoid consists of five distinct regions (Figure 3.11) :

1. a 1 m long straight section (TS1) that links the PS to the TS and houses a collimator that selects particles with momentum lower than 100 MeV/c

2. a 90° curved section (TS2) that avoid neutral particle from the PS to propagate into the DS;

3. a second straight section about 2 m long (TS3) containing two collimators, for filtering particles based on charge and momentum, separated by a berillium window, needed for stopping antiprotons;

4. a second 90° curved section (TS4) that brings the beam back to its original direction and does not allow neutral particles from the beam interactions in the TS3 to reach the DS;

5. a third straight section of 1 m length (TS5) that is equipped with a collimator for momentum selection.

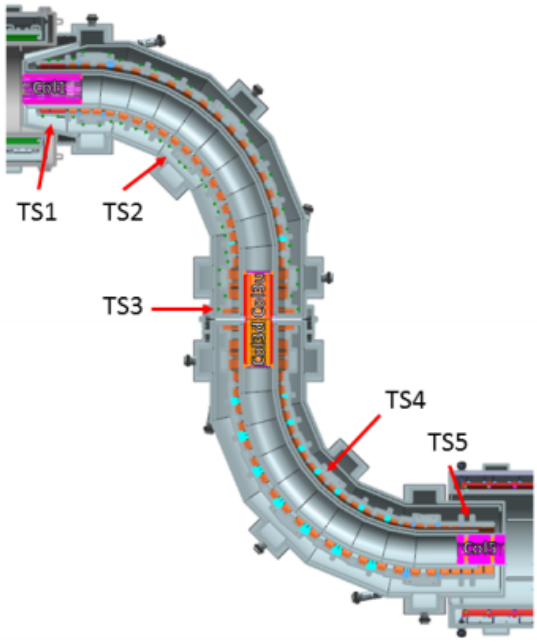

Figure 3.11: *Transport Solenoid view.*

3.2.4 Detector Solenoid

The Detector Solenoid is a large, low field magnet that houses the muon stopping target and the detectors to identify and analyze conversion electrons from the stopping target (Figure 3.12) .
It is nearly 11 m long with a clear bore diameter of about 2 m. The muon stopping target is placed in a graded field that varies from 2 to 1 Tesla so that it captures conversion electrons emitted in the direction opposite the detectors and reflects them back towards the detectors. The graded field is important also for reducing the background from high energy electrons: since they are accelerated towards the detector,

the resulting angle of these electrons is inconsistent with the angle of a conversion electron from the stopping target. The detectors reside in a field region that is relatively uniform. The inner bore of the Detector Solenoid is evacuated to 10^{-4} Torr to limit the multiple scattering backgrounds from muons that might stop on gas atoms.

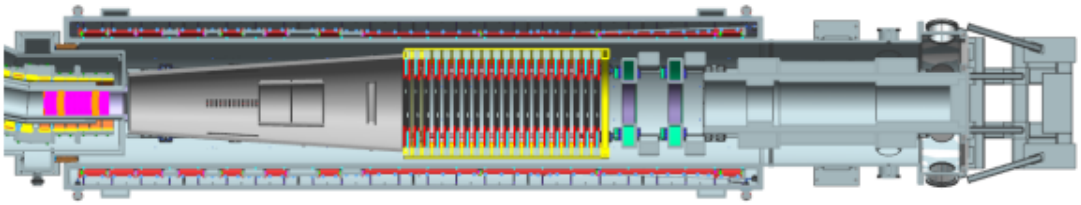

Figure 3.12: *Detector Solenoid view.*

The muon stopping target consists of 17 thin aluminum foil arranged coaxially along the Detector Solenoid axis (Figure 3.13, left). The target material Z has to be enough high to stop a significant fraction of muons coming from the TS, but not so massive to corrupt the momentum measurement of the produced conversion electrons. Energy loss and straggling in the stopping target are significant contributors to the momentum resolution function. The distributed, tapered target is designed to stop as many muons as possible while minimizing the amount of material traversed by conversion electrons that are within the acceptance of the downstream tracker.
For future running as in Mu2e-II, there will be the possibility to change target material. This is indeed importat since there is a large $R_{\mu e}$ rate dependence on the stopping target material as shown in Figure 3.13 (right).

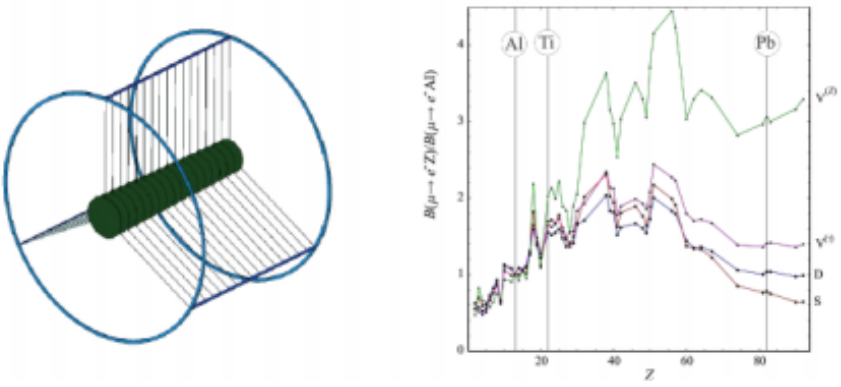

Figure 3.13: *Left: 3D view of the Mu2e stopping target. Right: target dependence of $R_{\mu e}$ (normalized to the Aluminum value) for different single operator dominance models.*

3.3 Mu2e Detector

The Mu2e detector is located in the nearly uniform 1 Tesla magnetic field in the DS and is designed to efficiently and accurately identify and analyze the helical trajectories of ~ 105 MeV electrons in the time varying high-rate environment of Mu2e.
The detector consists of a tracker and a calorimeter that provide redundant energy and momentum, timing, and trajectory measurements. A cosmic ray veto, consisting of both active and passive elements, surrounds the Detector Solenoid and nearly half of the Transport Solenoid.

3.3.1 Tracker

The Mu2e tracker will measure electrons trajectory in order to calculate their momentum.
The main aims of Mu2e tracker are:

- Minimize multiple Coulomb scattering and energy loss to obtain a good momentum resolution;
- Provide sufficient numbers of hits to find and fit tracks with high efficiency.
- Have segmentation and/or multi-hit capability to operate at the expected rates.
- Provide redundancy to protect against mis-reconstructions and non-Gaussian tails.

The tracker total lenght is ∼3 m and its diameter is 1.6 m. It is locate in a region with 1 T uniform magnetic field and its active area's radius extends from 40 to 70 cm, so that, as shown in Figure 3.14 , particles with a very low momentum do not reach at all the active area or just leave leave too few hits for a track to be reconstructed. This increases the tracker purity. The detector is made of 20736 drift straw tubes placed transverse to the axis of the DS. Current choice for drift gas is 80:20 Argon: CO_2 with a maximum operating voltage of1500 V.
Straws features are presented in table 3.2

Sense wire	$25\mu m$
Tube diameter	5 mm
Thickness	$15\mu m$(Mylar)
Lenght	334÷ 1174 mm
Gap between straws	1.5 mm

Table 3.2: *Overview of straws parameters*

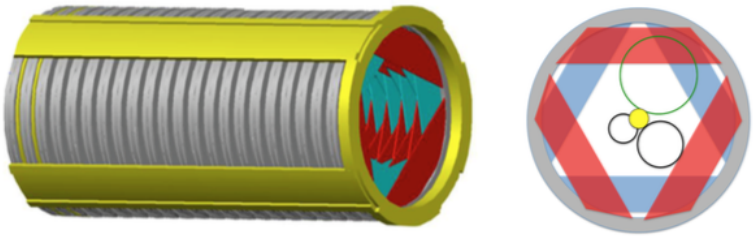

Figure 3.14: *Cross view of Mu2e tracker with trajectories of a 105 MeV/c momentum conversion electron (top), 53 MeV/c Michel electron (bottom right) and electron with energy small than 53 MeV (bottom left).*

As shown in Fig 3.15, groups of 96 straws are assembled into panels. In order to reduce the "righ-left ambiguity", 6 panels (three per side rotated by 120 degrees) are assembled into planes. These two layers of straws allows to determine easily on which side of the wire a track is passed.

Six panels are assembled into a plane. A face of a plane is made of three panels,

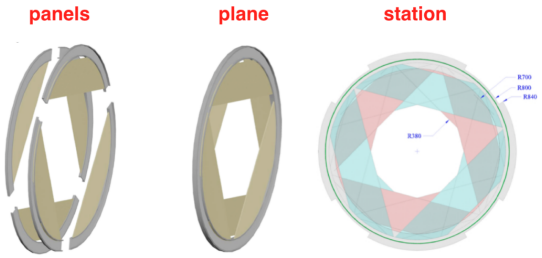

Figure 3.15: *Sketch of completed panel, planes and stations.*

which are rotated by 30° .

A pair of planes made a station, each station is separated by 46 mm. This two planes are identical but the second plane is rotated of 180° around the vertical axis with respect to the first plane. The Mu2e experiment is composed of 18 stations.

Indeed errors in pattern recognition can reduce acceptance of the signal and generate background.

In Fig 3.16 it is shown that the signal distribution has a peak not at the conversion energy, that is $p = 104.95 MeV/c$ (for Al) but around 104 MeV/c because of the energy loss. We expect for signal distribution a $\sigma \approx 350$ keV/c. Tracker resolution is an important component in determining the level of several critical backgrounds. As shown in Figure 3.17 the tracker is required to have a high-side resolution of σ ~120 - 180 keV with small positive tails, since these tails could increase the contribution of the background events, promoted in the signal region, from the fast falling DIO

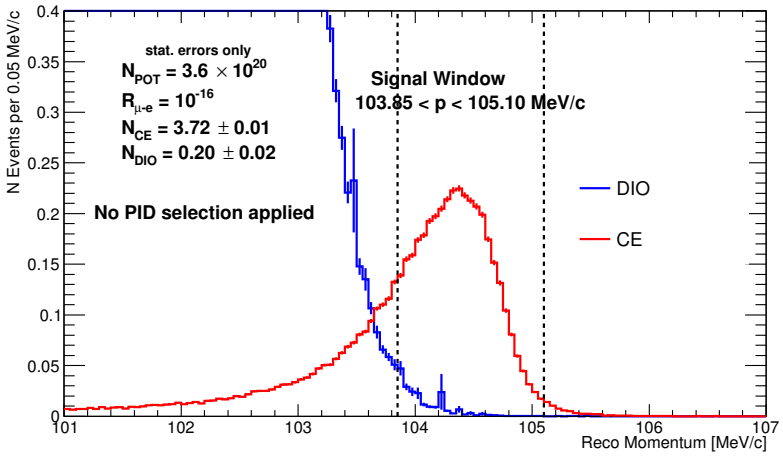

Figure 3.16: *Simulation of the reconstructed momentum spectrum for DIO (blue) and conversion electron (CE) events surviving selection criteria and normalized to the total number of muon stop for* $3.6x10^{20}$ *POT.*

spectrum.

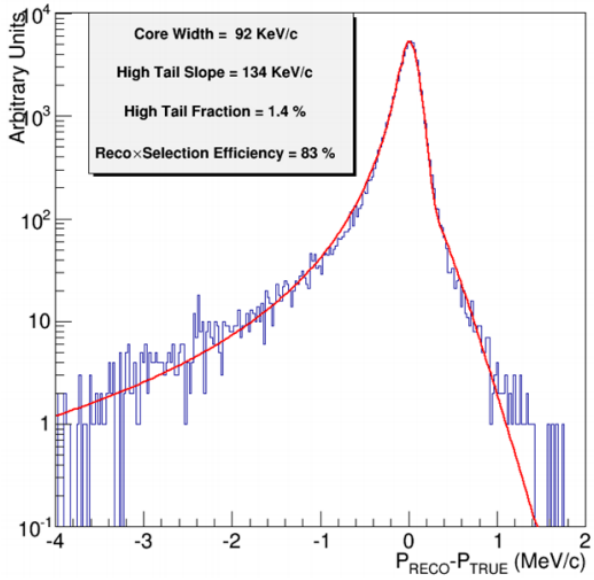

Figure 3.17: *Tracker momentum resolution with conversion electrons. Full background overlay and pattern recognition included. Fit to a split double Gaussian with standard track fit quality cuts. The core width satisfies the 180 keV momentum resolution requirement.*

3.3.2 Calorimeter

The Mu2e calorimeter must operate in a high-rate, high-radiation environment. This motivates a fast response, an excellent time resolution and good radiation hardness requirements. The Mu2e calorimeter has to:

- Provide the means to implement an independent trigger based on the sum and pattern of energy deposition;
- provide a "seed" to improve tracker pattern recognition and reconstruction efficiency;
- provide shower shape, energy, and timing information that, in combination with information from the tracker, can distinguish electrons from muons and pions;
- have large acceptance for signal electrons within the acceptance of the tracker.

After a long R&D phase, the best compromise between costs and properties has been selected: the calorimeter design consists in 1346 undoped CsI crystals located downstream of the tracker, arranged in two disks and, positioned at a distance of half wavelenght of a typical conversion electron (Figure 3.18).

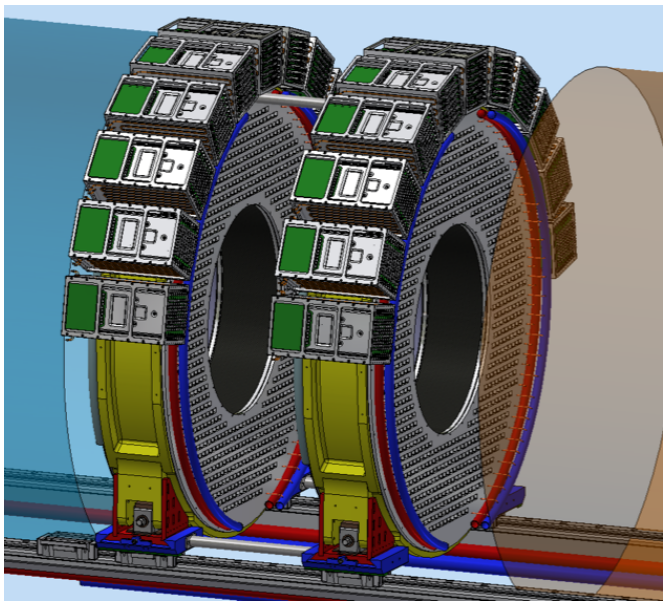

Figure 3.18: *CAD model of the Mu2e electromagnetic calorimeter.*

The crystals have squared faces with dimensions of (34×34) mm^2 and are 200 mm long. Each crystal is read by two 2×3 array of individual 6×6 mm ^{2} UV-extended

Silicon Photomultipliers (SiPMs). The solid-state photodetectors are necessary due to the presence of the high magnetic field. FEE, HV, slow controls and digitizer electronics are mounted behind each disk and must then work adequately in a high vacuum (to reduce multiple scattering), high magnetic field and high radiation environment. Equalization of the crystal response will be provided through a circulating radioactive source (FluorinertTM, C8F18), already experimented by the BaBar EMC [25] while a laser flasher system will be used for relative calibration and gain monitoring. Usage of cosmic ray events for the calibration along running is also planned.

3.3.3 Cosmic Ray Veto (CRV)

Cosmic muons are a source of background for the Mu2e experiment: they can produce 105 MeV electrons through interaction with the apparatus or with a decay-in-flight. The CRV system provides both a passive shielding (thick layer of concrete surrounding the DS) and an active veto, with a system of four layers of long scintillator strips, with aluminum layer between them, covering all the DS and the last part of the TS (Figure 3.19). The strips are 2 cm thick, providing ample light yield to allow a low

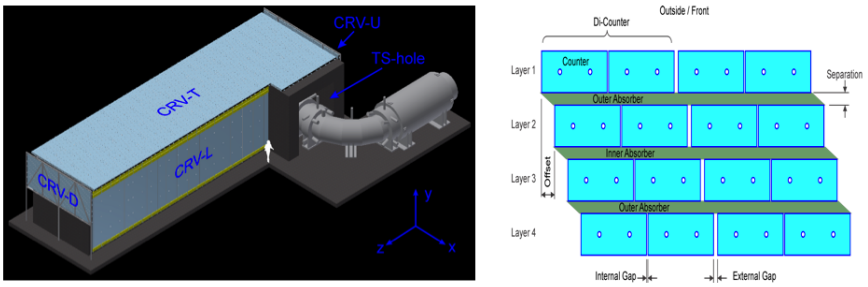

Figure 3.19: *Left: 3D view of the of the cosmic ray veto. Right: detail of a single CRV module with 4 scintillator strips.*

enough light threshold to be set to suppress most of the backgrounds. Aluminum absorbers between the layers are designed to suppress punch through from electrons. The scintillation light is then captured by optical fibers and then read out by means of SiPMs.

Chapter 4

Calorimeter Requirements

As already explained the Mu2e calorimeter must provide energy, position and timing information in order to confirm the events reconstructed by the tracker and distinguish fakes produced by cosmic rays and antiprotons. Moreover, the calorimeter should be fast enough to provide a trigger for the experiment.
These tasks lead to the following requirements:

- a rejection factor for muons of $\approx$ 200 while retaining high signal efficiency ($>$ 90%) for conversion electrons;
- provide an independent trigger to identify signal events and derive an unbiased estimate of the track trigger efficiency;
- an energy resolution $\sigma \cong$ 5% and a timing resolution better than $\sigma_t \approx 0.5$ ns to provide the needed muon rejection. The good timing also ensures that the energy deposits in the calorimeter are matched in time with events reconstructed in the tracker and pileup events are discarded;
- control (or measure and correct for) temperature and gain variations such that the combined energy response of a crystal calorimeter and its readout do not vary by more than 0.5%, i.e., is small compared to the energy resolution;
- a cluster position resolution of the order of $\sigma_{x,y} \cong 1$ cm to allow comparison between the position of a calorimeter energy cluster to the extrapolated trajectory of a reconstructed track.

The calorimeter will operate in a unique, high-rate Mu2e environment and maintain its functionality after a total gamma radiation exposure of up to 100 krad and for a total neutron fluency equivalent to $3 \times 10^{11}\ n_{(1\ MeV)}\ /\mathrm{cm}^2$.
Moreover an adequate monitoring of temperature, pressure and radiation dose rate

is required to and to ensure optimum performance of the calorimeter, as well as for the safe operation of the system.

4.1 Energy and time resolution

The calorimeter energy resolution (which is much larger than that of the tracking system) is set so that the measured energy could provide an E/p value sufficiently precise to allow the separation of conversion electron candidates from muons produced by cosmic rays that evades the Cosmic Ray Veto. An energy resolution of the order of 5% is sufficient to fulfill this requirement.
Several effects can affect the energy resolution such as: photoelectron statistics, energy loss in passive material, energy that escapes the calorimeter due to albedo or incomplete shower containment (leakage), contribution of electronic noise and energy from background sources in pile-up that is included when clusters are formed by the pattern recognition algorithm. In Figure 4.1, the result of a Monte Carlo simulation for a 105 MeV CE impinging at 50° on the calorimeter surfaceis reported. The energy resolution, computed as (FWHM/2.35), for a ten radiation length CsI calorimeter is shown as a function of the number of detected photoelectrons/MeV with a standard rate of background events in pile-up. A cesium iodide calorimeter can meet the energy resolution requirements.
The calorimeter time measurements have to be compared with the track arrival times

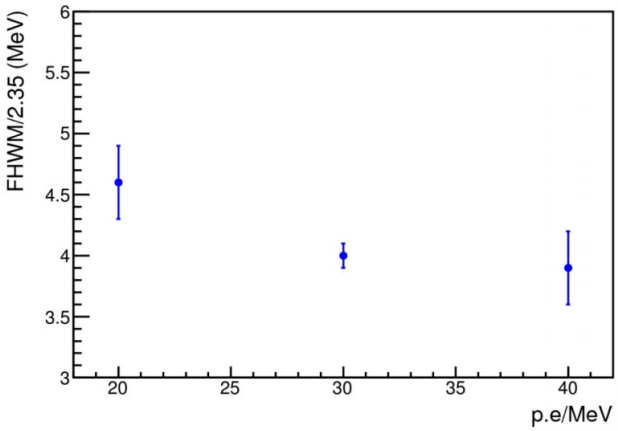

Figure 4.1: *Energy resolution (FWHM/2.35) of a CsI calorimeter determined by Monte Carlo simulation.*

on the calorimeter surface, that is estimated with the track extrapolation and timing, to guarantee an high PID capability. The time of passage is known to no better than

the total time it takes to drift from the outer radius of a straw to the inner wire: the resolution is then $1/\sqrt{12}$ of that time. Considering a 50 μm/ns gas and 2.5 mm radius, each hit has a time resolution of 15 ns. From the simulation a time resolution of $\sim$ 1 ns is found. A test performed with a CsI crystal readout by a Mu2e custom SiPM resulted in a time resolution of $\sim$ 170 ps with minimum ionizing particles so that we expect a crystal calorimeter can match this requirement (see Chapter 7.2).

4.2 Pattern reconstruction

The calorimeter timing information can be used to improve the track reconstruction considering two different steps:

1. Selection of straw hits from the tracker using the timing;
2. helix fit of the filtered hits.

The calorimeter cluster time gives the possibility to know the impact time of the particles with high precision, so that the time window increases the S/N ratio. The distribution of the simulated residuals between the time of all the straw hits and the one of the CE calorimeter cluster (Figure 4.2) presents a CE peak over a flat background. This shape is due to the time that a CE electron takes, on average, to cross

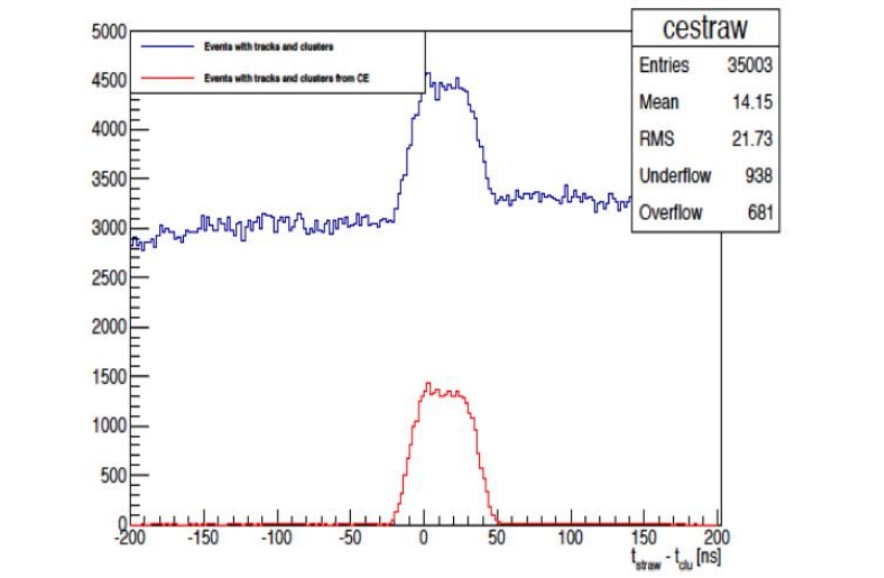

Figure 4.2: *δt (straw - cluster) distribution for all hits (blue) and the CE related hits (red).*

the tracker region ($\approx$ 12 ns) and to the drift time in the straw ($\approx$ 40 ns): the distribution then starts at 12 -40 = -28 ps, the CE time window is related to the full drift time,

spurious hits from delta rays or background particles may fall into this time window. Retaining only the hits in the CE region dramatically reduces the combinatorial background and the S/N ration improves of a large factor. This is clearly shown by the comparison of the tracking event display in Figure 4.3 before (left) and after (right) the application of this cut.
Seeding the track finding algorithm with calorimeter selected hits improve the track-finding efficiency by $\approx 10\%$.

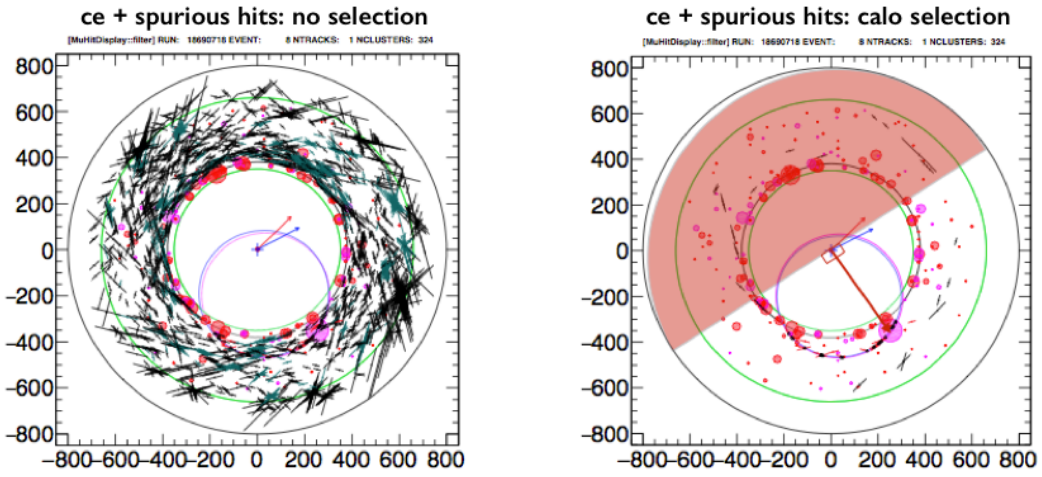

Figure 4.3: *Distribution of the hits in the tracker before (left) and after (right) the application of a cut on the δt variable.*

4.3 Position resolution

The purpose of the calorimeter hit position measurement is to confirm that the reconstructed track points to the location measured by the calorimeter itself.
The position resolution should ideally be comparable to or better than the extrapolated position error from the upstream track.
In Figure 4.4, the difference between the extrapolated track and the true impact point for a sample of simulated conversion electrons is reported. Tracks enter the calorimeter at an angle close to 45°. Since the shower depth is not known, the distance $\Delta_y = y_{track} - y_{cluster}$ depends on the track direction, as well as on the shower depth. Track-to-cluster residuals are calculated in the direction orthogonal to the track in order to remove dependencies so on the shower depth. The extrapolated position resolution of the tracker at the face of the upstream calorimeter disk is then $\sigma_x = 7.95$ mm and $\sigma_y = 7.92$mm. The position resolution of the calorimeter should be comparable to these values. From simulation it results that, at the expected occupancies of

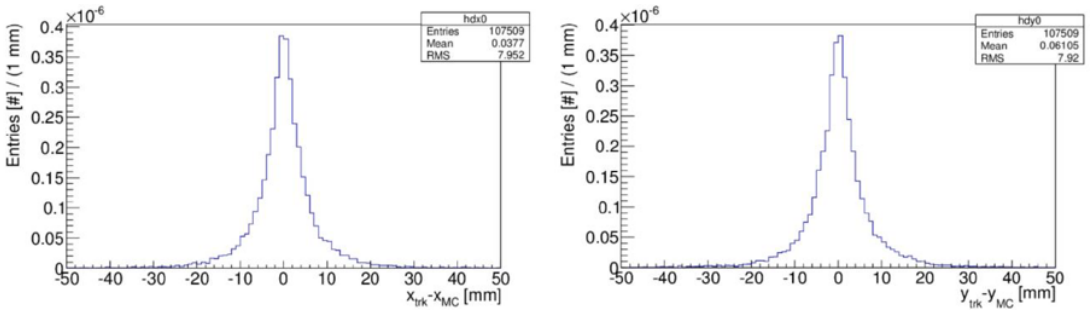

Figure 4.4: *Distribution of the difference between the real impact point of DIO tracks in the range 90 to 105 MeV/c at the calorimeter face and the extrapolated value using the parameters of track reconstruction algorithm.*

the experiment, a calorimeter position resolution of $\mathcal{O}(1)$ cm is sufficient to match well the total tracks-clusters.

4.4 Particle identification

The primary goal of the particle identification (PID) at Mu2e is to separate potential signal, electrons from $\mu \rightarrow e$ conversions, from muons which could be associated with the beam or produced by cosmic rays.
In the following it is shown that, in order to sufficiently suppress cosmic ray and antiproton induced backgrounds, the calorimeter must have PID capabilities.

4.4.1 Muons rejection

A muon generated by a cosmic ray can enter the DS and bypass the Cosmic Ray Veto, mimicking a conversion electron signal. The most recent studies of cosmic rays induced background [26] indicate the presence of about 1 events for 3 years of data, in which negative cosmic muons with the correct momentum survive all the analysis cuts passing in holes of the veto system.
In order to keep this background negligible with respect to the 0.1 events related to CR events and CRV inefficiency, a muon rejection factor of 200 is required. A limited PID capability is available with tracker informations only (based on tracking timing and dE/dx). Combining tracker and calorimeter information it is instead possible to meet the rejection requirements [27].
The Mu2e particle identification algorithm is based on energy reconstruction, shower shape and the time difference between calorimeter timing and extrapolated arrival

time of the track at the calorimeter face under the electron hypothesis (δt_e). In Figure 4.5, the distributions of δt_e and E/p for muons and electrons are reported. A timing resolution of ~ 0.5 ns and an energy resolution of $\mathcal{O}(5\%)$ are necessary to maintain high efficiency and a μ rejection factor of 200.

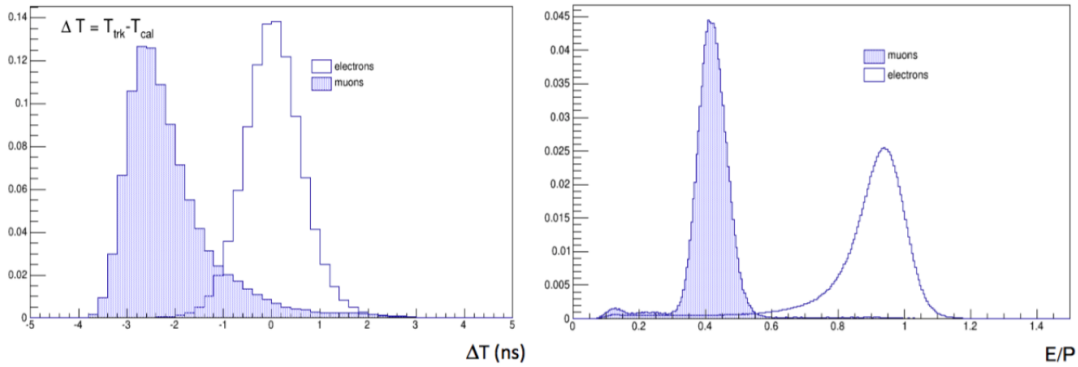

Figure 4.5: *Distribution of δt_e (left) and E/p (right) variables for electrons (white) and muon (blue) of same momentum (104.4 MeV/c).*

4.4.2 Antiproton rejection

Since antiprotons are slow and negatively charged, when they survive the absorber in the TS collimator can produce a nasty background, in the data taking time window, composed of μ^-, π^-, e^-. While it is possible to reject μ^-, π^- using particle identification informations from the calorimeter [28], the e^- background is irreducible. From simulation, we compute that the calorimeter PID can reduce the non-electron components of the $\overline{p}$ induced background to the level of few 10^3 events in the enlarged signal region of [100, 106] MeV/c.

4.5 Trigger

Mu2e may use both the sum and the pattern of energy deposition to form an online "Level 1" standalone trigger. This trigger can provide an independent measurement of the track trigger efficiency, and be affected by different systematics due to environmental background.
Figure 4.6 shows the performance of a trigger based on the energy deposits in the calorimeter as extracted from the digitized waveform. A signal efficiency above 60% with at a background rejection level of 100 is achievable. Such rejection level is needed

to maintain an acceptable trigger rate. The corresponding efficiency is large enough to evaluate the tracker trigger efficiency.

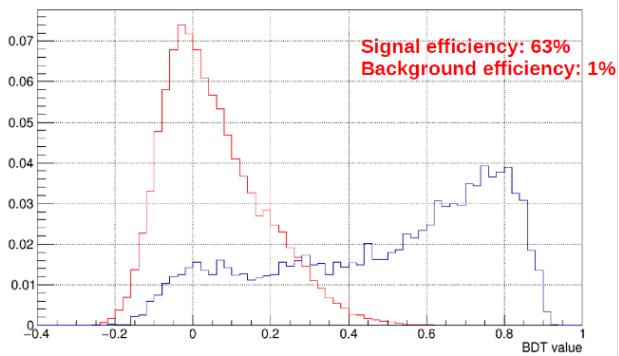

Figure 4.6: *Distribution of the BDT discriminating variable for the calorimeter trigger for signal (blue) and background (red) events.*

4.6 Environment and Radiation hardness

The calorimeter must operate in 1 Tesla solenoidal magnetic field and in a high radiation environment. The calorimeter crystals has to withstand a total gamma radiation dose of 100 krad/yr [29] [30] [31] and a total neutron fluence of 10^{12} n/cm^2 in three years of run.
The SiPMs and FEE electronics are shielded by the crystals themselves and the highest dose rate expected on a SiPM is $\sim 6 \times 10^{10}$ n/cm^2/yr (1 MeV equivalent). Adding safety factors, we ask that the photosensors should survive a total neutron fluence of 3×10^{11} n/cm^2 (1 MeV equivalent) integrated in three years of run.
Since the light output of the crystals and the gain of the SiPMs show a temperature dependence, the calorimeter temperatures, in both front face and and FEE rear face, have also to be monitored.
Our calibration system (laser+ source) will allow to monitor the individual calorimeter channels so that the contribution of the crystal light output changes and the gain variation of the readout devices due to temperature and irradiation will be monitored and controlled.

Chapter 5

Silicon Photomultipliers

In this chapter, the semiconductor characteristics and their applications as photon detectors will be described. In particular, semiconductor photosensor applications with a reverse bias voltage will be discussed. Silicon photosensors working in linear and Geiger mode will be described and finally Silicons Photomultipliers and their characteristics will be presented.

5.1 Semiconductor and p-n junction

The solution of the Schroedinger equation for the electron energy, in a periodic potential created by the atoms of a crystal lattice, involves the existence of splitted energy levels and the formation of energy bands. Since the discrete energy levels in each band are densely packed, it is possible to consider them as a continuuum.
The valence and conduction bands are separated by the bandgap energy E_g. Material with a full valence band and $E_g > 3$eV are named insulator; materials with a very small energy gap are named conductor. Semiconductors are characterized by an energy gap between 0.1 eV and 3 eV.
Semiconductors like Silicon (Si) and Germanium (Ge) have four electrons in the valence band. As shown in Figure 5.1, some electrons can be thermally excited from the valence to the conduction band. As a consequence the valence band has an unoccupied quantum state so that the electrons remaining in the valence band can in turn exchange places with other under the influence of an electric field. At the same time electrons in the conduction band are free to move thanks to the electric field producing current.[1] Semiconductors properties can be magnified controlling the in-

[1]The whole process can be also seen as the motion of an holes with charge e^+ from the conduction to the valence band.

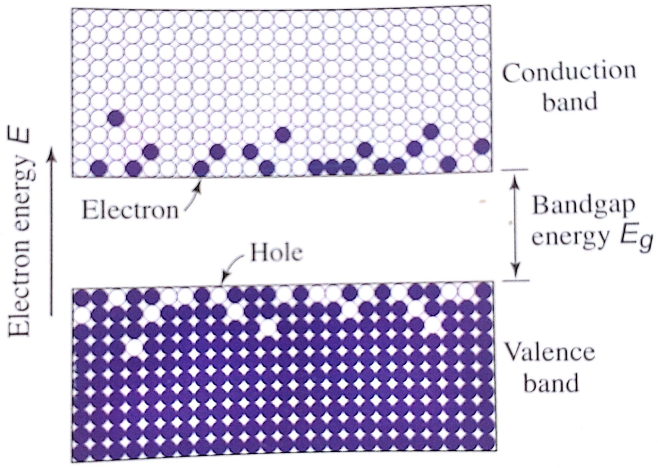

Figure 5.1: *Electron in the conduction band and holes in the valence band at $T > 0°$ K.*

troduction into the materials of particular impurities called dopants: replacing a small portion of normal atoms in the crystal lattice with dopants with an excess of valence electrons (donors) creates a predominance of e^- carriers. Such a material is called *n-type* semiconductor. A *p- type* semiconductor, characterized by the excess of holes, is created by using a dopant with a lack of valence electrons (acceptor). Juxtaposition of an *n-type* semiconductor with the same semiconductor p-doped is called *p-n* homojuction.

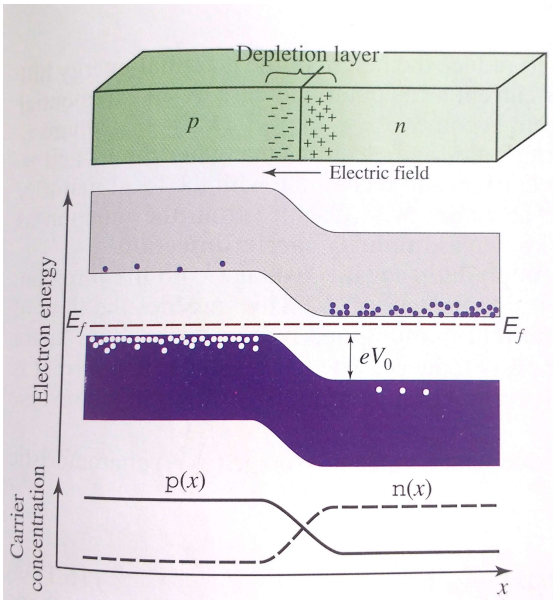

Figure 5.2: *p-n junction at thermal equilibrium with $T > 0°K$.*

When the two regions are brought in contact, as shown in Figure 5.2 carriers drift from the area with higher concentration towards the area with lower concentration. Electrons diffuse from the n-type region to the p-type region, where electrons recombines with the abundant holes; holes drift from the p-type region to the n-type region recombining with electrons.
This process does not continue indefinitely and causes a displacement of the charge distribution in the two regions.
As the carriers drift the electric field in the depletion region, pointing from the *n* side towards the *p* side, obstructs the diffusion of the mobile carriers through the junction until an equilibrium condition in established. A narrow area nearly depleted of mobile carriers, called the "depletion region", forms in both regions near the junction.
This layer contains only fixed charges and its area is inversely proportional to the dopant concentration in the region.
It is possible to apply to the junction an external potential that alters the potential difference between the *p*- and *n*- regions. In particular applying a positive potential $+V$ to the *p*- side an electric field is created in a direction opposite to the buit-in field, the junction is *forward biased*. As shown in Figure 5.3, the applied voltage breaks the equilibrium condition causing a decrease of the potential gap between the *p*- and *n*- regions, the majority carrier concentration increases so that the output current exponentially increases too.
If a negative potential $-V$ is applied to the *p*- region the junction is *reversed biased*.

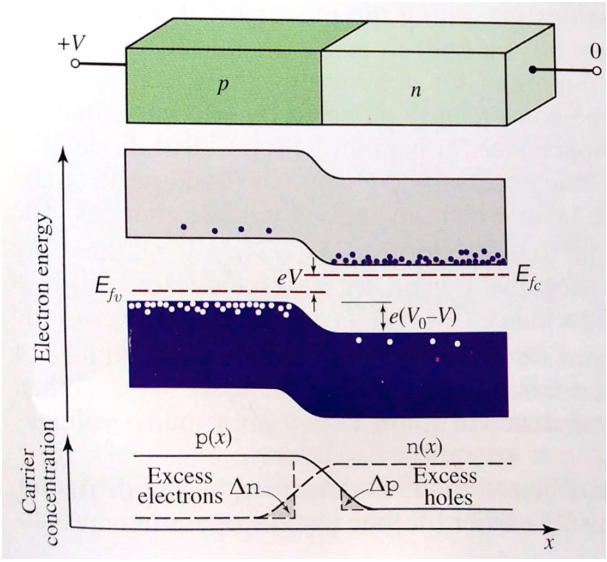

Figure 5.3: *Energy-band diagram and carrier concentrations for a forward biased* p-n *junction.*

The potential gap increases and the field created is concordant with the buit-in one preventing the majority carriers flux. In these conditions the output current is the results of the electron-hole recombination in the depletion region. Hence a *p-n* junctions, as reported in Figure 5.4, acts as a diode with a current voltage characteristic:

$$i = i_s\left[exp\left(\frac{eV}{KT}\right) - 1\right] \quad \text{with} \quad V = \begin{cases} V > 0, & \text{forward biased junction} \\ V < 0, & \text{reverse biased juction} \end{cases} \tag{5.1}$$

where i_s is a constant.

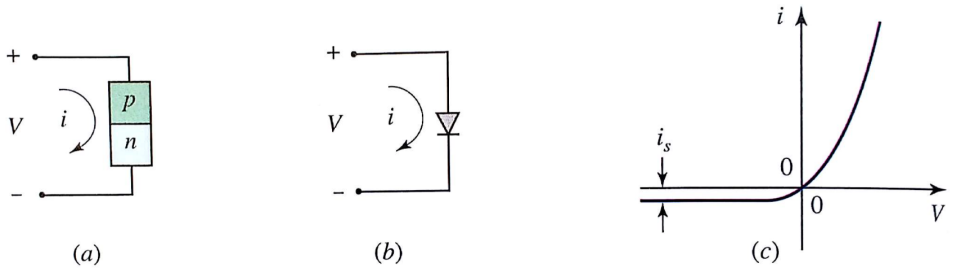

Figure 5.4: *(a) Voltage and current in a* p-n *junction. (b) Circuit representation of the* p-n *junction diode. (c) Current-voltage characteristic of an ideal* p-n *junction.*

5.2 Quantum efficiency

Quantum efficiency is defined as the probability that a single incident photon generates a couple of electron-hole carries.
Considering an high number of incident photons, quantum efficiency is defined as the ratio of this number ($N_{arrives}$) to the flux of carriers generated in the device (N_γ). It is usually represented by the ϵ ($0 \leq \epsilon \leq 1$) symbol and it is related by the following equation to other parameters :

$$\epsilon = \frac{N_{arrives}}{N_\gamma} = (1 - R)\zeta\left[1 - e^{-\alpha x}\right] \tag{5.2}$$

where:

(i) the $(1 - R)$ term represents the reflection effects that incident photons experiment on the devices surface, it can be reduced it using dedicated antireflection coatings;

(ii) the ζ factor represents the fraction of electron-hole pairs which effectively contribute to the photocurrent avoiding recombination with superficial material.

(iii) the $[1 - e^{-\alpha x}]$ term is the probability of crossing all the Si layer and depends on the absorption coefficient (α). In Figure 5.5 several absorption coefficients for different semiconductors are shown.

The probability of photon absorption in a dx region, placed at a distance x from the optical coupling interface, is given by the product of the probability that the photon is not absorbed traveling up to the point x and the probability that it is absorbed in the dx, that is:

$$P(x) = e^{-\alpha x} dx \Rightarrow F(x) = \frac{\int_0^x P(x')\,dx'}{\int_0^\infty P(x')\,dx'} = \frac{\int_0^x e^{\alpha} x'\,dx'}{\int_0^\infty e^{\alpha} x'\,dx'} = [1 - e^{-\alpha x}] \tag{5.3}$$

The probability that an incident photon creates an electron-hole pair depends on the

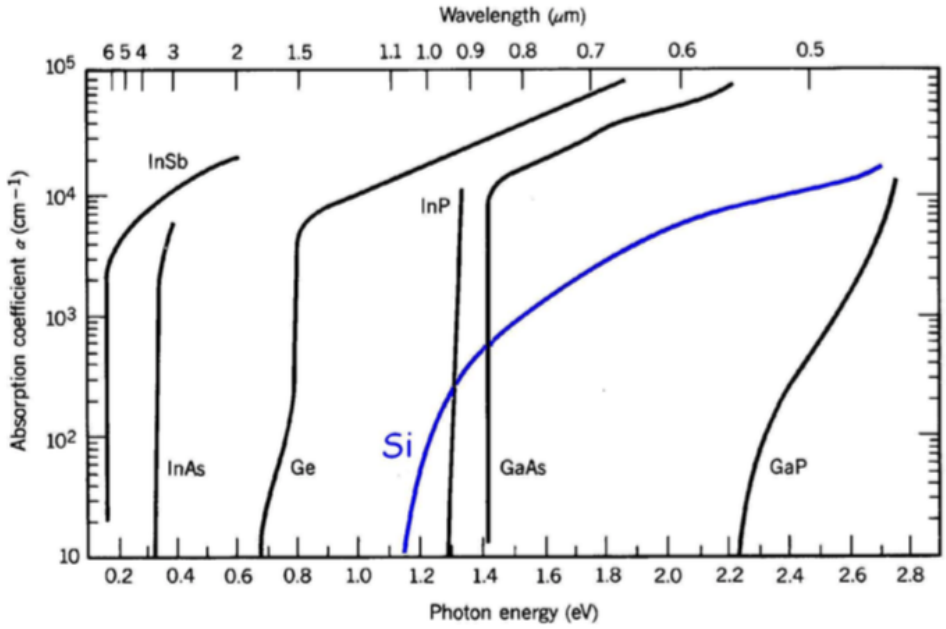

Figure 5.5: *Absorption coefficient for different semiconductors as a function of incident photon wavelength and energy.*

photon energy, which is related to its wavelength, following the law:

$$E = h\nu = \frac{hc}{\lambda} \Rightarrow \lambda = \frac{1.24}{E}\ \mu m \tag{5.4}$$

From Figure 5.5, it is clear that a critical wavelength λ_c exists beyond which the photon absorption coefficient drops too much to effectively use the device as a photodevice.For instance, for the Silicon (with an energy gap of 1.11 eV) the maximum detectable wavelength is ?1200 nm.

5.3 Photodiode

Photodiodes are devices that generate a current or voltage when the PN junction in the semiconductor is irradiated by light. In Figure 5.6 a reverse biased *p-n* junction is

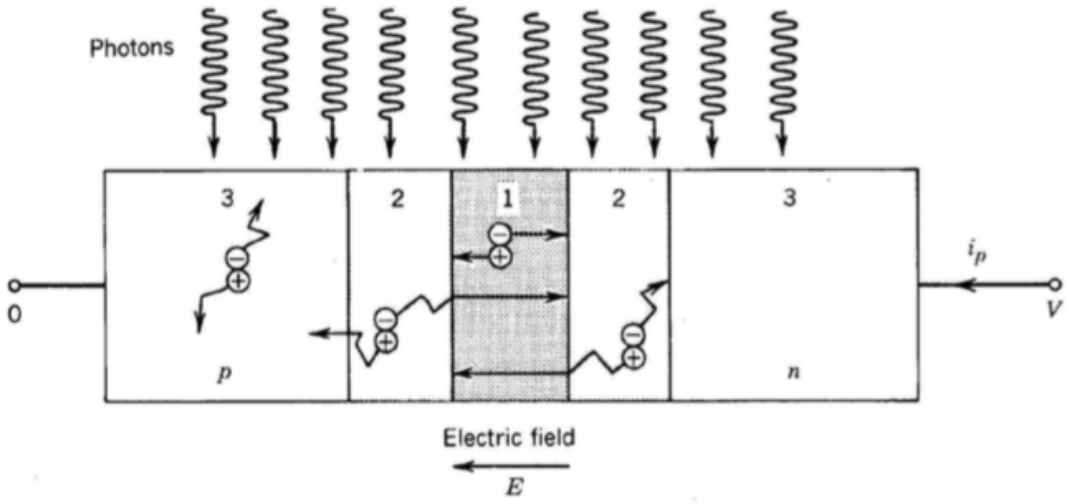

Figure 5.6: *Photon illuminating an ideal reverse-biased* p-n *photodiode.*

shown. When a photon is absorbed it produces an electron-hole pair but depending on the region where the absorption occurs, different effects can occur [34]:

- **A photon is absorbed in region 1:** pairs are generated in the depletion region. Carriers pair is swept from the junction by the electric field of the depletion region and carriers drift in opposite directions.. Electrons move to the *n* side and holes to the *p* side so that the photocurrent produced in the external circuit is in the reverse direction, i.e. from the *n* to *p* region.

- **A photon is absorbed in region 2:** electron-hole pairs generated close to the depletion region have a possibility to enter in the depletion region thanks to a random diffusion. An electron (hole) coming from the *p* (*n*) side is transported across the junction producing current in the external circuit

- **A photon is absorbed in region 3:** carriers pairs are produced away from the depletion region and cannot be transported because of the absence of electric field. After random diffusion they are re-absorbed by recombination and do not contribute to the external current.

As electronic device, the photodiode has an I-V relation given by:

$$I = I_s \left[e^{\frac{eV}{k_B T}} - 1 \right] - I_P \tag{5.5}$$

that is the usual I-V relation for a *p-n* junction with the addition of the photocurrent ($-I_P$), which is proportional to the photon flux. An example of I-V curve is reported in Figure 5.7

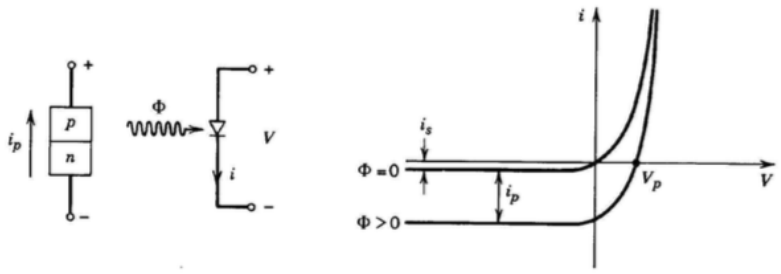

Figure 5.7: *I-V curve for a photodiode.*

5.3.1 Avalanche photodiode (APD)

An APD is a *revese-biased* photodiode where the applied electric field is so large that the carriers accelerate acquiring enough energy to excite other carriers by the impact ionization process. As shown in Figure 5.8 a photon absorbed in point 1 creates an electron-hole pair, in particular the electron in the conduction band and the hole in the valence band. Due to the strong electric field the electron accelerates increasing its energy with respect to the bottom of the conduction band. However the acceleration process is constantly interrupted by random collisions in which the electron loses part of its energy.
If the electron acquire an energy greater than the energy gap E_g it can generate a second electron-hole pair by impact-ionization (point 2), these two electrons accelerate under the effect of the field and can give origin to further impact ionization. Concerning the holes generated in point 1 and 2, they accelerate too and can impact-ionize too. The ability of carriers to impact-ionize is described using two ionization coefficient α_e and α_h, which represent the ionization probability per unit length for

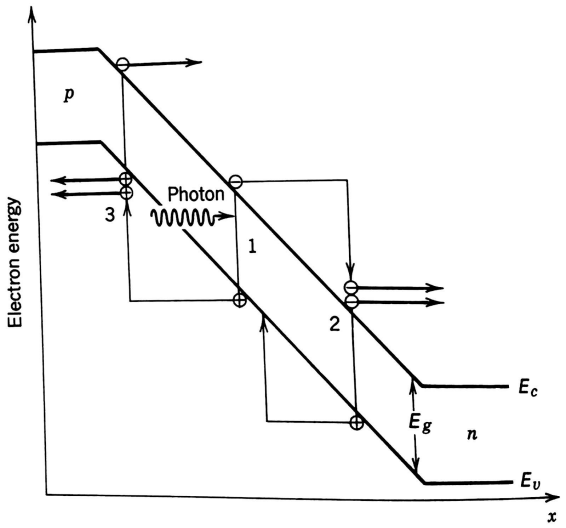

Figure 5.8: *Sketch of the multiplication process in an avalanche photodiode (APD).*

electrons and holes respectively. An important parameter to take into account in characterization of anAPD is the ionization ratio κ:

$$\kappa = \frac{\alpha_h}{\alpha_e} \tag{5.6}$$

The ionization probability is directly proportional to the depletion layer electric field and decreases with the increasing device temperature. Indeed as the lattice vibration grows the number of collisions increases too reducing their mean free path and avoiding the carriers to acquire sufficient energy to ionize between collisions.

5.3.2 Gain

The simplest way to determine the gain of an APD is to consider a single-carrier (electrons[2]) causing the multiplication. In this case we have $\alpha_h = 0 \rightarrow \kappa = 0$. Let $J_e(x)$ be the electron current density at a location x, its rise can be described as:

$$\frac{dJ_e(x)}{dx} = \alpha_e J_e(x) \;\Rightarrow\; J_e(x) = J_e(0)e^{\alpha_e x} \tag{5.7}$$

Defining the gain as the ratio between the current density in w, that is the multiplication layer width, to the current density in the point where photon absorption generates the electron-hole pair, it is obtained:

$$G = \frac{J_e(w)}{J_e(0)} \;\Rightarrow\; G = e^{\alpha_e w} \tag{5.8}$$

[2]It is possible to assume the current to be generated only by electrons. The holes have a similar but opposite behavior in their reference frame

As reported in Eq. 5.8, the current density exponentially increases with the absorption coefficient and depletion region width.
Instead considering a double carrier multiplication problem both electrons and holes current density, J_e and J_h has to be known. Assuming that only electrons are injected in the multiplication region and remembering that holes ionization also produces electron the variation of $J_e(x)$ can be expressed as:

$$\frac{dJ_e}{dx} = \alpha_e J_e(x) + \alpha_h J_h(x) \tag{5.9}$$

From the charge conservation $\frac{dJ_e}{dx} = -\frac{dJ_h}{dx}$, that is the sum $J_e + J_h$ has to be constant under steady state conditions. Since no holes are injected at $x = w$, $J_h(w) = 0$ and thanks to continuity of the current density $J_e(x)+J_h(x) = J_e(w)$ (Figure 5.9). Therefore

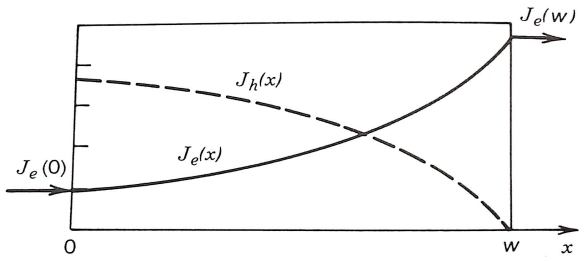

Figure 5.9: *Distribution of the electron and holes current density as a result of the avalanche multiplication.*

it is possible to write $J_h(x) = J_e(w) - J_e(x)$ in Eq. 5.9, obtaining:

$$\frac{dJ_e}{dx} = (\alpha_e - \alpha_h)J_e(x) + \alpha_h J_e(w) \tag{5.10}$$

Introducing the ionization ratio κ it is possible to describe the gain as:

$$G = \frac{1-\kappa}{e^{[-(1-\kappa)\alpha_e w]} - \kappa} \tag{5.11}$$

When $\kappa = 0$ the single carrier multiplication is obtained and the gain is expressed as in Eq. 5.8, when $\kappa \to \infty$ G=1 since only electron are injected and the do not multiply. For $\kappa = 1$ the gain is indeterminate and it has to be obtained from Eq. 5.10. The gain dependence on $\alpha_e W$ for several value of κ is shown in Figure 5.10.

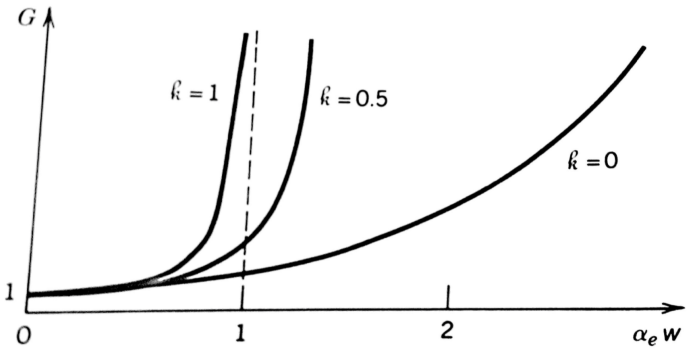

Figure 5.10: *Growth of the gain with the multiplication-layer width for several values of the ionization ratio* ρ.

5.3.3 APD in Geiger mode

When the reverse voltage applied to an APD is set higher than the breakdown voltage[3], the electric field in the APD becomes high enough to cause a discharge (Geiger discharge) even by input of one single photon as shown in Figure 5.11. For a photo-

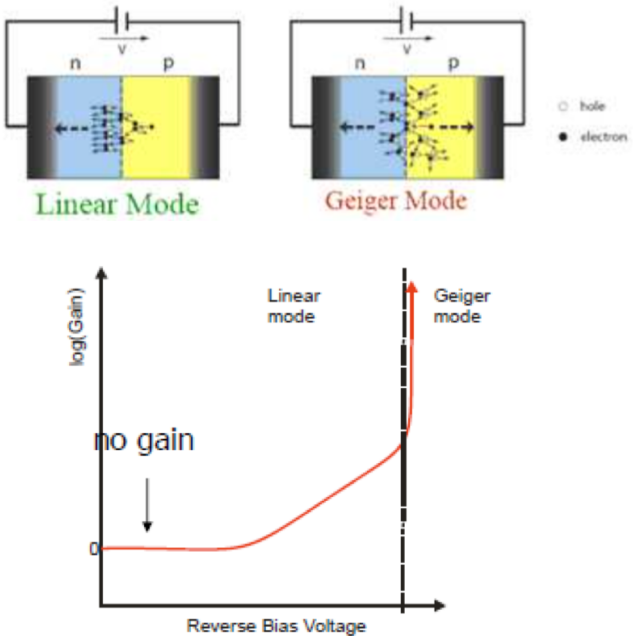

Figure 5.11: *ADP in linear and geiger mode.*

[3]The breakdown voltage V_{br} is the minimum(reverse) bias voltage that leads to self-sustaining avalanche multiplication

diode operated in Geiger mode, the avalanche caused by injection of a single charge carrier does not stop but it is self-sustained so that the gain values are $G \sim 10^6$. When a photon begins an avalanche in Geiger mode it is not possible to detect another photon arriving. since the Geiger discharge continues as long as the electric field in the APD is maintained, to usefully exploit a sensor in Geiger mode the discharge should be quenched. One specific example of limiting the discharge time is based on the application of a quenching resistor connected in series with the APD. The avalanche multiplication in the APD is quickly stopped due to a drop in the operating voltage occuring when the output current, caused by the Geiger discharge, flows. A sketch of this quenching techniques is reported is Figure 5.12. When $t < t_0$

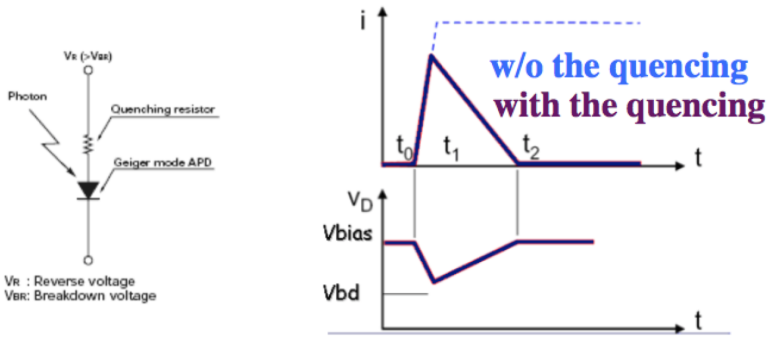

Figure 5.12: *Quenching techniques: (left) schematic equivalent circuit, (right) time diagram.*

the current does not flow, at $t = t_0$ the avalanche begins and propagates in $t_0 < t < t_1$; when $t > t_1$ avalanche is self-maintained, current value is limited thanks to quenching resistor.

5.4 Silicon Photomultipliers (SiPM)

SiPMs are photon-counting devices consisting of an array of light-sensitive elements, the pixels[35]. Pixels are all connected in parallel and externally biased by a single voltage source, as shown in Figure 5.13. Each pixel is a series combination of an APD and a quenching resistor . By design, all pixels are identical in shape, dimension and construction features.

The sum of the output of each pixel forms the SiPM output. Assuming all pixels to be identical and producing the same charge while absorbing a photon the number of pixel fired can be deduced by just measuring the total charge output. Indeed, the charge output will be a multiple of the charge emitted by a single pixel fired, hence it

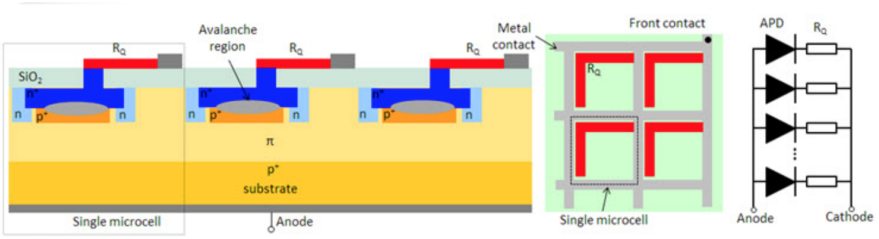

Figure 5.13: *Sketch and equivalent circuit of a SiPM.*

is clear that it is also possible to obtain the number of photons absorbed. In Figure 5.14 an analog output from a SiPM is shown, fired pixel detecting a photon in an array are shown in red in the right part of the figure. In the top right array a single photon is detected resulting in one photoelectron output. In the bottom right array three simultaneously detected photons are shown, thus resulting in a pulse with three times higher amplitude.

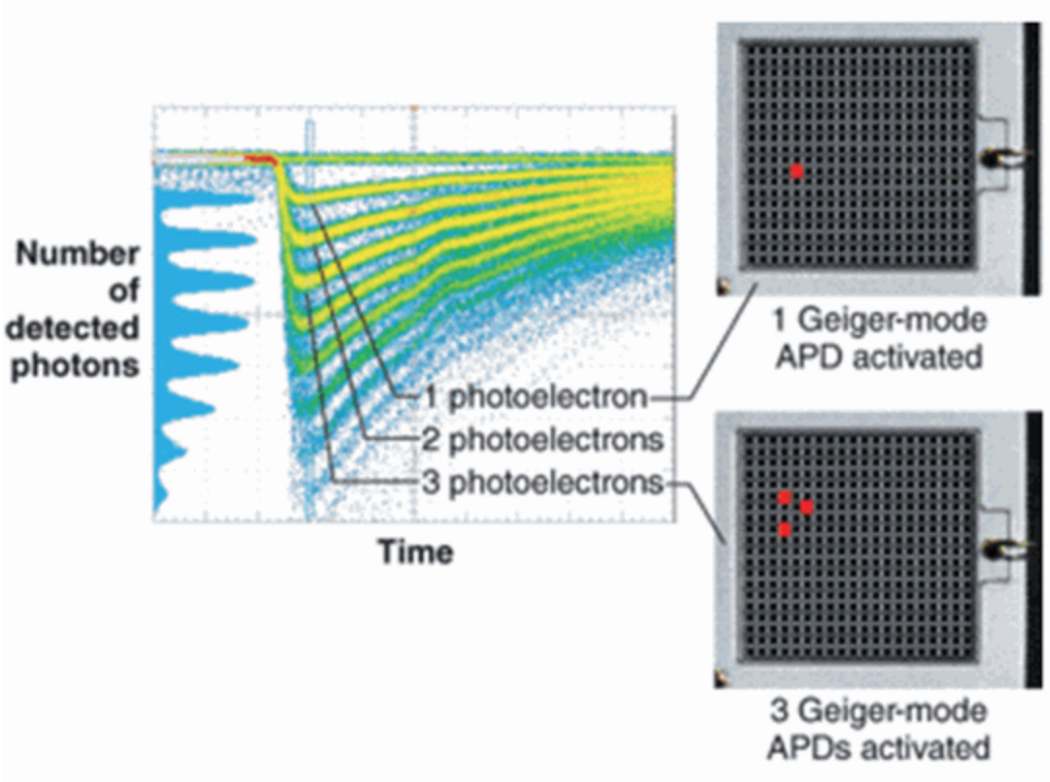

Figure 5.14: *Sketch and equivalent circuit of a SiPM.*

While a single pixel can be considered as a digital device, since it emits a well defined charge while detecting a photon, the entire SiPM can be considered as an analog device, but with specific properties of non linearity in response and saturation.

5.4.1 Gain

The gain of a SiPM is directly proportional to the reverse-biased polarization voltage applied. If we consider a SiPM as a parallel-plate capacitor it is possible to express the gain as:

$$G = \frac{Q}{e} = \frac{(V_{bias} - V_{br})C_{pixel}}{e} \tag{5.12}$$

where C_{pixel} is the capacitance of a single pixel and V_{br} is the breakdown voltage. The greater the capacitance, the greater is the gain. We underline that the pixel capacitance decreases with the increase of the bias voltage following equation:

$$C_{pixel} = \epsilon \frac{A}{L},\ L \propto \sqrt{V_{bias}} \tag{5.13}$$

where A is the junction area, L the lenght of the depletion region and ϵ the electric permittivity of the semiconductor. Even if the increase of L with the bias voltage causes the decrease of the pixel capacitance, at high value of bias voltage, the typical of the Geiger mode, the capacitance of the depletion region, which is lacking of carriers, is almost constant (see Figure 5.15) [36].

It is important to underline that the breakdown voltage is temperature dependent so

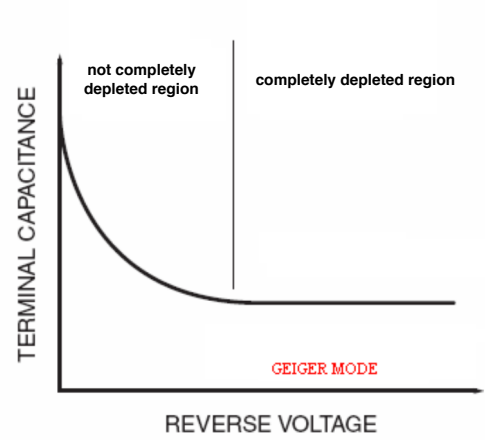

Figure 5.15: *Deplection region capacitance as a fuction of the bias applied.*

that even gain of a single pixel depends on temperature. In a semiconductor the total resistance varies with the temperature following the law:

$$R = R_0(1 - \alpha T),\ \alpha = \frac{\beta}{T_0^2} \tag{5.14}$$

where R_0 is the resistance at T_0 and β depends on the particular silicon device. Decreasing the resistance, the voltage drop on the SiPM decreases and consequently, from Eq. 7.4, the gain decreses too.

5.4.2 Photon Detection Efficiency

Considering a SiPM, the Photon Detection Efficiency (PDE) and in particular its variation with the wavelength of incoming photons (shown in Figure 5.16) has to be addressed.

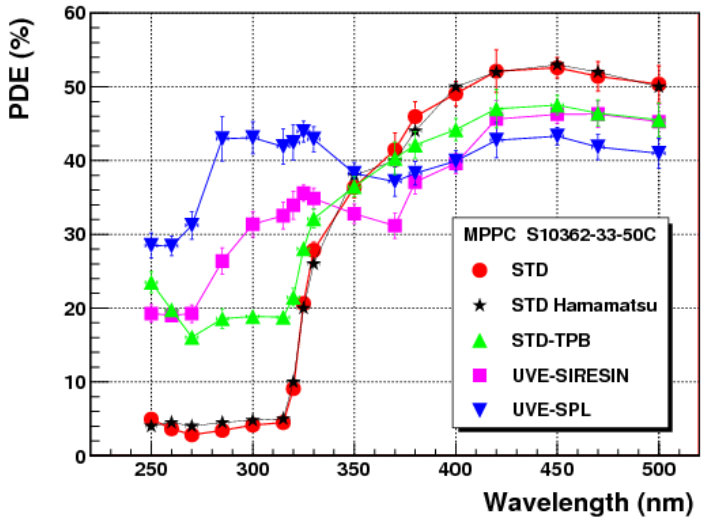

Figure 5.16: *Photon detection efficiency as a function of the wavelength for four SiPM prototypes from Hamamatsu.*

The PDE is the product of three factors:

- **Quantum Efficiency (QE):** silicon photomultipliers QE peaks is in the visible spectrum, in particular around a wavelenght of $\sim 400\mu$m, that corresponds to blu-violet. QE could be expressed through the ratio of pixel fired to the effective number of incident photons.
- **Fill Factor:** it is defined as the ratio of the effective pixels dimension and the SiPM total dimension. Typical values range between $\sim 30\%$ and $\sim 80\%$.
- **Avalanche Probability:** is the probability that a photon absorbed in the depletion region can begin an avalanche.

5.4.3 Dark Current

Dark current originates when, due to a thermal fluctuation, an electron-hole pair is created in the depletion region of a SiPM pixel. In this case, the charge carrier can enter the avalanche region and start an avalanche indistinguishable from the one resulting from photon absorption. Less likely the pair can be thermally created in the

avalanche region. The creation of an electron-hole pair is due to the the presence of generation-recombination centers (called traps), generated because of lattice imperfections, with an energetic level between the valence and the conduction band.The dark current depends on overvoltage, temperature, pixel size and quality of the chosen material. Considering only a trap level, tthe dark current can be written as:

$$i_{dark}(t) \propto -\frac{dn}{dt} = nP,\ P = \frac{1}{\tau} \propto e^{-\frac{E}{kT}} \tag{5.15}$$

where P is the probability that in a time unit an electron could flow to the conduction band and E is the energy level corresponding to a trap.

5.4.4 Afterpulsing

During an avalanche multiplication in a SiPM pixel, the carriers could be trapped by lattice defects. The output could contain some spurious signals appearing with a time delay from the light input to the SiPM. An example of these signals, called afterpulses, is shown in Figure 5.17. The aftepulsing can greatly increase the dark rate and cause distortions in the arrival time distribution of the photons. The probability

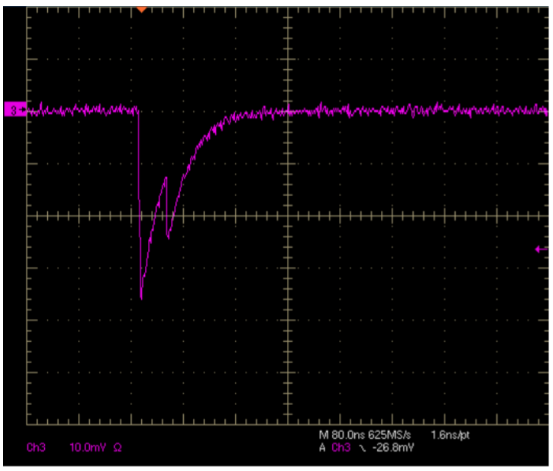

Figure 5.17: *Afterpulse in a 100 pixels SiPM.*

of afterpulsing can be expressed as follows:

$$P_{afterpulse}(t) = P_{trap}\frac{e^{-\frac{t}{\tau}}}{\tau}dtP_{avalanche} \tag{5.16}$$

where P_{trap} is the probability that a carrier is trapped, τ is the mean time that a carrier spends in a unstable energetic level (a trap) and $P_{avalanche}$ is the probability an avalanche starts. Since the avalanche probability increases with the applied bias it is clear that the probability of afterpulsing grows too. Moreover the traps density

is directly proportional to the pixel surface so that the probability of afterpulsing increases with the pixel dimensions.

5.4.5 Dynamics

The dynamic range of a detector can be defined as the optical signal level range over which the detector provides a useful output. For a SiPM, this range extends from the lowest signal level detectable to the optical signal level that results in all the SiPM microcells detecting photons simultaneously (within the microcell dead-time). At this point the output signal completely saturates since no more microcells are available to detect incoming photons, until some of the microcells have recovered back to their sensitive (charged) state.
The dynamic range for simultaneously incident photons is determined by the number of pixels excited and the PDE of the SiPM. As the number of incident photons increases, two or more photons can hit a single pixel. Since each pixel can only detect a single photon, the output linearity degrades as the number of incident photons increases. The number of excited pixel (N_{fired}) can be described using the following equation:

$$N_{fired} = N_{tot} \times \left[1 - exp\left(\frac{-N_{photon} \times PDE}{N_{tot}}\right)\right] \tag{5.17}$$

where N_{tot} is the total number of pixel, $n_{photons}$ is the number of incident photons and PDEm is the photon detection efficiency. It is possible to wide the SiPM dynamic range increasing the photosensitive area or using pixel with a narrower pitch.

5.4.6 Radiation damage in silicon detector

The main effects due to radiation damage can be summarized in two classes : bulk damage, caused by the displacement of crystal atoms, and surface damage, which include all effects in the covering dielectrics and the interface region [42].

Considering a macroscopic scale,irradiation damage causes:

- increase of leakage current and noise,
- change in material resistivity,
- reduction in the amount of collected charge due to the charge carrier trapping mechanism,
- decrease of the carrier's mobility and their lifetime

Bulk damage

A bulk damage is caused by the interactions of the incident particles with the nuclei of the lattice atoms. Differently from ionization, such interactions are not always reversible. To remove a silicon atom from its lattice position a minimum recoil energy E_r of about 25 eV is required. Electrons need an energy of at least 260 keV in order to provide such a recoil energy in a collision, while protons and neutrons, because of their higher mass, require only 190 eV.
Considering low energy electrons and x-ray photons, a small energy is delivered to the recoil Si atom; isolated displacements are created, leaving a single vacancy-interstitials pairs. If the recoiling silicon atom receives enough energy through the collision, that is about 5 keV, it is able to displace other Si atoms in the crystal. Since these displacements are closely situated, most of them repair and only 2% of all generated defects form electrically active states. Such disordered regions are referred to as defect clusters, which can have high local defect density and can be ≈ 10 nm wide. Both point defects and clusters can have severe effects on the detector performance, depending on their concentration, energy level and the respective electron and hole capture cross-section. Defects with deep energy levels in the middle of the forbidden gap could act as recombination/generation centers and could be responsible of an increase of the reverse current.
Moreover, these defects could also act as trapping centers affecting the charge collection efficiency. The trapping is due to the different time constants of the electron capture and emission processes. Traps are mostly unoccupied in the depletion region due to the lack of free charge carriers and can hold or trap parts of the signal charge for a time longer than the charge collection time and so reduce the signal height.

Surface damage

Surface damage summarizes all defects in the overlaid dielectrics and the interface between the silicon and the dielectric. The passage of an ionizing radiation in silicon detectors creates e-h pairs that are collected by the electric field at the electrodes and form the signal. In the undepleted bulk of the semiconductor, where there is no electric field, the high carrier density allows the deposited charge carriers to recombine. Therefore, the semiconductor does not show permanent traces of the passage of a charged particle that loses energy by ionization.

On the contrary, the passage of an ionizing radiation in the oxide causes the built up of trapped charge in the oxide layers of the detector. The e-h pairs created in the oxide either recombine or move in the oxide electric field: the electrons towards the

SiO_2-Si interface, the holes towards the metallic contact. The higher mobile electrons escaped from the recombination are injected into the silicon bulk, in a typical time of $\sim$ 100 ps. The less mobile holes can be trapped at the SiO_2-Si interface. This trapping results in an increase of the oxide positive charge, therefore in a degradation of the oxide quality. In addition to the trapped charge, the ionising radiation also produces new energy levels in the band gap at the SiO_2-Si interface. These levels can be occupied by electrons or holes, depending on the position of the Fermi level at the interface and the corresponding charge can be added or subtracted to the oxide charge.

Chapter 6

Test Beam

At the beginning of the Mu2e project, in 2008, the crystals under consideration for the calorimeter were made of $PbWO_4$ soon replaced by the LYSO crystals, that well met the experiment requirements. LYSO has indeed a very high light output, a small Molière radius, a fast scintillation decay time, excellent radiation hardness and a scintillation spectrum well-matched to an APD readout.
Due to the sudden increase of LYSO price, two more options, cheaper and lighter, were proposed during the CD-2[1] review: BaF_2 crystal readout by APD and CsI crystal readout by SiPM as a backup solution. Since the CsI crystals coupled to UV-extended SiPMs resulted the easiest choice to take, at the end of 2015 it was decided to build the calorimeter using CsI crystal. One of the most convincing argument was the results from a dedicated test beam with an electron beam performed at the Test Beam Facility (BTF(at INFN Frascati National Laboratories (LNF), where a smaller prototype of CsI and SiPM was tested. In this chapter a short summary of this test is presented.

6.1 Experimental set-up

A small matrix made of nine $3 \times 3 \times 20$ cm^3 undoped CsI crystals (Figure 6.1), readout with UV-extended SiPMs, has been exposed to an electron beam of 80-130 MeV at LNF BTF in April 2015.

The matrix crystals from Opto Materials [32] and from ISMA [33] have been used. Each crystal has been wrapped with 150μm thick Tyvek. The back side of each crystal has been coupled to a large area 12×12 mm^2 photosensor by means of the optical grease Rhodosil 7 silicon paste.
In order to sum all the signals from the photosensors and provide an amplification of

[1] Critical Decision-2, approve Performance Baseline

Figure 6.1: *Left: SiPM holder. Right: matrix assembled.*

8, a custom FEE board has been designed. Two $5\times1\times1$ cm^3 plastic finger scintillators, crossed at 90° were placed in front of the matrix providing, in time coincidence, the beam trigger. Moreover, a $10\times30\times4$ cm^3 scintillator was positioned above the matrix defining a cosmic rays trigger.
Signals from counters and SiPMs have been readout and digitized by 12 bit, 25 MHz WF digitized board from CAEN.
As shown in Figure 6.2 two different configurations were tested:

- 0°, that is beam orthogonal to the prototype front face.
- 50°, incident angle typical for the conversion electrons in Mu2e.

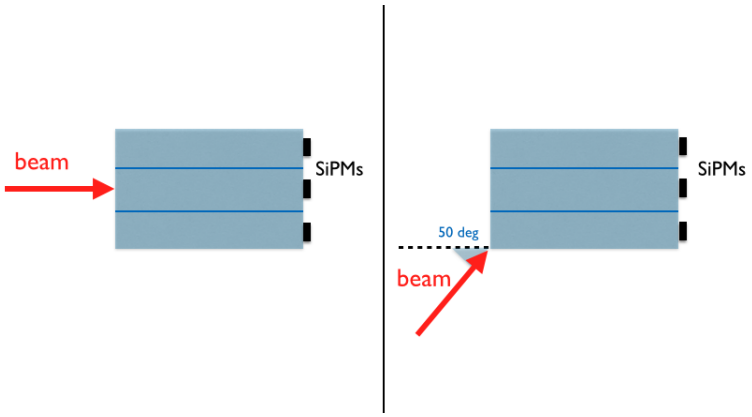

Figure 6.2: *Beam test configuration. Left: beam normal to the prototype surface. Right: bean at* 50° *to the prototype surface.*

6.2 Energy response and energy resolution

The cross calibration of the calorimeter channels has been set using both the response to MIPs and to a scan with the beam in each crystal. The energy scale has

been done with e^- considering several sets of orthogonal run with different energies (80,90,100,110,120 MeV).
In Figure 6.3 the peaks resulting of a Lognormal fit to the charge distribution are reported as a function of the average deposited energy estimated by simulation for different beam energy. The charge values are fitted with a linear function. The in-

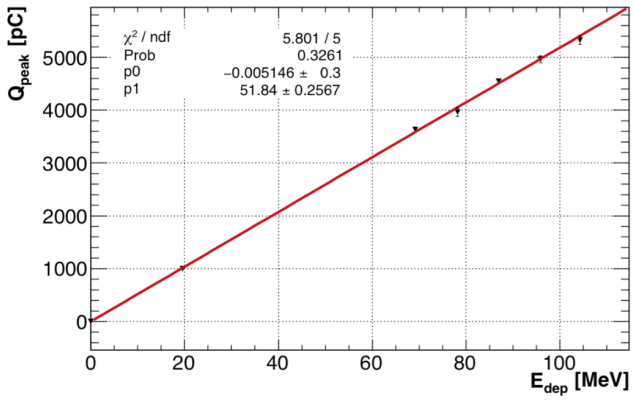

Figure 6.3: *Peak value of the reconstructed total charge of the prototype in the calibration runs as a function of the deposited energy. The red line represents a linear fit.*

tercept is compatible with 0 and the slope, $k_{cal} \approx 52$ pC/MeV is used as energy scale. Considering the total gain provided by the SiPMs and the amplification system, this corresponds to an average light yield of ≈ 32 pe/MeV. Hence, the total calorimeter energy can be calculated as $E_{tot} = Q_{tot}/k_{cak}$.

The energy resolutions has been evaluated from the σ of the Lognormal fit, as a

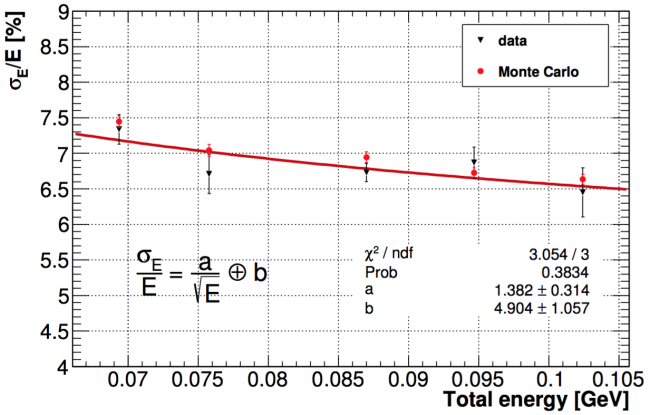

Figure 6.4: *Comparison between energy resolution from data (black) ad Monte Carlo (red).*

function of E_{dep}, as reported in Figure 6.4. The energy resolution measured ranges

from 7.4% to 6.5% in the energy deposition range (70, 102) MeV and is dominated by energy leakage. Monte Carlo and data are in agreement within the uncertainties.

6.3 Time resolution

The time resolution has been measured in different ways:

- using only the crystal with the highest energy deposition;
- using the mean time from all crystal weighted with the energy: $T_{mean} = \sum(T(i,j)E(i,j))/\sum E(i,j)$, where T(i,j) is the crystal time of a the cell in row i and column j, as evaluated with the Constant Fraction method (see Section 7.2).

Since the shape of the recorded signal waveforms has been found to be dependent on the integrated charge, the signals used for timing measurements were required to have a deposited energy above 10 MeV. In Figure 6.5 this dependence of the length of the waveform leading edge, $t_{peak} - t_{crystal}$, on the energy deposited in the crystal is shown. In Figure 6.6 an example of the central crystal time distribution for 100 MeV

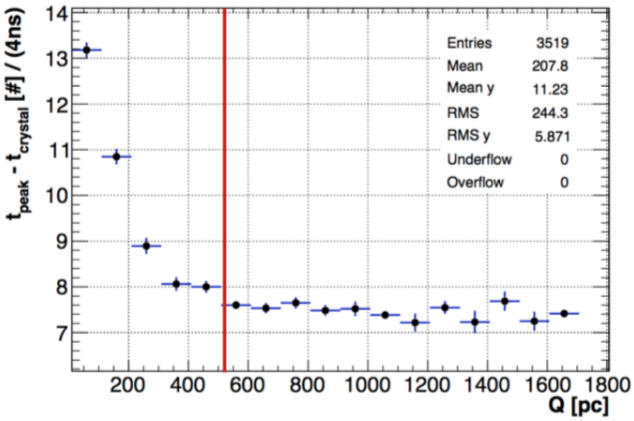

Figure 6.5: *Pulse rising time as a function of the signal reconstructed charge. The red line indicates the 10 MeV equivalent threshold.*

electron beam is shown.
The leading edge time distribution is fit with a gaussian, the σ of the fit is used to evaluate the resolution. The time resolution, as a function of the energy deposited in the crystal, is shown in the right side of Figure 6.6. The time resolution varies from 130 ps, at 45 MeV, to 110 ps, at 69 MeV of deposited energy in the crystal with high energy (corresponding to 80 and 120 MeV beam momentum respectively).

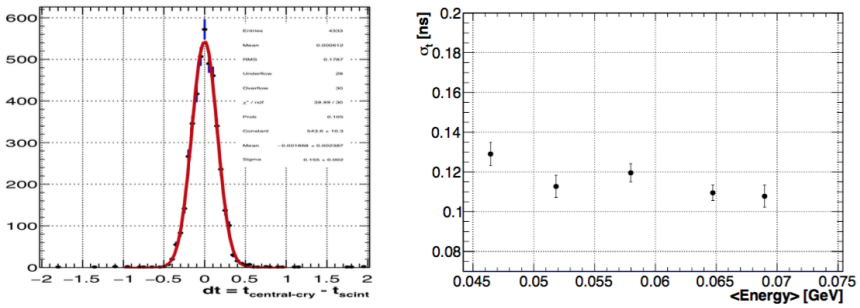

Figure 6.6: *Left: example of the central crystal time distribution for 100 MeV electron beam. Right: time resolution of the most energetic crystal as a function of the mean energy deposited in the crystal.*

Similarly, in Figure 6.7 left an example of the timing distribution for 100 MeV electron beam is shown for the energy weighted time, T_{mean}. The obtained time resolution as a function of the mean deposited energy is reported in Figure 6.7. The time resolution varies from 120 ps, at 53 MeV, to 105 ps, at 82 MeV of energy deposition (corresponding to 80 and 120 MeV beam momentum respectively, after the application of the 10 MeV threshold).

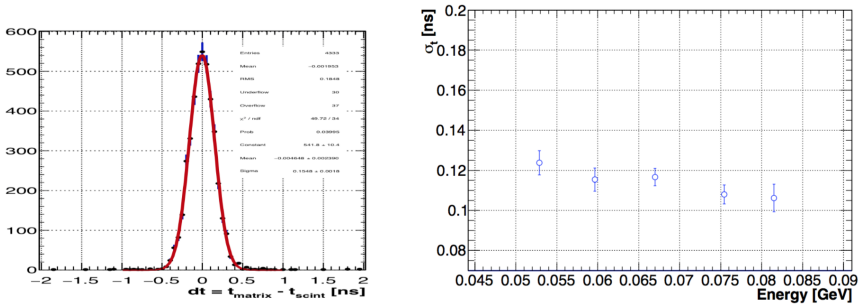

Figure 6.7: *Left: example of the weighted energy time distribution for 100 MeV elec- tron beam. Right: time resolution of the energy weighted mean time as a function of the mean energy deposited in the matrix.*

Chapter 7

Design and characterization of the Mu2e SiPM and crystal

In this chapter, the results of our characterization of seven large area UV extended SiPMs from Hamamatsu [38] are described. The SiPM specifications are reported in Table 7.1. Results from irradiation test and measurements of the crystal light output are also reported.
First of all, the description of the time characterization and the timing resolution achieved with SIPM in series configuration is presented.
Then, the methods for the measurements of the dark current and of the gain are described; the latter one is obtained looking at the photon peaks in the charge spectrum. The result of neutron irradiation performed on SiPM at the HZDR center in Dresden and the behavior of an array of 3 SIPMs in series configuration both with all SiPMs non irradiated or with one of them strongly irradiated are reported. The variation of the charge resolution in the latter case is shown.
To correct the large increase of leakage current due to irradiation we need to cool down the SiPMs. A study of the dependence of the SiPM parameters with temperature has been carried out.

Pixel pitch [μm]	50
Effective photosensitive area [mm]	6.0×6.0
Number of pixel	14400
Window material	Silicon resin
Gain (at 25°)	1.7×10^6
PDE @ 310 nm	30%

Table 7.1: *SiPM series 13360-6050CS specifications.*

The needs and the method use to characterize the Mean To Time Failure of these devices is described.
Finally studies concerning crystal specifications tests are reported.

7.1 Description of the Mu2e custom SiPMs

A modular SiPM layout has been chosen in order to enlarge the active sensor area in order to maximize the number of collected photoelectrons from the crystal.
To optimize the granularity and the acceptance the crystal dimension has been increased (after CD-2) from 30×30 mm^2 (dimension reported in the TDR) to 34×34 mm^2 thus allowing to accomodate two arrays of 2×3 individual 6×6 mm^2 UV extended SiPM modules (see Figure 7.1). This was impossible with the previous crystal dimension because of problems related to mechanics, that is the Front End Electronics lack of space. Although the requirements on the light collection are met with a single photosensor, the second SiPM in the crystal ensure redundancy.
The photosensors are coupled to the crystals without using grease or glue.
A serial connection has been chosen in order to overcome some issues related with

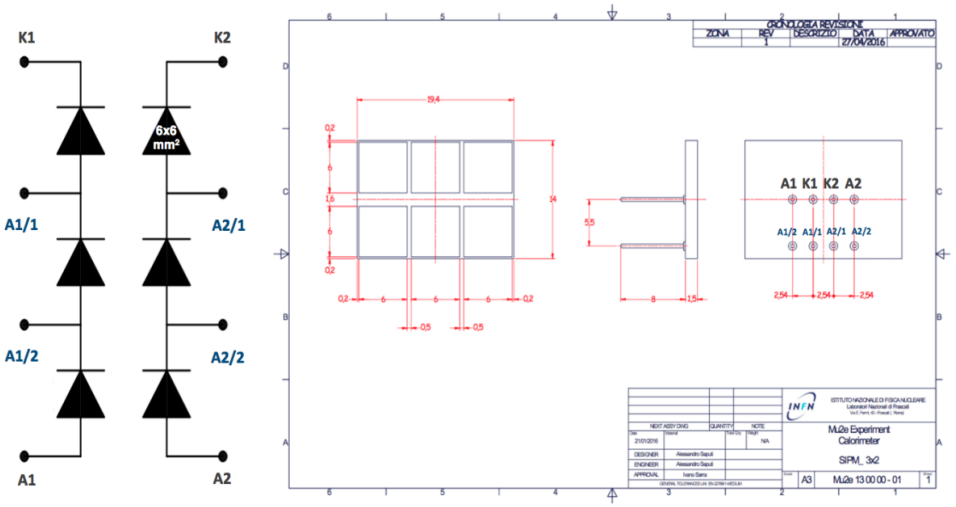

Figure 7.1: *Sketch and schematic structure (from left to right) of the front, cross and back side of the 3360-6050CS Hamamatsu MPPC(Multi-Pixel Photon Counter).*

parallel connection which may affect the energy and time measurements, in particular a very large capacitance resulting in an increased noise and an increased signal rise time and width.
When connecting SiPM in series configuration, the bias of each SiPM is regulated by the common dark current (I_{dark}) (more details in Sec. 7.3).

Differently from the parallel configuration, where the signal becomes wider, the pulse shape resulting from a series of SiPMs results narrower than that of a single SiPM. This is due to the reduction of the total capacitance of the series circuit, as reported in Figure 7.2. Moreover, the fast rise time improves the time resolution and the shorter signal decay time is relevant to minimize the overall width of the Crystal+SiPM pulse height thus improving the pileup discrimination capability.
A possible disadvantage of the series configuration is that the collected charge, which depends on the capacitance as explained in as explained in Subsec.5.4.1, is reduced to one third with respect to that of a single SiPM. However, this refers to the total charge which results smaller because of the reduced quenching time; the signal pulse height actually remains the same.

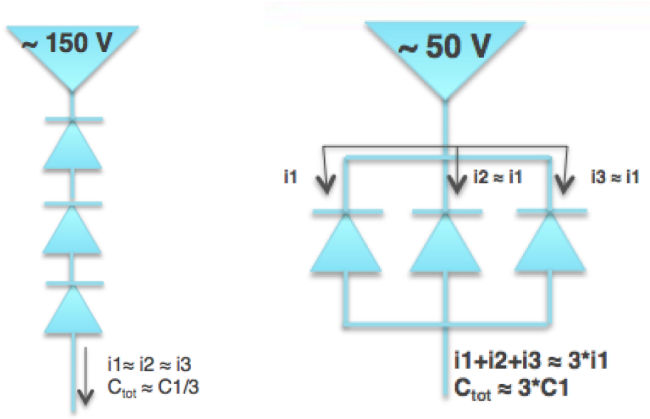

Figure 7.2: *Sketch of a parallel (left) and serial(right) SiPMs connection.*

7.2 Timing characterization of the SiPM series

In order to determine the time resolution of an array made of 6 Hamamatsu SiPMs (see Figure 7.1) in Mu2e configuration(Mu2e SiPM in the following) a test with cosmic rays has been performed.
To optimize the light collection, an undoped CsI crystal has been wrapped with a 15 μm-thick Tyvek foil, by covering the four faces along the crystal axis and the side opposite to the readout system. The crystal has been coupled with an air-gap to the Mu2e SiPM array and the whole system has been placed between two plastic scintillation finger counters as shown in Figure 7.3 (left). The polarization and amplification scheme are shown in Figure 7.3 (right).
The Mu2e SiPM signal is amplified through a custom fast amplifier by a factor of

~ 16.

The acquisition system is composed of a trigger board, which makes the coinci-

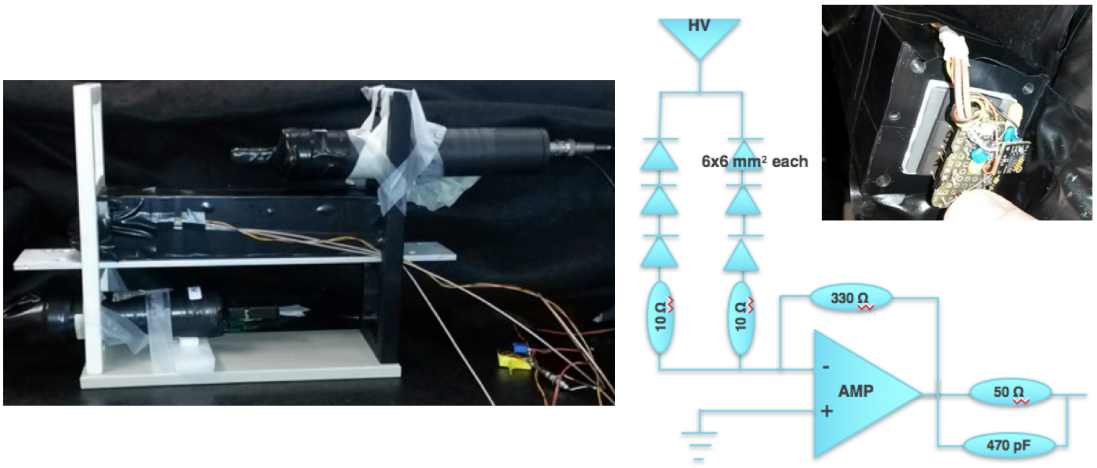

Figure 7.3: *Left: experimental setup used during the acquisition. Right: polarization scheme for* 2×3 *SiPMs array.*

dence between the two discriminated counter signals, and a desktop digitizer (CAEN DT5751, 1 Giga samples per second) which acquires finger and crystal signals.
Since previous measurements showed a dependence of the time from the charge, the measured time is taken at a constant fraction (CF), set at 20% of the maximum signal amplitude, which is fitted using a lognormal function:

$$f(t) = N exp\left(-\frac{ln^2[1-\eta(t-t_0)/\sigma]}{2s_0^2} - \frac{s_0^2}{2}\right)\frac{\eta}{\sqrt{2\pi}\sigma s_0} \tag{7.1}$$

where N is the normalization parameter, t_0 is the position of the peak, $\sigma = FWHM/2.35$, η is the asymmetry parameter and $s_0 = 0.85\ \text{arcsinh}(\eta 2.35/2)$. The experimental data and fit to a typical pulse are shown in Figure 7.4.

To eliminate the time jitter due to the trigger, the half sum of the finger time is subtracted to the crystal measured time:

$$t = t_c - \frac{t_1 + t_2}{2} \tag{7.2}$$

The time jitter of the trigger is evaluated as the σ obtained by the gaussian fit to the trigger time distribution, that is $\sigma_f = (255 \pm 12)$ ps.
In Figure 7.5 the time distribution, before the jitter subtraction, is reported. The time resolution after trigger jitter subtraction is evaluated as:

$$\sigma_t = \sqrt{\left(\sigma_c^2 - \sigma_f^2\right)} = 167.3 \text{ ps} \tag{7.3}$$

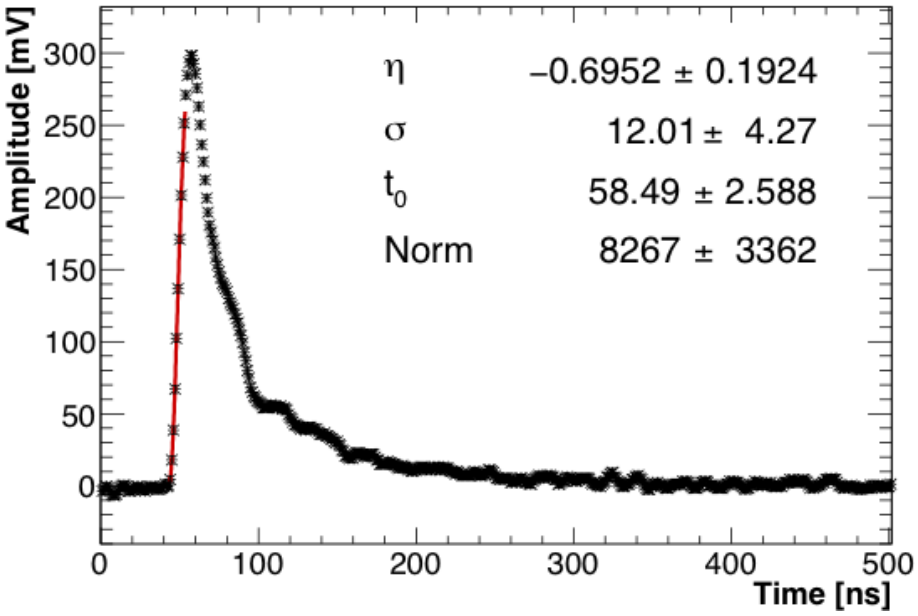

Figure 7.4: *Signal of the crystal acquired by the CAEN DT5751 digitizer.*

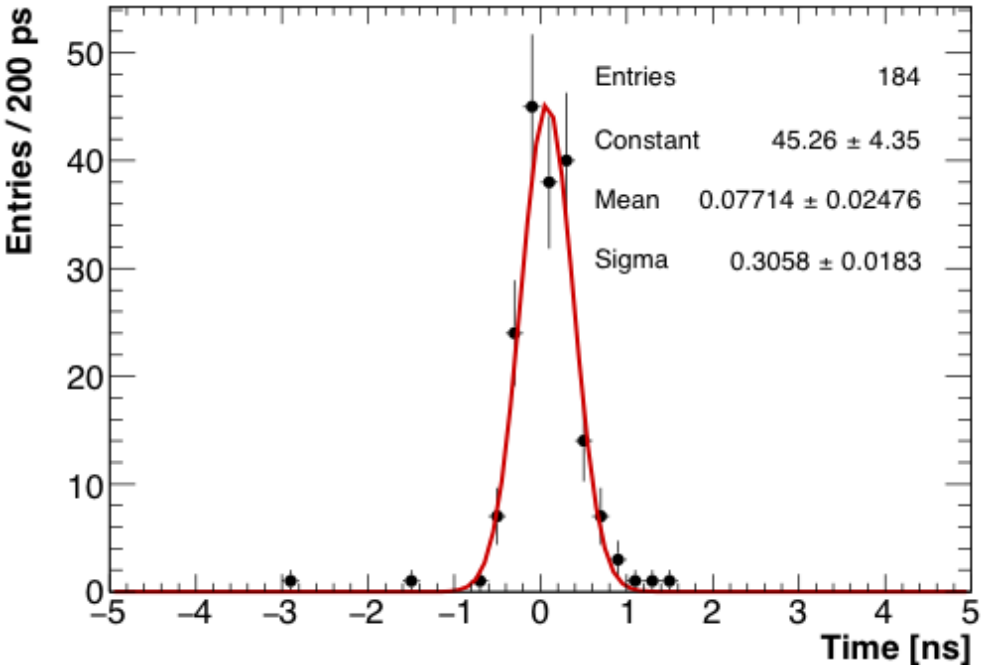

Figure 7.5: *Time distributions obtained with the constant fraction method.*

7.3 Study of the breakdown voltage, of the dark current and of the gain

7.3.1 Measurement of V_{br} and measurements of I_{dark}

In order to determine the breakdown voltage (V_{br}) and evaluate the gain and I_{dark} fluctuations at the same overvoltage, defined as the difference between the bias applied and the breakdown voltage. The dark current has been measured as a function of the applied bias for six 6×6 mm^2 Hamamatsu SiPMs. Each SiPM has been fixed on a support inside a black box and the I_{dark} value as a function of the bias applied has been recorded using a Keithley pico-ammeter, through an automatic acquisition program, that could read the voltage and current information with a programmable voltage step.
As shown in Figure 7.6, we can divide the plot in three different regions:

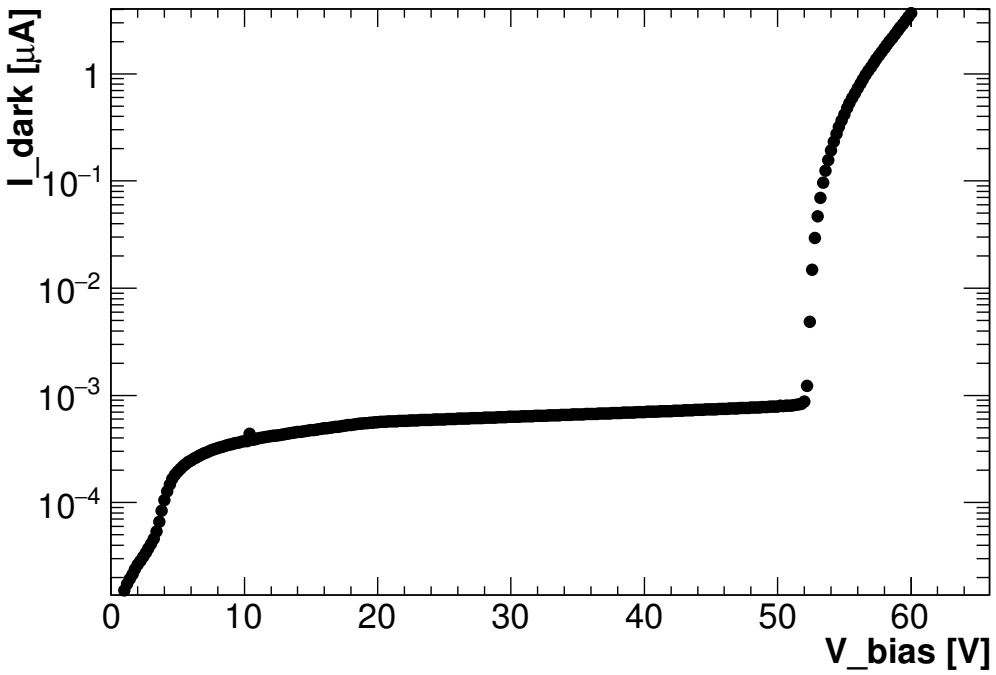

Figure 7.6: *I_{dark}-V curves for a SiPM from Hamamatsu.*

- **V$\ll V_{br}$:** the dark current, I_{dark}, monotonically increases with the applied bias. There are two main contributions to the dark current: the bulk current due to thermally generated charge carriers, that flows primarily in the depletion region, and the surface current that is due to defects at the Si-SiO2 interface.

- **V $\simeq V_{br}$ (APD region):** the carriers generated in the bulk begin to have enough energy to impact-ionize Si atoms in the avalanche section of the depletion region. The current now increases more rapidly with each voltage step, reaching the highest rate of increase when V= V_{br}.
- **V $> V_{br}$:** the devices operate in Geiger mode and the gain becomes linearly proportional to $\Delta V = V_{bias} - V_{br}$.

The increasing rate of the current with respect to the applied bias follows a low that is proportional to $(V - V_{br})^n$ in the first part of the rise and $e^{(V-V_{br})}$ in the following part, with $n > 2$ [39]. In order to determine the breakdown voltage of the SiPM and compare it with the one from datasheet, the derivative of the current curve in logarithm scale has to be calculated, as shown in Figure 7.7.

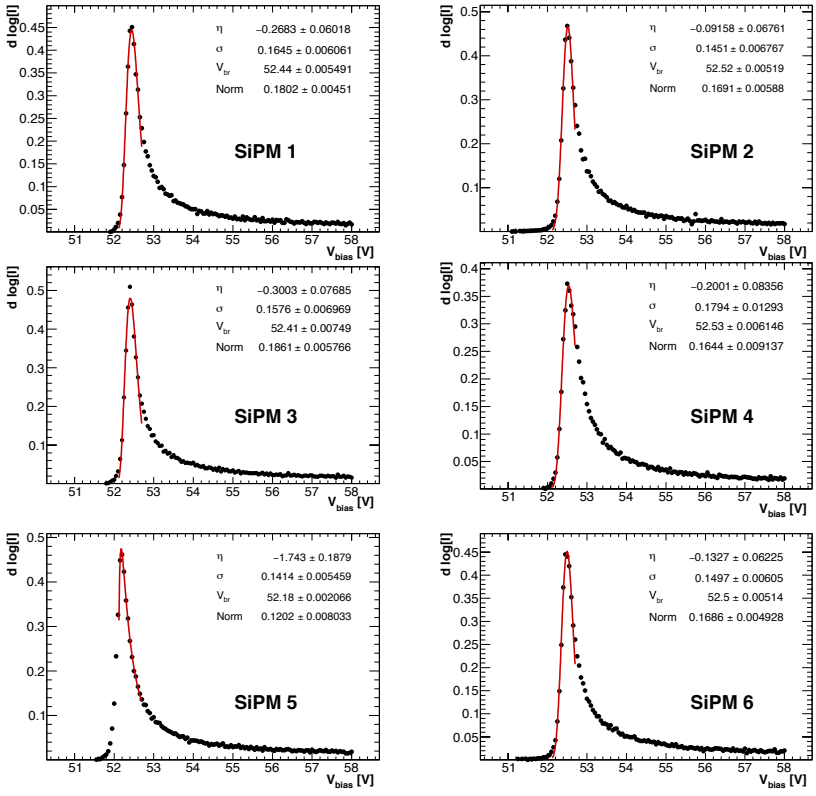

Figure 7.7: *Derivative of the I-V curves in logarithmic scale used to determine the SiPMs breakdown voltage.*

Calculating and plotting the derivative $\frac{dlog[(V-V_{br})^n]}{dV} = \frac{n}{V-V_{br}}$ as a function of V, the position of the local maximum, estimated with a log normal fit, represents the breakdown voltage. In Table 7.2 the fit results of our measurements compared with

the V_{br} estimated by Hamamatsu (as reported in their datasheet) for each SiPM are reported.
In order to verify that all the curves have the same shape we can plot the logarithm of the current as a function of the overvoltage, as shown in Figure 7.8.

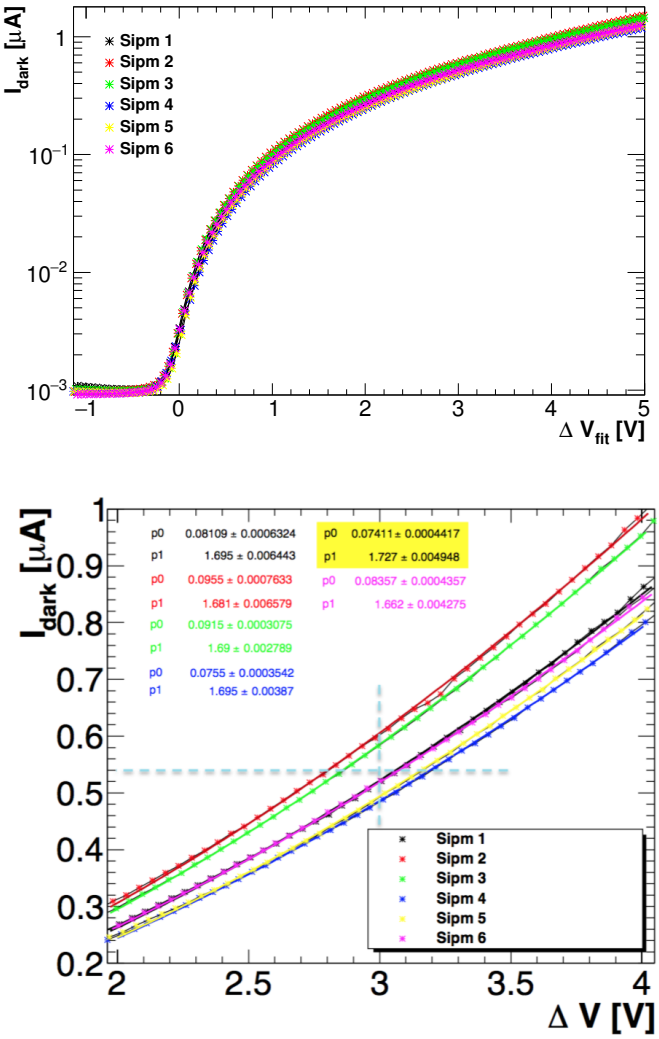

Figure 7.8: *Upper: dark current as a function of the overvoltage. Lower: zoom around the operation region.*

The function used to fit the data is $I_{dark} = p_0(\Delta V^{p_1})$, where p_0 is the value of the current when the bias is $\sim V_{br}$ and p_1 corresponds to the exponential value n. Two systematic differences with respect to Hamamatsu determination have been noticed: the first is the presence of an offset in V_{br} of $\delta V_{br} \sim 300$ mV for four of the SiPMs and a subset of two SiPMs with a δV of $\delta V_{br} \sim 150$mV; the second difference concern the exponential value: as said before we expected from [39] that $n > 2$ but from

the fit we obtain $n \sim 1.7$. This effect can be explained considering that for the new generation of SiPMs the dark rate results reduced due to the introduction of trenches, which separate the SiPM cell reducing the crosstalk. In the region near the operation voltage, defined as $V_{op} = V_{br} + 3$ V following the vendor specifications, we observe (see Table 7.2) that variation of dark current are in within ±15%. From the dashed line we can extrapolate that the average dark current at operation voltages is $I_{op} \sim 0.54\mu$A.

SiPM number	$V_{br}^{Hamamatsu}$[V]	V_{br}^{Fit}[V]	δV_{br}[mV]	n
SiPM 1	52.08	52.44	+320	1.69
SiPM 2	52.14	52.51	+370	1.68
SiPM 3	52.08	52.41	+330	1.69
SiPM 4	52.29	52.54	+250	1.69
SiPM 5	52.02	52.18	+160	1.73
SiPM 6	52.32	52.49	+170	1.66

Table 7.2: *Value of breakdown Voltage from the fit and datasheet.*

7.3.2 Gain determination

The second step for the SiPM characterization is the determination of the gain, which is measured with the following setup:

- A black box containing the experimental system (SiPM and amplifier)
- A Polaroid filter which allows to change gradually the beam light intensity.
- A blue led (λ = 425 nm) driven by a fast pulser illuminating the SiPM surface. Its distance from the photodetector is such that the number of photons reaching the SiPM is extremely small. Since the light produced is small, the distribution of the photons follow a poissonian law. If we were able to distinguish the photon peaks, we could determine the SiPM gain.

The signals generated by the SiPM are amplified by a factor ~ 300 and are acquired by a CAEN DT5751 digitizer at 10^9 samples per second (1Gsps). The experimental set-up used is show in Figure 7.9. In the upper side of Figure 7.10 the charge spectrum of an Hamamatsu SiPM for a fixed position of the polaroid filter is shown. The bias voltage applied is the one expected from Hamamatsu.

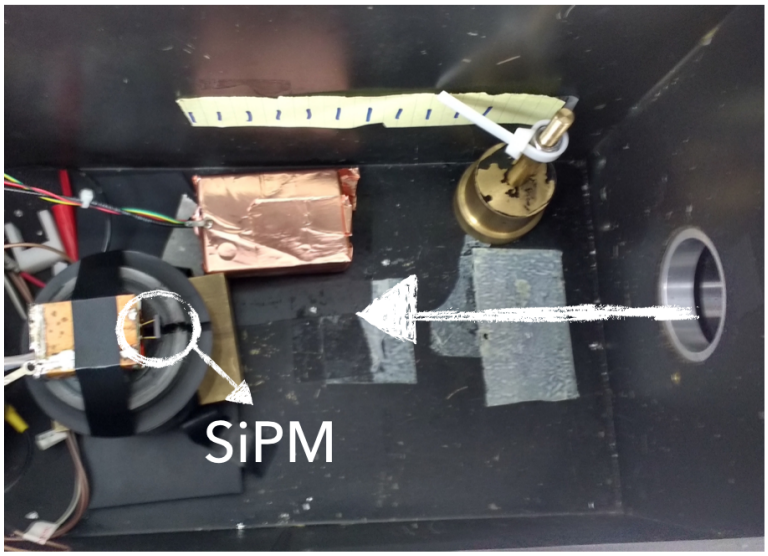

Figure 7.9: *Experimental set up.*

This spectrum is characterized by a very good separation between peaks, which grants an excellent resolving power for photon counting. The estimated gain from Hamamatsu at 25°C and at operation voltage is $G \sim 1.7 \times 10^6$.
In order to evaluate the device gain the following expression is used:

$$Q_n = G_{amp} \times G_{SiPM} \times N_{pe} \times e \;\Rightarrow\; G_{SiPM} = \frac{\Delta Q}{G_{amp} \times e} \tag{7.4}$$

Where Q_n is the charge corresponding to n photons, G_{amp} and G_{SiPM} are respectively the amplifier and SiPM gain, N_{pe} is the number of photoelectrons and e is the electron charge.
In Eq. 7.4 the value ΔQ is defined as the difference between the mean value of the charge of two adjacent peak, so that the number of photoelectrons $N_{p.e.} = 1$. The spectrum is fitted with a sum of gaussians and a continuous polynomial background:

$$Q_{fit} = \sum_i G_i(\mu_i, \sigma_i) + \mathrm{Pol}X \tag{7.5}$$

where $\mu_i = n_i Q_i$ and σ_i is the fixed resolution.
A fit example is reported in Figure 7.10 (bottom). While testing different SiPM we always obtained $G \sim 10^6$ as shown in Tab. 7.3. Using the same experimental set-up and working in the same conditions we have also evaluated the gain dependency on the applied bias. We chose a range of $\sim \pm 1$ V around the operation voltage and determine the gain with steps of 0.25 V. An example of one SiPM is shown in Figure 7.11. Starting from the experimental data we obtain that:

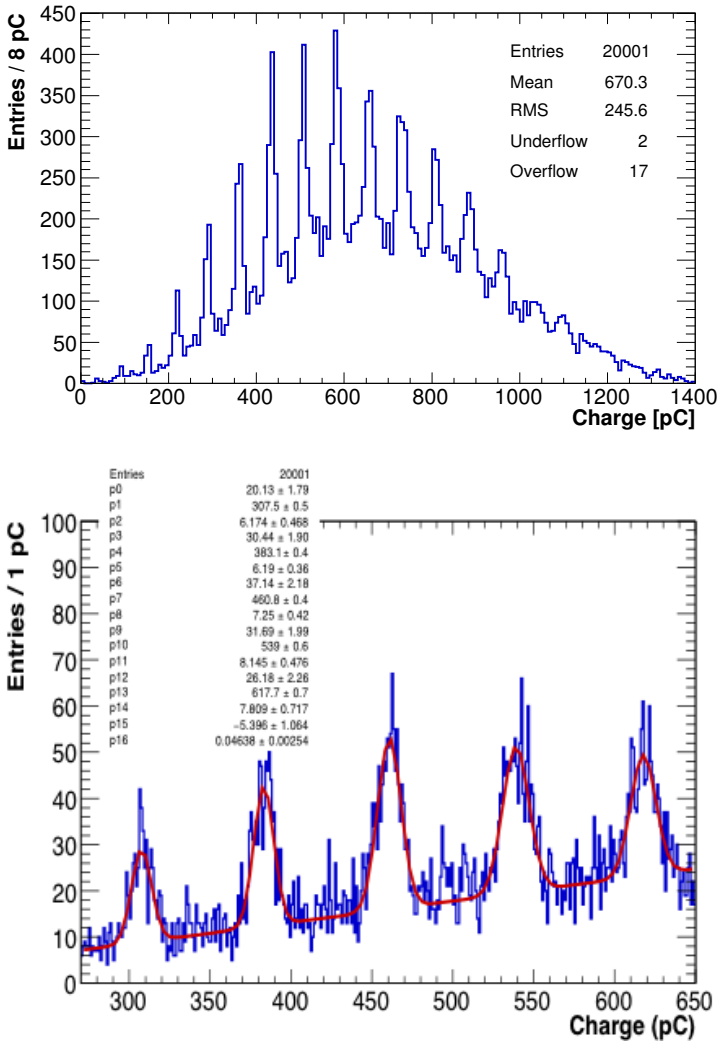

Figure 7.10: *Top: charge spectrum of a SiPM illuminated by a blue LED. Bottom: zoom in the central region and fit of the charge distribution.*

SiPM number	Gain
SiPM 1	1.5×10^6
SiPM 2	1.53×10^6
SiPM 3	1.47×10^6
SiPM 4	1.52×10^6
SiPM 5	1.66×10^6
SiPM 6	1.61×10^6

Table 7.3: *Value of the SiPM gain.*

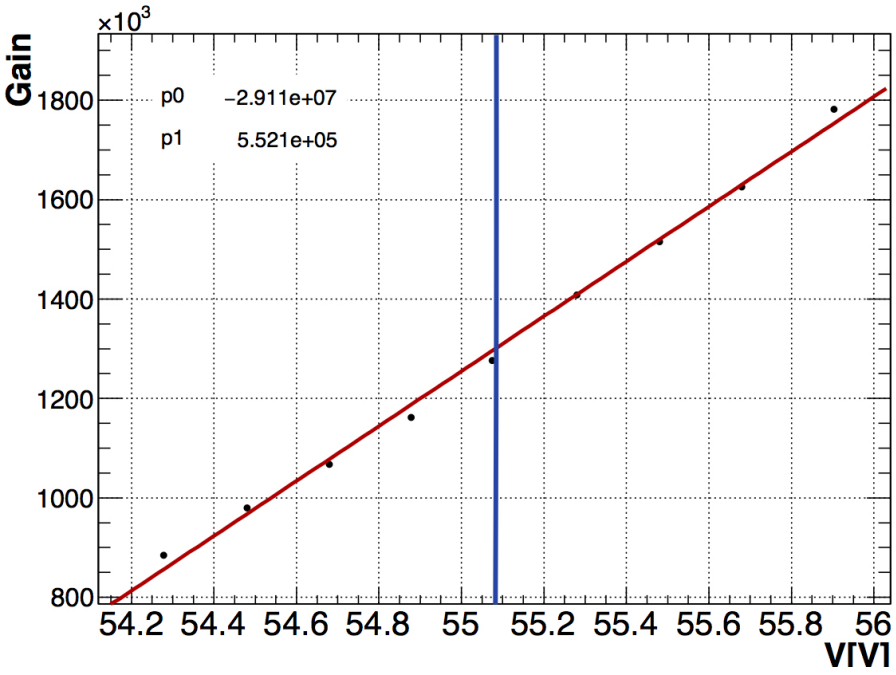

Figure 7.11: *Gain dependency on the on the applied voltage. The red line represent the operation voltage.*

$$\frac{\delta G/G}{\delta V} \sim \frac{5.521 \times 10^5/V}{1.3 \times 10^6} \sim 40\%/V \tag{7.6}$$

It is possible now to evaluate the gain spread of the different SiPM at V_{op}. In Figure 7.12 gain variation as a function of the overvoltage $\Delta V = V_{op}^{ham} - V_{bias}$ is reported. It results that at operation voltage ($\Delta V = 0$) the maximum gain obtained is $G = 1.69 \times 10^6$ and minimum value is $G = 1.48 \times 10^6$. Using the definitions:

$$\Delta G = \frac{(G_{max} - G_{min})}{G_{mean}} \quad \text{and} \quad \delta G = \frac{(G_{max} - G_{min})/\sqrt{12}}{G_{mean}} \tag{7.7}$$

where $G_{mean} = (G_{max} + G_{min})/2$ and δG is the uncertainty associated to ΔG (supposing a uniform distribution for the gain spread), we obtain that $\Delta G = 0.133 \pm 0.038$. Alternatively, instead of the value provided by the vendor Hamamatsu, it is possible to use our estimations for the V_{op} (obtained with the fit described above) to evaluate the gain variations, as shown in Figure 7.13. In this case we obtain $G_{max} = 1.74 \times 10^6$ and $G_{min} = 1.68 \times 10^6$ and a value of gain variation of $\Delta G = 0.035 \pm 0.010$. Comparing this value with the one obtained using the values of V_{op} given by Hamamatsu ($\Delta G = 0.133 \pm 0.038$) it results that the performed measurements returns more accurate and precise values of V_{op}. The straight red line, that is an average value of the gain near V_{op} ($G_{mean} = 1.62 \times 10^6$), allows us the evaluate the spread in V_{op}: from

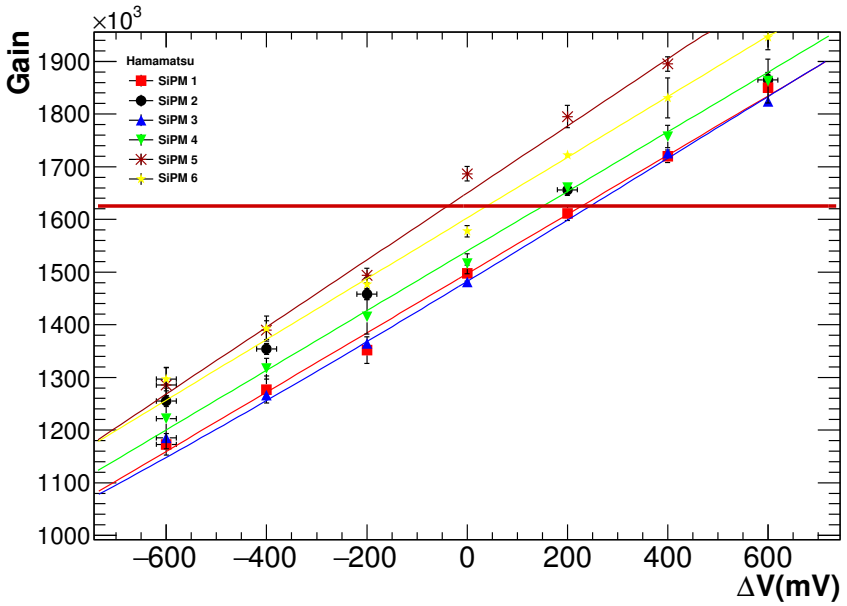

Figure 7.12: *Gain spread of the six Hamamatsu SiPM tested as a function of the over-voltage* $\Delta V = V_{op}^{ham} - V_{bias}$.

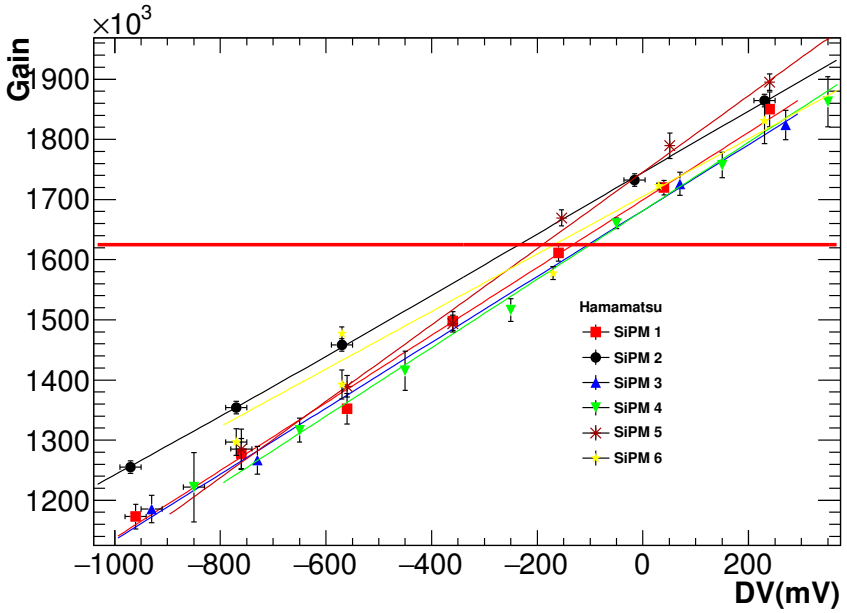

Figure 7.13: *Gain spread of the six Hamamatsu SiPM tested as a function of the over-voltage* $\Delta V = V_{op}^{fit} - V_{bias}$.

the Figure 7.12 we obtained a spread of $\delta V \sim 292$ mV. Considering an operation point of ~ 55 V we obtain that $dV_{op}/V_{op} \sim 5.6‰$, while from Figure 7.13 we have $\delta V \sim 140$ mV and $dV_{op}/V_{op} \sim 2.5‰$ that is is compatible the requirement fixed at

$\sim 3‰$.

7.4 Radiation hardness of SiPM

The Mu2e calorimeter must operate and survive in a high radiation environment. Simulation studies estimated that SiPMs have to withstand at 1 MeV equivalent neutron fluency of 3×10^{11} n/cm^2 and a to Total Ionizing Dose (TID) of 20 krad of photons in three years of running [40]. These values already assume a factor of 3 safety and are calculated in the region where the ionization is maximal, i.e. the innermost ring. For this reason we have tested SiPMs to measure the variation of the leakage current and the charge response to an ultraviolet led. During the first irradiation campaign in 2015, different models of Silicon Photomultipliers (SiPM) have been tested: two SiPMs from Hamamatsu and a SiPM from FBK [41]. The two Hamamatsu SiPMs had equal layout but different protection material: one SiPM had a cover with a silicon protection layer (SPL) while the other one with a Micro-Film (MF). The FBK SiPM was instead monolithic. SPL and MF are 12×12 mm^2 detectors made of an array of 16 3×3 mm^2 cells, while the SiPM from FBK is made of a single 6×6 mm^2 cell.
The SPL SiPM was irradiated with photons at CALLIOPE facility (ENEA, Casaccia) up to a total dose of ~ 20 krad in 3 days of exposition. The dose effect on SiPM performances resulted to be negligible both in term of leakage current and signal amplitude at this level of irradiation.
On the other side, the three different SiPMs were irradiated with neutrons at FNG facility (ENEA, Frascati) and placed 7 cm away from the source. Since changes in temperature affect the SiPM response the temperature of experimental hall was maintained stable between 23°C and 25°C. SiPMs were irradiated for ~ 4 hours with 14 MeV neutrons up to 2.2×10^{11} n/cm^2, which corresponds to a 1 MeV neutron fluence equal to 2.2 times the experimental lifetime. The neutron flux caused a strong decrease of the signal peak and gain and a large increase of the leakage current. Irradiation test with neutrons on a SiPM of the same type of those used in the previous Sections have been also performed at EPOS neutron source (HZDR, Dresden) in April 2016. As shown in Figure 7.14 the active area of the SiPM was positioned parallel to the incoming neutron flux. It was biased with the nominal operation voltage that is 54.9 V.
To understand the difference in the irradiation results, we have simulated different positions of the SiPM with respect to the neutron flux and estimated that the irradiation results are practically independent from the particular SiPM orientation.

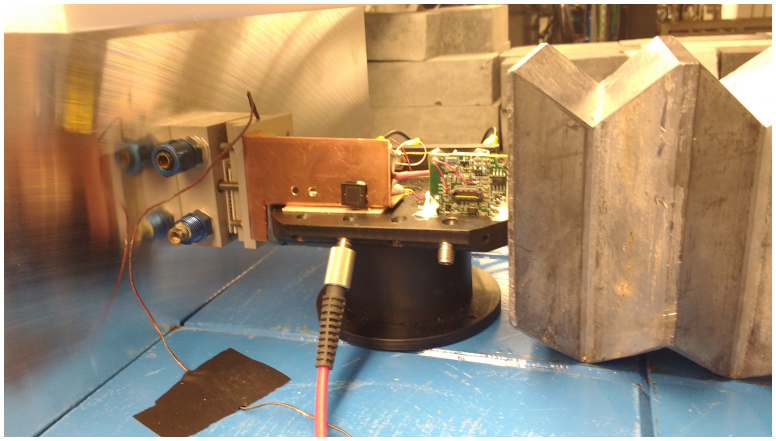

Figure 7.14: *Experimental set up used at HZDR center.*

Indeed, a small difference is observed in the effective neutron fluency between the SiPM running in horizontal or vertical configurations as shown in Figure 7.15. Average results for the 1 MeV equivalent fluency at are: $(1.365 \times 10^7 \pm 9.6\%)$ n/cm^2/s for the vertical configuration and for the horizontal one $(1.682 \times 10^7 \pm 4.9\%)$ n/cm^2/s.

The particular position in the experimental hall has been chosen to minimize the

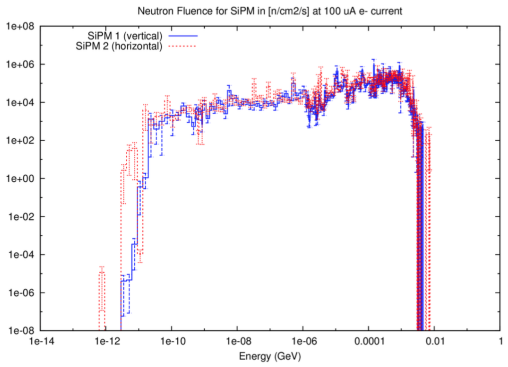

Figure 7.15: *Neutrons fluence for horizontal (red and dashed) and vertical (blue) configuration as obtained in simulation.*

number of incoming γ, as shown in Figure 7.16, where SiPM position is underlined with a white box. To maintain the SiPM temperature as stable as possible, the irradiated SiPM has been connected with a Peltier cell, with the hot side in a cooling system. The SiPM temperature has been monitored using a PT1000.To control and monitor the Hamamatsu devices, a pulsed UV-led and two splitted optical fibers have been used to illumunate the SiPM and a PMT positioned near the neutron source.
We acquired the signal response to the led pulse and the leakage current of the SiPM using a Keithley 2001 Multimeter while the SiPM amplitude is evaluated from the

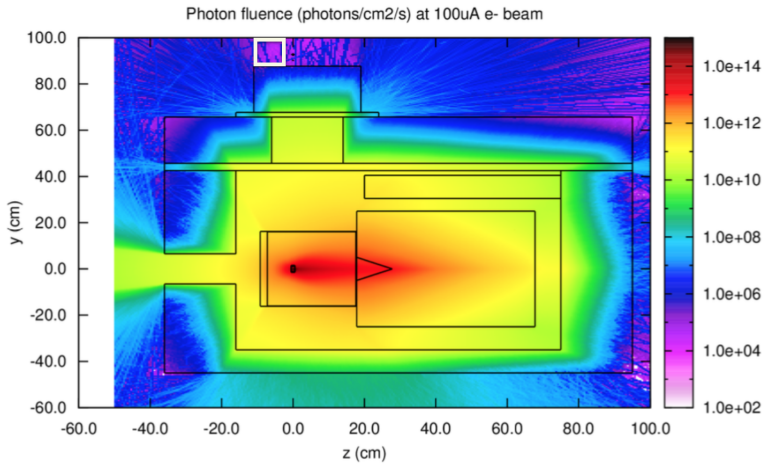

Figure 7.16: *γ fluence inside the experimental area.*

scope. The PMT response has been used as reference signal to obtain a precise measurement of the light input.
The total 1 MeV neutron fluence absorbed by the SiPM in five days was larger than 4×10^{11} n/cm^2, that is three times the flux expected in the hottest region in 3 years of running.

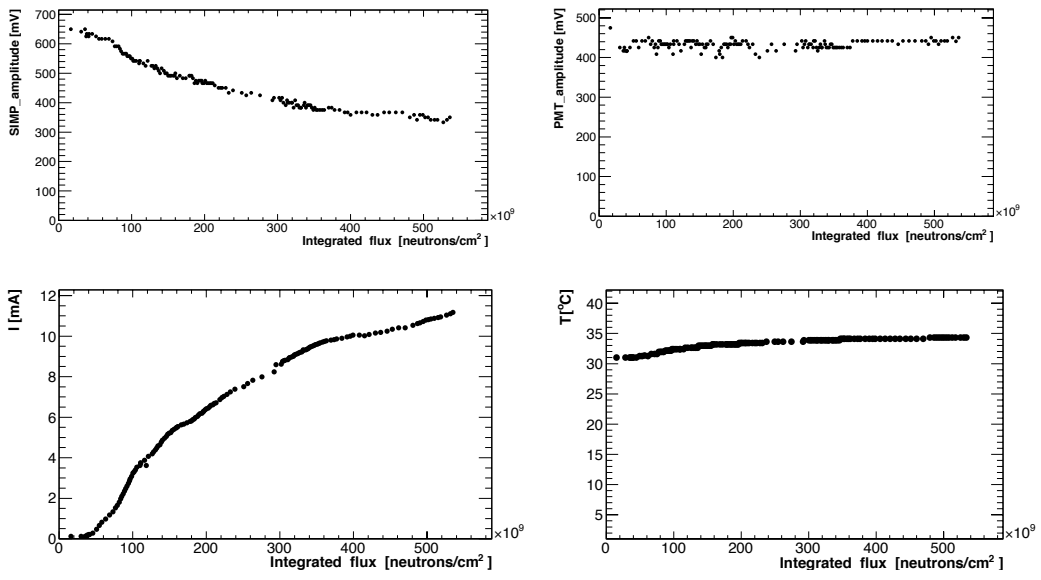

Figure 7.17: *Top: variation of SiPM (left) and (PMT) signal amplitude during the irradiation test. Bottom: SiPM leakeage current (left) and SiPM temperature (right) as a function of the integrated flux.*

During the irradiation temperature increases from 31° C to 34.25°
In Figure 7.17 irradiation results are reported as a function of the integrated flux.
The SiPM signal peak decreased from ∼650 mV to ∼400 mV, this behavior is in part due to the temperature variation. A rising behavior of the SiPM leakage current is clearly visible: it increased from 60μA up to 12 mA.
At the end of this test, we have waited for the SiPM annealing for one month, then we measured the I_{dark}-V curve of the irradiated SiPM and compare it with the other curves previously shown in Section 7.3. The result is reported in Figure 7.18 as a function of the overvoltage $\Delta V = V - V_{br}$.
In the region around the breakdown voltage the dark current of the irradiated SiPM is 2 order of magnitude greater than the one of the non-irradiated one. The plateau region is due to the pico-ammeter saturation.

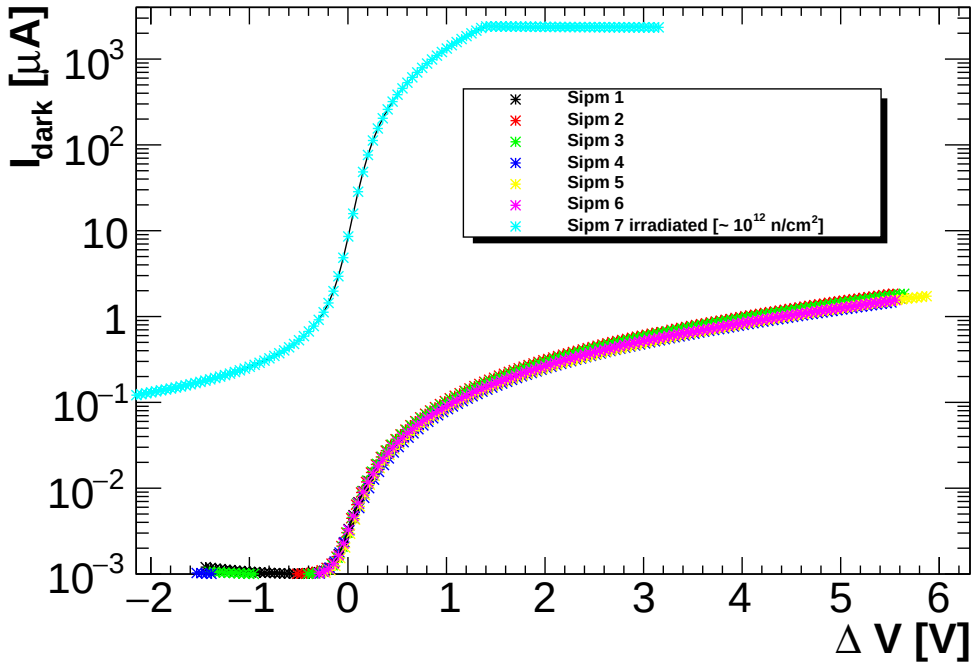

Figure 7.18: *Comparison between irradiated and unirradiated SiPM I_{dark}-V curves.*

7.5 Temperature dependency

In order to learn how much we should cool down our sensor after irradiation, we have investigate the SiPMs properties as a function of its temperature. We did this test both with not irradiated and irradiated SiPMs.

To avoid to reach the dew point we have performed these tests in a vaccum chamber at $\sim 10^{-4}$ mbar. The SiPM under study was cooled by means of a cascade of two peltier cells: the bigger one is in thermal contact with the bottom plate of the chamber , thus acting as external heat sink, the smallest one was in contact with the SiPM surface and acted as a chiller. The SiPM temperature was monitored by a PT1000 sensor. A UV- LED was illuminating directly the sample inside the chamber.
The experimental set up used is shown in Figure 7.19.
To study the dependence of the V_{op} on temperature, the SiPM was illuminated with

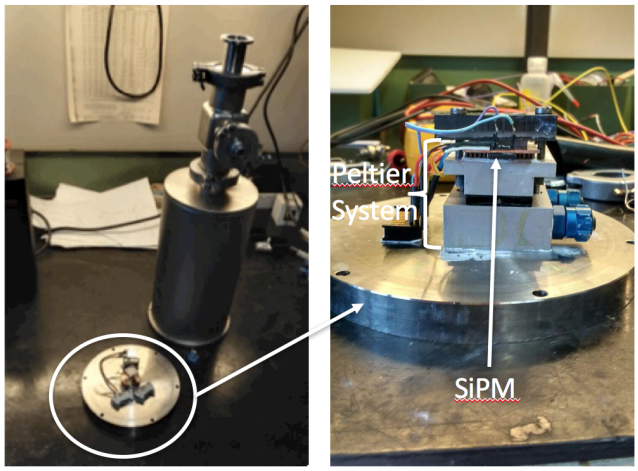

Figure 7.19: *Experimental set up used for the temperature dependency studies.*

a LED and the peak of the signal pulse height recorded with a digital scope. When varying the temperature, we set the operation voltage by keeping constant the signal amplitude. In Figure 7.20 the dependence of V_{op} as function of the temperature is reported: V_{op} decreases for decreasing temperature as expected. This is due to the increase of ionization rates at low T [45] [46].
The dependency is linear for the not irradiated SiPM so that we can quantify, from a linear fit, the drop in the V_{op} coefficient as (52.28 ± 0.4) mV/^{o}C.
Concerning the irradiated one, there is a change of slope at ~ 13°C. From a linear fit of the irradiated SiPM curve it results that between -13 and 13°C the slope value is (62.89 ± 1.25) mV/^{o}C. and between 13 and 29°C the slope is (161.8 ± 10.4) mV/^{o}C. Concerning the not irradiated SiPM changes in slope are not observed and its value is (52.3 ± 0.4) mV/^{o}C. A similar behavior for the two SiPM is observed at low temperature, while it changes for the irradiated one with the increase of the temperature. Moreover, using a pico-ammeter we acquired the dark current at operation voltage for the two SiPMs under study and we plot it as a function of the temperature. Results are in Figure 7.21. The shape of the two distributions are similar but the dark current

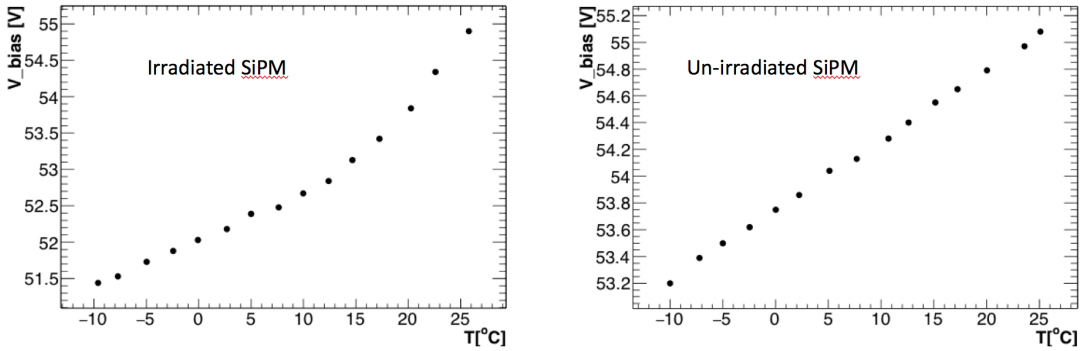

Figure 7.20: *Dependency of the breakdown voltage on device temperature for a irradiated and non irradiated SiPM.*

for the irradiated SiPM is larger of at least three orders of magnitude. From these

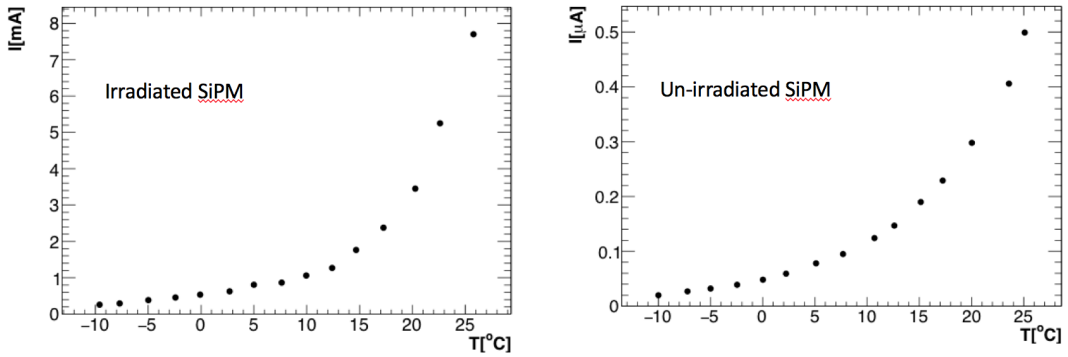

Figure 7.21: *Dependency of dark current on device temperature for a irradiated and un-irradiated SiPM.*

plots, we have learnt that to remain inside our front-end electronics requirements, i.e. I_{supply}<2 mA/channel, we need to run at T< 5^{o}C.
Indeed we can calculate this from Figure 7.21(left): at 0 ^{o}C one 6×6 mm^2 SiPM will reach $\sim$ 1 mA, 3 SiPM in series will have the same running current. In the parallel of the two series will flow a current I< 2 mA respecting the supply requirement.
We are designing our front end electronics and sensor cooling system to keep the SIPM to a running temperature between -10°C and 0°C.

7.6 Study of charge resolution for SiPM in series

7.6.1 Series made of three un-irradiated SiPMs

As explained in Section 7.1 the Mu2e SiPM is a 2x3 array of individual 6x6 mm^2 monolithic UV extended SiPMs. Each series has an independent bias voltage while the anodic signals of the two series will be sum together.
The operation voltage applied to each siPM in the series is determined by the common I_{dark} and the single I-V curve.
To prove that there is no effect on the resolution due to a non perfect determination of the operation voltage of the SiPM, we have carried out direct test on the charge resolution. Our first test compared the charge resolution observed in a SiPM series with respect to the one of a single SiPM. Both the series and the single SiPM are illuminated uniformly with a LED. SiPMs were mounted on a PCB support, shown in Figure 7.22 and then inserted inside a black box and illuminated by an UV Led through a polaroid filter. In Figure 7.23 the distributions of resolution for one SiPM and for a

Figure 7.22: *Support used in the experimental set up.*

series of three SiPMs are shown as a function of the charge peak. The distributions have been fitted using the following formula:

$$\sigma_Q/Q = \sqrt{(Fano/N_{pe}) + \sigma_N^2} = \sqrt{\frac{p_0}{Q\left(\frac{p_1}{Q_{max}}\right)} + p2} \tag{7.8}$$

where p_0 represent the Fano factor, p_1 is the number of photoelectrons $N_{p.e.}$ measured at Q_{max}, p_2 describes the noise factor and Q_{max} = 600 pC.

From the fit parameter we obtain that the Fano factor (called also excess noise) is compatible with one and the noise is negligible. The number of photoelectrons estimated from the fit to the resolution for the SiPM in series ($N_{pe_{series}}$ = 5476) is three

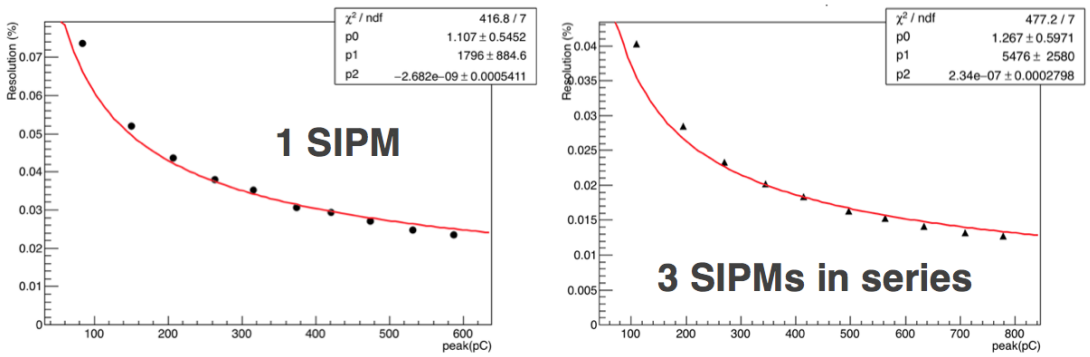

Figure 7.23: *Charge resolution as a function of the amplitude of the charge distribution.*

times larger than that obtained for a single SiPM ($N_{pe_{1SiPM}}$ = 1796). This demonstrate that the resolution is dominated by Poisson fluctuation of the collected light and no other effects contribute

7.6.2 Series made of two non irradiated SiPMs and an irradiated one

In this section we quantify the effect on resolution related to the irradiation-induced increase of SiPM leakage current. Let us consider the extreme case where only one of the three SiPM has been irradiated increasing its leakage current of a factor 2000 with respect to the not irradiated ones. Given that the chosen bias has to be the one corresponding to $I_{dark} \sim 0.5\mu$A, the irradiate SiPM will work with a (V_{op} - V_{br}) ~ 0 V (see Figure 7.18), so that its response will be negligible. This will not effect the behavior of the other two SiPMs.
To prove this, the response of the series connection of three SiPMs to a blue laser was studied in the two configurations sketched in Figure 7.24:

(a) Three not irradiated SiPMs,

(b) Two not irradiated SiPMs and the one irradiated at EPOS

To obtain a uniform illumination of the series it would have been better to align the three SiPMs of case (b) on the same row, as we did for the not irradiated SiPM. However, we did check that the illumination was uniform in this position. We operated the arrays at constant current by fixing the operational point at 0.54μA. This working-point corresponded to $\Delta V \sim 0$ V for the irradiated SiPM, so that we biased the series (a) to V_{op} = 166.4V and series (b) to V_{op} = 162.7 V.
In Figure 7.25 the charge distributions of the two series are reported. Taking into

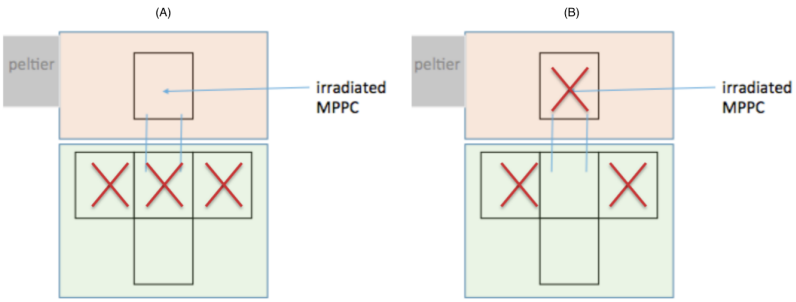

Figure 7.24: *Different configurations used for testing un-irradiated (A) series and irradiated (B) series.*

account the ratio between the peaks of the charge distribution between SiPMs series (b) and series (a), we obtain that:

$$Q_{w\ irr}/Q_{w/o\ irr} = 0.66 = 2/3 \tag{7.9}$$

This result is compatible with the hypothesis $\Delta V \sim 0$ V for the irradiated SiPM. Using

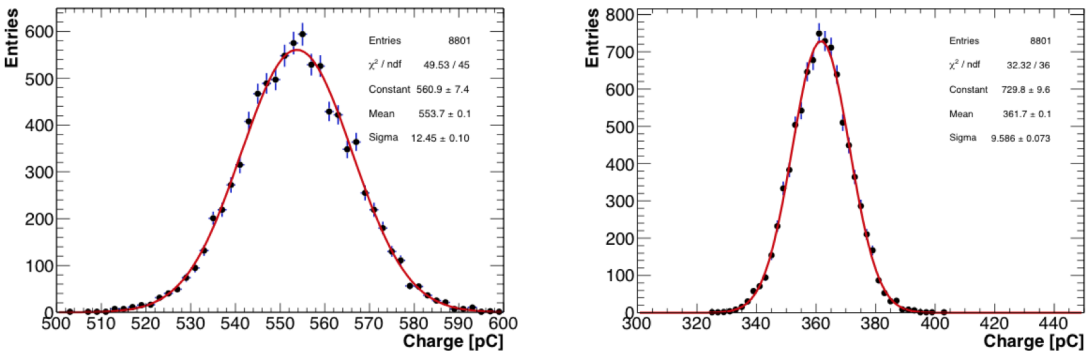

Figure 7.25: *Left: charge distribution for the unirradiated series. Right: charge distribution for the series made of an irradiated SiPM and two non irradiated.*

the same experimental set up we have measured the variation of the mean value of charge distributions as a function of the polaroid intensity for the two SiPM series. Results are reported in Figure 7.26.

In both cases the total charge decreases as far as the polaroid filter closes. The charge of the series, that contains the irradiated SiPM is smaller than the one of series (a). The charge resolution as a function of charge peak is also reported, resolution of the series with the irradiated SiPM is worse than the other one. The fit function used is the one reported in Eq. 7.8. Differently from Figure 7.23 right, in both configurations tested an higher electronic noise is observed.

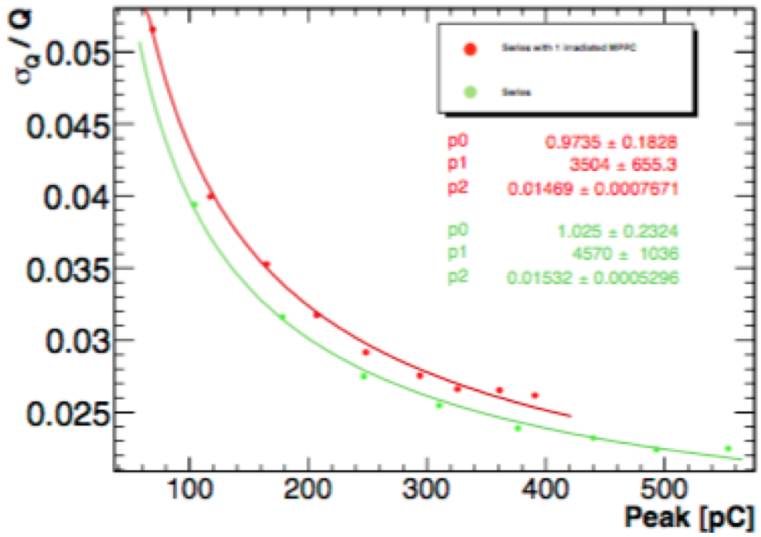

Figure 7.26: *Charge resolution as a function of charge peak.*

7.6.3 Simulation

After having tested the extreme case in Subsec. 7.6.2, we have estimated the variation of the resolution as a function of a possible gain variation in the single cell of a series with 3 SiPMs.

We start assuming that the gains of the three SiPM are equal $G_1 = G_2 = G_3 = G_0$, the illumination and the PDE are similar and that the number of photoelectrons N_{pe} emitted is equal to N_0 for each SiPM. The response of the series in this case is $Q = 3 \times N_0 \times G_0$.

We then consider the charge response of the series for a variation of the gain in the single cell as follows:

$$\frac{Q_{series}}{e} = G_1 N_0 + G_2 N_0 + G_3 N_0 \quad \text{where } G_i = G_0 + \Delta G_i \tag{7.10}$$

For this exercise we assume that the number of photoelectrons is equal for all SiPMs, i.e. the PDE variation is smaller that gain one. In this case we obtain

$$\frac{Q_{series}}{e} = N_0 G_1 + N_0 G_2 + N_0 G_3 = 3N_0 \left[G_0 + \frac{1}{3}(\Delta G_1 + \Delta G_2 + \Delta G_3 \right] = 3N_0 G' \tag{7.11}$$

To understand this effect, we build a toy Monte Carlo: we fixed the gain of one of thee SiPM $G_1 = G_0$ and varyied the gain of the other two $G_i = G_0 \pm \Delta G$. In order to give a reasonable estimate of the number of photoelectrons collected by one SiPM at at ~ 100 MeV the following relation is used starting from the known value of Light Yield (see 7.8) a of 2" PMT:

$$\frac{1}{6}\left(\frac{NPE}{MeV}\right)_{Sipm} = PDE_{ratio} \times Area_{Ratio} \times \left(\frac{NPE}{MeV}\right)_{PMT} \sim 4.5 pe/MeV, \tag{7.12}$$

where $PDE_{ratio} = PDE_{SiPM}/PDE_{PMT} = 35\%/25\% = 1.4$,
$Area_{Ratio} = A_{6SiPM}/A_{PMT} = 216mm^2/1156mm^2 = 0.19$ and $\frac{NPE}{MeV}_{PMT} = 103$ p.e./Mev.
We divided the number of photoelectron by a factor of 6 because we are interested in knowing the value for a single cell in the series. For the number of photoelectrons emitted by three different SiPMs we extracted random values, poissonian distributed for each SiPM ($\mu = N_{p.e}$ and $\sigma = \sqrt{N_{p.e.}}$). The total charge can be now calculated as expressed in Eq. 7.10. An example of the obtained distribution is shown in Figure 7.27. We then consider an interval of ΔG between $[-40\%, 40\%]G_0$ and evaluate the total

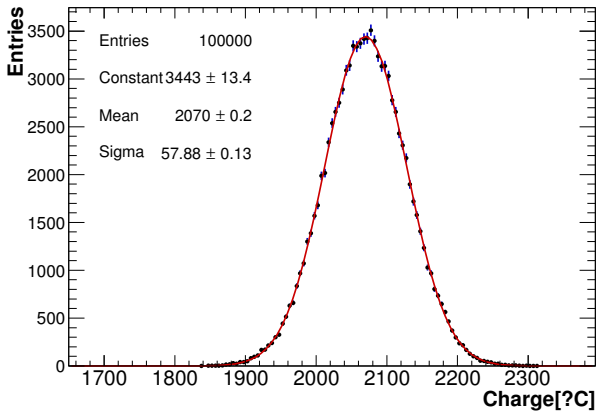

Figure 7.27: *Distribution of the simulated charge of a 3 SiPMs series.*

charge distribution in discrete steps of δG_0. For each case, with a gaussian fit we have extracted the mean value and the σ of the charge distribution. Results of the MC simulation are reported in Figure 7.28.

The resolution is reported as σ/Q, these two parameter are extracted from a gaus-

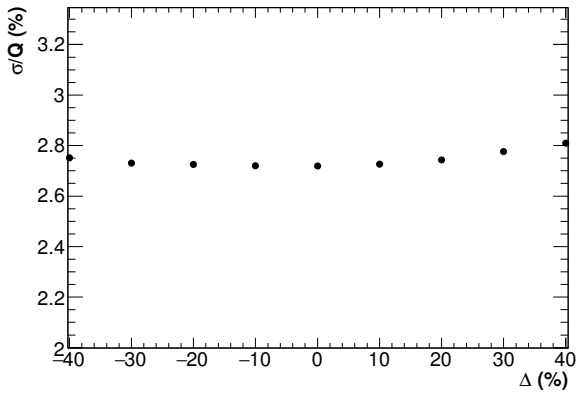

Figure 7.28: *Charge resolution as a function of the* ΔG.

sian fit of the charge distribution. This results clarifies that even large variations in the gain of a series of three SiPMs does not affect the resolution.

7.7 The SiPM Mean Time to Failure (MTTF)

Mean Time To Failure, MTTF, is the mean time to the first failure under specified experimental conditions [43]. It is one way to evaluate the reliability of pieces of hardware or other technology.
In this section we will determine the MTTF needs for the Mu2e SiPM experiment and explain the methods for its experimental determination.

7.7.1 Estimate of MTTF requirements

We developed a simulation to estimate the expected number of SIPMs that will die in a year of run for a given sensor MTTF. We assume to be in the flat region of the lifetime "bath-tube" distribution, i.e. that the SiPM have a constant dead rate. The number of SiPMs considered in this simulation is 1400, that is $\sim$ the number of SiPMs used in the Mu2e experiment.The value of MTTF has been initially fixed to be $MTTF = 10^6$ hours, giving origin to an exponential decay distribution which describes the SiPM probability of survival and we made 1000 fake experiment. For each of these trials the number of deads was obtained extracting 1400 times a value from the exponential distribution. If the value extracted was smaller that a time-limit fixed to 3 years of run we declared "the SiPM dead". The same procedure is repeated considering a time limit of one year. The results are reported in Figure 7.29.

Then we considered the readout of a single crystal is made of two independent components called (a) and (b) (the two 2×3-SiPM arrays), to understand how often the two sides of a cell die simultaneously. This is due to our requirement to have enough light also with one or half of a SiPM. We fixed the number of cell to be $N_a = N_b = 1400$. From the plots in Figure 7.30 it is clear that the probability to have one cell with both SiPMs dead is very small increasing substantially our reliability during running with respect to the case of one SiPM per crystal only. We have also repeated the simulation considering the SiPMs array made of 4 separate components (the Mu2e SiPM arrays should be made of the parallel of two independent 3 SiPMs series) to study how this increase on redundancy could influences MTTF. Results considering a MTTF of 10^6 hours and a time limit of one and three years of runs resulted in no cases where all the four components are dead simultaneously on the same cell,
From this simulation, we derived the MTTF needed to obtain a 99% (95%) probability

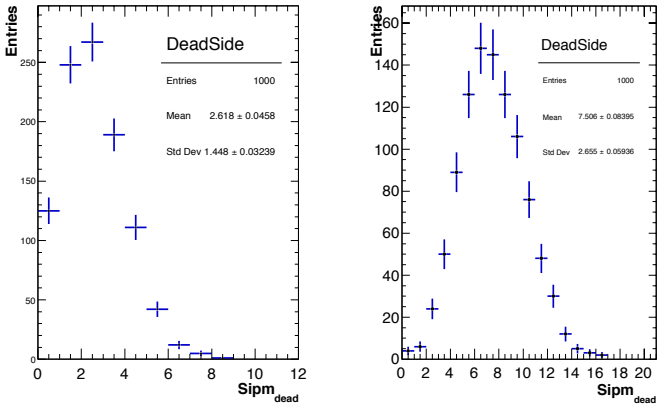

Figure 7.29: *Distribution of the dead SiPM considering a time limit of 1 year of run (left) and 3 year of run (right) and a MTTF* 10^6 *hours.*

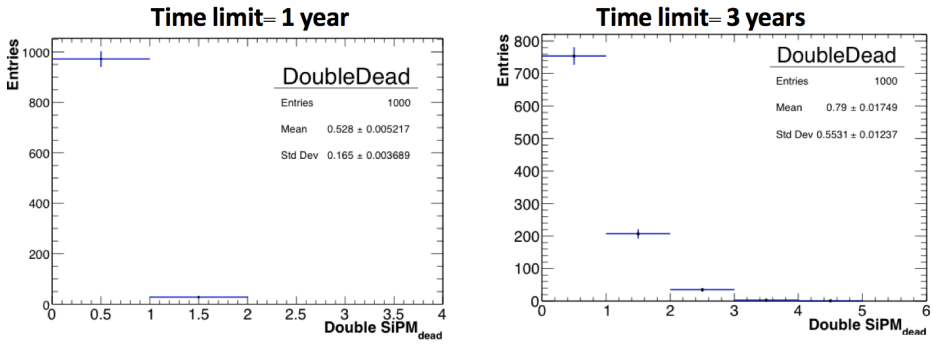

Figure 7.30: *Distribution of the dead SiPM considering a time limit of 1 year (left) and 3 years(right) of run and a MTTF of* 10^6 *hours.*

of survival with at maximum one dead element in three years run, this has been done repeating and varying the MTTF value and considering a time limit of 3 years run. Distributions are reported in Figure 7.31 and Figure 7.32 for two specific value of MTTF. We obtained that we need a MTTF of 0.27×10^6 (0.185×10^6) hours to meet respectively the request on 99% (95%) probability of survival.

7.7.2 Determination of MTTF value

Existing measurement from literature indicates an MTTF of 4×10^6 hours for 3x3 mm^2 MPPCs when running at 25° C. Since the SiPM in the Mu2e experiment will work at 0° C, we gain a reliability factor of 11 (see Equation 7.13) so that this trans-

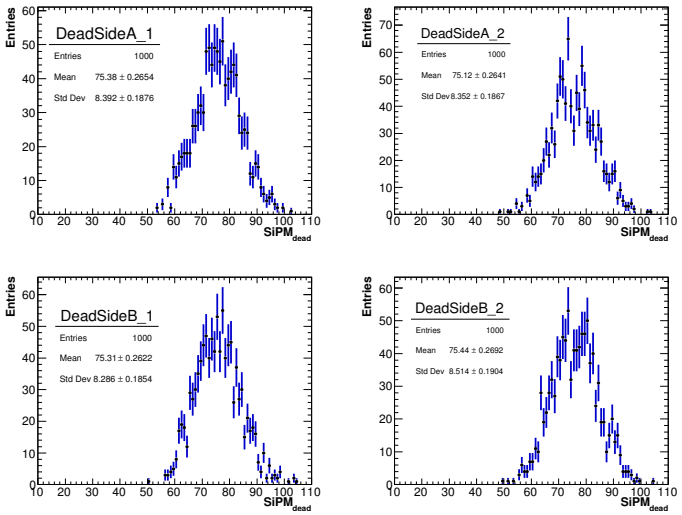

Figure 7.31: *Distribution of the number of dead SiPM cells considering a time limit of three years of run and a MTTF of* 0.27×10^6 *hours, when requiring 4 independent biased SiPM cells.*

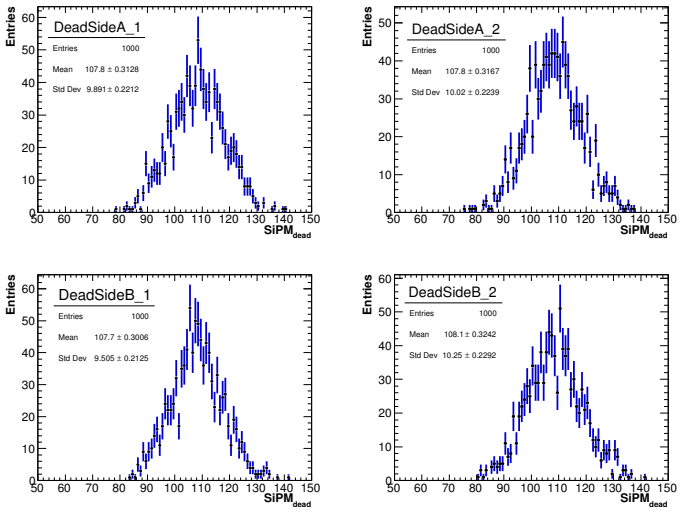

Figure 7.32: *Distribution of the number of dead SiPM cells considering a time limit of three years of run and a MTTF of* 0.185×10^6 *hours, when requiring 4 independent biased SiPM cells.*

lates to an MTTF of 44×10^6 hours. Further scalings are necessary because of the different SiPM area (need to decrease MTTF by a factor 4, because the single SiPM makig the Mu2e custom SiPMs are 6×6 instead of 3×3) and different number of SiPMs in a Mu2e array (decrease by a factor 6).
After applying all these corrections the result obtained is MTTF $_{Mu2e}\sim1.8\times10^6$ hours.

We have also performed at LNF a first MTTF determination using four 6×6 mm^2 FBK SiPM [41]. As shown in Figure 7.33, the SiPMs were put in a box maintained at 50° C using Peltier cells and pulsed every 300 s with an UV led. After two months of run-

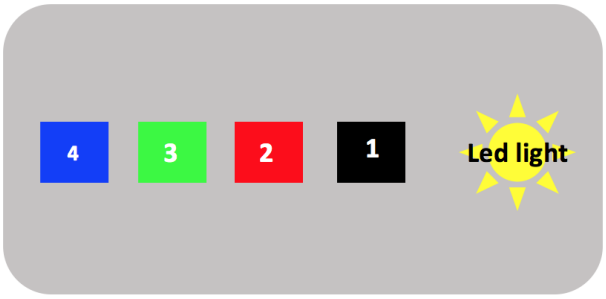

Figure 7.33: *Sketch of the experimental setup used for the MTTF test.*

ning all four SiPMs were still working as shown in Figure 7.34.

Two out four SiPMs do not present any variation in signal amplitude whereas the

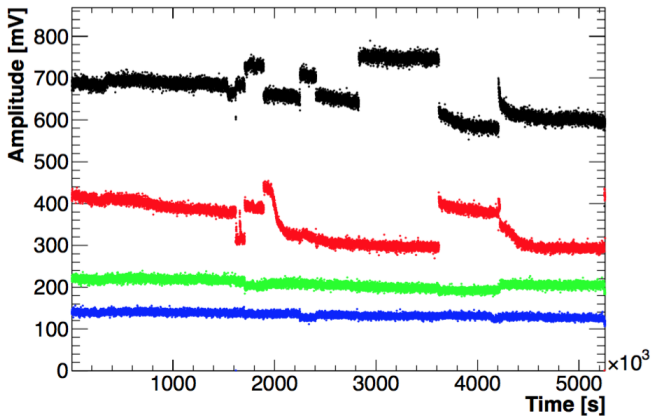

Figure 7.34: *Results of the MTTF performed in LNF for four FBK SiPM.*

signal amplitude of the other two decreased of an order of magnitude. We believe that this is due to a not perfectly stable position of the UV led. At the end of the test all the SiPMs were perfectly working. Assuming no deads in two months for 4 SiPMs corresponds to a measured MTTF of > 0.5 x NSIPM x AF x Nhours, that is $2\times99\times1300$ hours$\rightarrow 0.26\times10^6$ hours.

The term AF=99 is the acceleration factor, obtained from the Arrhenius equation:

$$AF = exp\left[\frac{E_a}{k}\left(\frac{1}{T_{use}} - \frac{1}{T_{stress}}\right)\right] \tag{7.13}$$

where $E_a = 0.7$ eV is the Silicon activation energy, k is the Boltman constant, $T_{use} = 273$°K is the temperature fixed for the Mu2e experiment and $T_{stress} = 323$°K is the temperature fixed during the MTTF test. The acceleration factor is used to derate the failure rate from the thermally accelerated life test conditions to a failure rate indicative of experiment temperature.

7.8 Crystals characterization

In this section the results of tests performed on crystals at LNF and Enea-Frascati are reported. In particular, crystal light output and radiation induced noise (RIN) are addressed.

7.8.1 Light Yield and Response Uniformity

17 crystal from three different vendors (ISMA, SICCAS [47], Optomaterials) have been tested to study the light yield (LY) and longitudinal response uniformity (LRU). A low intensity collimated ^{22}Na source (placed between the crystal and a small tagging system made of a $3 \times 3 \times 10$ mm^3 LYSO crystal readout by a 3×3 mm^2 SiPM irradiated the crystal in few mm^2 emitting a 511 keV electron-positron annihilation photons.
One of the two back-to-back photons is tagged by the LYSO monitor and the other one is used to calibrate the crystal under test, which is readout by a 2" UV extended photomultiplier. It is characterized by a quantum efficiency of $\sim 30\%$ at 310 nm, that is the CsI emission peak.
The experimental setup is shown in Figure 7.35. The data acquisition system is com-

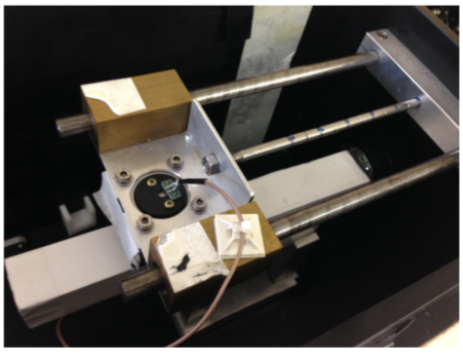

Figure 7.35: *detail of the setup used to test crystals.*

posed by a trigger board, which starts the recording of the events applying a threshold

of 20 mV on the tag discriminated signal, and a CAEN DT5751 digitizer at 10^9 samples per second (1 Gsps), which acquires both tag and test signals.
A longitudinal scan is done irradiating eight points, in 2 cm step, from the readout system. In the scan, the source and the tag are moved together along the axis of the crystal under test with a manual movement. For each position the mean value of the charge distribution is extracted to evaluate the light yield following the expression:

$$\frac{N_{p.e.}}{MeV} = \frac{\mu_{Q1}[pC]}{G_{PMT} \times E_{\gamma}[MeV] \times q_{e^-}[pC]}, \tag{7.14}$$

where $q_{e^-} = 1.6 \times 10^{-19}$ pC is the electron charge, $E_{gamma} = 511$ keV is the energy of the photon and $G_{PMT} = 3.8 \times 10^6$ and μ_{Q_1} is the mean value of the charge distribution. From crystal requirements the longitudinal uniformity (LRU) is defined by the RMS of the Light Yield distribution in the 8 measured points.
Results reported in Figure 7.36 are obtained as a mean value of the 8 measurements along the crystal. Almost all SiPMs from different vendors meet the experimental

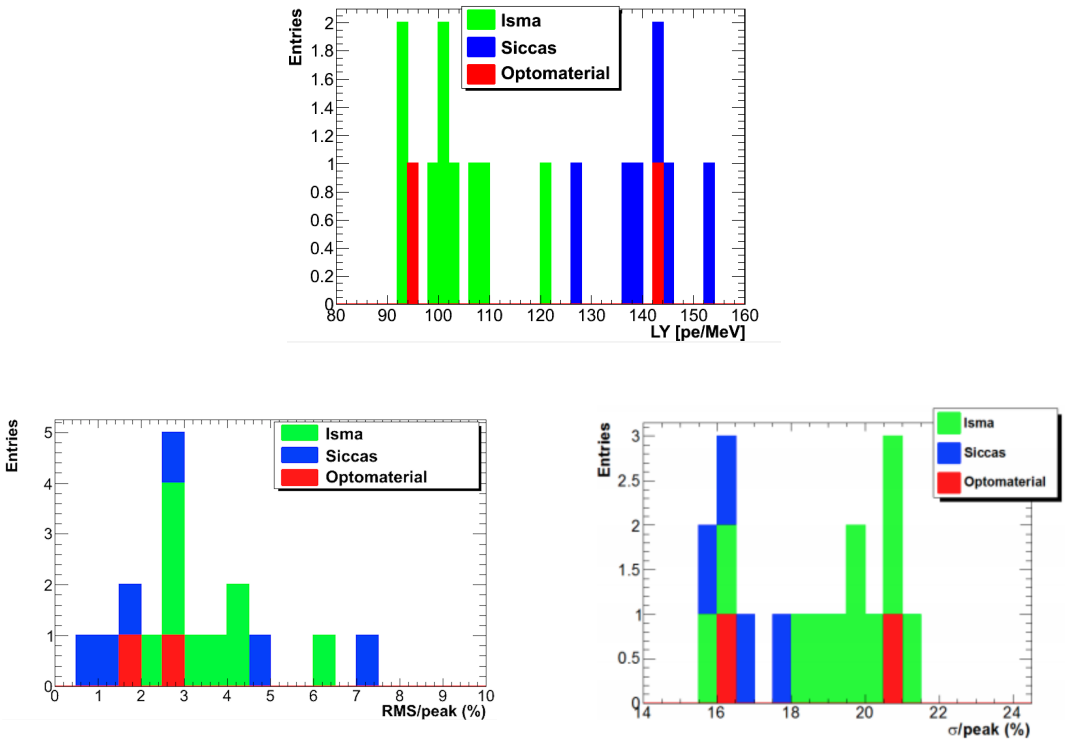

Figure 7.36: *Top: crystal LY distribution from different vendors (Mu2e requirement: LY> 100 p.e/MeV). Bottom Left: LRU distribution (Mu2e requirement LRU < 5%). Bottom right: energy resolution expressed as σ_q/peak (Mu2e requirement $\sigma_E < 20\%$).*

requirements fixed, that is:

- LY > 100 p.e./MeV
- LRU < 5%
- σ_E < 20%

7.8.2 Radiation Induced Noise (RIN)

It is important to control the noise induced by neutron flux similar to the one expected while running in Mu2e. In May 2016 crystals from Siccas, ISMA and Optomaterials have been tested with thermal neutrons at the HOTNES facility at ENEA-Frascati: a single crystal, coupled to a photomultiplier with a gain of 2.1×10^6 at 1400 V, has been inserted inside the Am B source[48] and thus irradiated with a uniform flux of 700 n cm $^{-2}$s^{-1}, the dark current values are recorded by means of an automatic acquisition program.The experimental setup is shown in Figure 7.37. A typical measurement took

Figure 7.37: *Experimental setup used to determine crystal RIN.*

place in three different steps: we have measured the dark current of the crystal outside the source for ∼5 minutes, then, continuing dark current monitoring, the crystal has been irradiated with the source for 15 minutes and finally current recording continued for 15 minutes after the extraction to check the crystal decay time. To evaluate the radiation induced noise we are interested in measuring F that is the radiation induced number of phoelectrons/s/neutron flux and the radiation induced noise (RIN), the first one is defined as:

$$F = \frac{\frac{I}{e\times G_{PMT}}}{\phi_N} \tag{7.15}$$

To evaluate the noise expected for the Mu2e experiment we considered a gate of 200 ns and an extimate flux of 10^4 n/cm^2/s, that is the number of collected photoelectrons

is defined as:

$$N_{p.e} = F \times \phi_{Mu2e} \times 200 \text{ ns} \tag{7.16}$$

Knowing now the number of collected photoelectrons, the RIN can be obtained using the following relation:

$$RIN = \frac{\sqrt{N_{p.e.}}}{LY} \tag{7.17}$$

Results obtained are reported in Table 7.4 and Figure 7.38 an example of signals from crystal sold by different vendors are reported. The value of the current increase

Crystal	LY [$N_{p.e.}$/MeV]	I[μA]	F[$N_{p.e.}$/s/flux]	$N_{p.e.}$	RIN_{Mu2e} [keV]
ISMA 02	103	7.16	3.02×10^4	60.3	75.4
ISMA 12	103	4.61	1.94×10^4	38.9	60.5
ISMA 20	103	5.35	2.25×10^4	45.1	65.2
ISMA 21	103	7.28	3.07×10^4	61.4	76.0
SICCAS 1	129	6.83	2.88×10^4	57.5	58.6
SICCAS 2	126	7.58	3.19×10^4	63.8	63.4
SICCAS 4	136	10.1	4.27×10^4	85.5	67.8
OPTOM 2	93	7.65	3.22×10^4	64.4	86.3

Table 7.4: *Results from RIN test at HOTNESS Facility.*

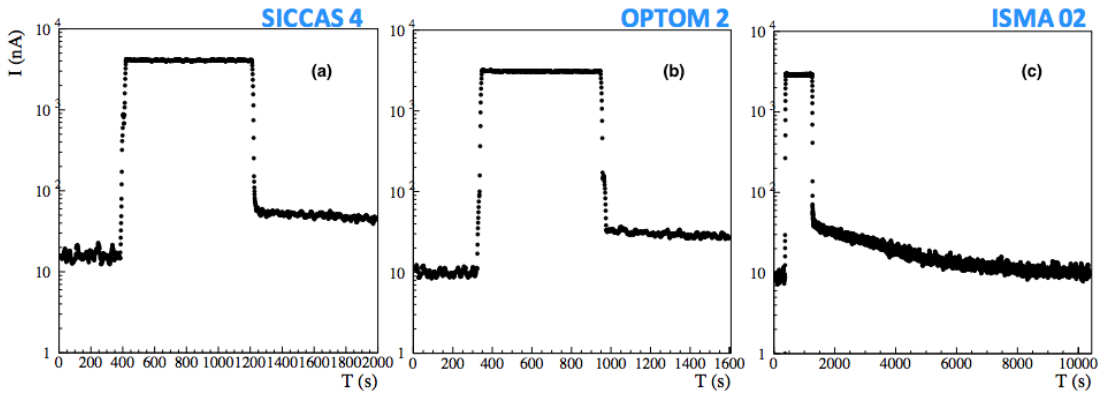

Figure 7.38: *Signal from SICCAS (a), Optomaterials (b) and ISMA (c) crystal under test to evaluate the radiation induced noise.*

from $I_{dark} \sim 10$ nA while the crystal is not irradiated to $I_{neutrons} \sim \mathcal{O}(10)$ μA. All the crystals tested showed a similar behavior and the RIN values obtained, that is between 60-85 keV for a flux of f 10^4 n/cm^2/s, meet the Mu2e requirement of a RIN<0.6 MeV.

Conclusions

The Mu2e experiment, thanks to its peculiar state of the art Superconducting Magnetic System and to the possibility of exploiting an intense and pulsed negative muon beam, aims at improving of four orders of magnitude the present limit on rate of the muon conversion in the field of a nucleus. The study of this process would allow, in combination with results from the MEG-II experiment, to discriminate between several New Physics scenarios. A CLFV signal observation would be a clear evidence for New Physics.

The electromagnetic calorimeter plays a crucial role in the Mu2e experiment, since it has been demonstrated that a calorimeter with a 5% energy resolution and 500 ps timing resolution can provide the needed rejection power to reduce background from muons and antiprotons, mimicking a conversion electron, to the level required by the experiment. The calorimeter improves also the tracker reconstruction efficiency. It will work in a high rate environment with a delivered dose of 5 krad/year and a neutron fluence of 10^{12} n/cm^2 in the innermost rings of the calorimeter while residing in a region with 1 T axial magnetic field and in 10^{-4} Torr vacuum.

The calorimeter design and the choice of the crystal and of the coupled photosensor has been settled. It is composed of two annular disks made of ~ 700 undoped CsI crystals readout by two "Mu2e SiPMs", each consisting in a parallel of two series made of three 6×6 mm^2 UV-extended SiPMs.

Several tests on the SiPM have been performed: after having measured the $I_{dark} - V$ curves and determined the breakdown voltage, the gain of six SiPM from Hamamatsu has been measured by exploiting the possibility to use the SiPM as a photon-counter. The experimental results are in good agreement with data-sheet that is a gain $\sim 1.7 \times 10^6$ at operation voltage. Indeed the gain values obtained ranges between 1.68×10^6 and 1.74×10^6. Moreover, spread of the gain, dark current and operation voltage meet the Mu2e experiment requirements.

A neutron irradiation test has been performed at HZDR Zentrum in Dresden with neutrons up to $\sim 6 \times 10^{11}$ n$_{1\ MeV}$/cm ^{2} to measure the variation of the SiPM leakage current and the its response to an UV Led. The SiPM response decreased of about a

factor of two and its current varied from 60 μA up to 12 mA. By studying the current dependency with temperature variations, it was shown that it is needed to maintain the SiPMs at 0°C.
Moreover, a test to study the performances of a SiPM series made of two not-irradiated SiPM and the SiPM irradiated in Dresden has been performed comparing this series with one made of three not-irradiated SiPMs. The results demonstrated that the presence of the irradiated SiPM does not affect drastically the device performances. A study of the SiPM Mean Time to Failure has also been performed.
Tests on the crystals were performed as well, regarding light response and radiation hardness. In particular, the crystal light output characteristics from different vendors have been tested using a ^{22}Na source. Almost all crystals pass the specification, that is a Light Yield (LY) >100 p.e./MeV, a Longitudinal Response Uniformity (LRU)< 5% and an energy resolution < 20%. Concerning crystal radiation hardness a test has been carried out at the HOTNES facility (ENEA-Frascati) to quantify the Radiation Induced Noise (RIN) from thermal neutrons, obtaining 58.6< RIN < 86.3 keV at the Mu2e expected fluence. The latter results show that the RIN is lower that the one fixed as maximum limit by the Mu2e requirements (RIN < 0.6 MeV).

Bibliography

[1] Altarelli, Guido. "The standard model of particle physics." arXiv preprint hep-ph/0510281 (2005).

[2] G. Aad, et al. "Observation of a new particle in the search for the Standard Model Higgs boson with the ATLAS detector at the LHC." Physics Letters B 716.1 (2012): 1-29.

[3] S. Chatrchyan, et al. "Observation of a new boson at a mass of 125 GeV with the CMS experiment at the LHC." Physics Letters B 716.1 (2012): 30-61.

[4] Fukuda, Y., et al. "Evidence for oscillation of atmospheric neutrinos." Physical Review Letters 81.8 (1998): 1562.

[5] A. de Gouvea, and P. Vogel. "Lepton flavor and number conservation, and physics beyond the standard model." Progress in Particle and Nuclear Physics 71 (2013): 75-92.

[6] Bertl, W., et al. "A search for muon to electron conversion in muonic gold." The European Physical Journal C-Particles and Fields 47.2 (2006): 337-346.

[7] Calibbi, L., et al. "Status of supersymmetric type-I seesaw in SO (10) inspired models." Journal of High Energy Physics 1211 (2012). JHEP, 1211:040, 2012.

[8] Harnik, R., Kopp, J., Zupan, J. ”Flavor violating Higgs decays”. arXiv preprint arXiv:1209.1397 (2012).

[9] Blanke, M., et al. "FCNC processes in the littlest Higgs model with T-parity: an update." arXiv preprint arXiv:0906.5454 (2009).

[10] Arnold, J. M., Bartosz, F., and Wise, M.B. "Phenomenology of scalar leptoquarks." Physical Review D 88.3 (2013): 035009.

[11] Lee, C. H., Dev, P. B., Mohapatra, R. N. ." Natural TeV-scale left-right seesaw mechanism for neutrinos and experimental tests". Physical Review D, 88(9), 093010.

[12] D. Measday, "The Physics of Muon Capture"s, Physics Reports 354, 243-409 (2001).

[13] T. Suzuki et al.,"Total nuclear capture rates for negative muons" ,Phys. Rev. C35, 2212 (1987).

[14] R. Kitano, M. Koike,Y. Okada, "Detailed calculation of lepton flavor violating muon-electron conversion rate for various nuclei." Phys. Rev. D 66, 096002 (9 2002).

[15] A. Czarnecki, X. Garcia i Tormo, W. Marciano, "Muon decay in orbit: Spectrum of high-energy electrons". Phys. Rev. D 84, 013006 (1 2011).

[16] W. Bertl et al. "A search for $\mu-e$ conversion in muonic gold". EPJ C, 47(2):337?346, 2006

[17] F. Renga, "Latest results of MEG and status of MEG-II."arXiv preprint arXiv:1410.4705 (2014).

[18] J. Adam et al. " The MEG detector for $\mu \rightarrow e\gamma$ decay search". Eur. Phys. J. C 73, 2365 (2013).

[19] Y. Kuno and Y. Okada. "Muon decay and physics beyond the standard model". Rev. Mod. Phys, 73:151-202, 2001

[20] A.M. Baldini et al. "Search for the lepton flavour violating decay$mu^+ \ rightarrow \ mathrme^+\gamma$ with the full dataset of the MEG experiment." The European Physical Journal C 76.8 (2016): 434.

[21] A.M. Baldini et al. "MEG Upgrade Proposal". Paul Scherrer Institute Research Committee, 2013.

[22] Comet collaboration, "Technical Design Report",2014

[23] L. Bartoszek et al. "Mu2e Technical Design Report". Fermi National Accelerator Laboratory, 2014

[24] P.Murat, G. Pezzullo. Mu2e Track Momentum Resolution: Understanding the High Side Tail. *Mu2eDocDB 5304-v7*,2015

[25] B. Lewandowski. “The BaBar electromagnetic calorimeter”. Nucl. Instrum. Meth., A494(1-3):303 -307, 2002. Proc. 8th International Conference on Instrumentation for Colliding Beam Physics.

[26] R. Ehrlich.“ Update on the cosmic background simulation”. Mu2e DocDB,4184, 2013.

[27] P. Murat. “Calorimeter-based Particle identification Mu2e”. Document 4256.

[28] G. Pezzullo and S. R. Soleti.“ Antiproton induced background rejection by means of the calorimeter PID”. Mu2e DocDB, 4709, 2014.

[29] R.-Y. Zhu, “Radiation damage in scintillating crystals”, Nucl. Inst. And Meth. A413 297 (1998).

[30] R.H. Mao, L.Y. Zhang and R.-Y. Zhu, “Gamma-Ray Induced Radiation Damage in Large Size LSO and LYSO Crystal”, IEEE Trans. Nucl. Sci. NS-54 1319 (2008).

[31] R. H. Mao, L. Y. Zhang and R.-Y. Zhu, “Effect of Neutron Irradiations in Various Crystal Samples of Large Size for Future Crystal Calorimeter”, Paper N32-4 in NSS 2009 Conference Record 2041 (2009).

[32] Filar optoMaterial s.r.l. http://www.filaroptomaterials.com/”.2016

[33] Institute for Scintillation Material. http://isma.kharkov.ua/eng/”.2016

[34] B. Saleh, University of Wisconsin, M. C.Teich, Columbia University, “Fundamentals of photonics”, Wiley Interscience (1991).

[35] “Datasheet Multi Pixel Photon Counter”, Hamamatsu Photonics k.k. (2008).

[36] S. Mattiazzo, “I rivelatori a silicio”,

[37] P.W. Cattaneo et al. “Development of High Precision Timing Counter Based on Plastic Scintillator with SiPM Readout”,arXiv:1402.1404v2, 2014.

[38] Hamamatsu, http://www.hamamatsu.com/us/en/index.html”.

[39] C. Xu, “Study of the Silicon Photomultipliers and Their Applications in Positron Emission Tomography”, PhD Dissertation, 2014

[40] G. Pezzullo and B. Echenard, “Study of the radiation dose and neutron flux on the calorimeter”, Mu2e-doc-2853.

[41] `https://srs.fbk.eu`

[42] G. Lindstrom, “Radiation Damage in Silicon Detectors”, NIM A512 (2003) 30.

[43] B.Seymour. “MTTF, Failrate, Reliability and life testing”. Burr-Brown Application Bulletin.

[44] (DOI 10.1109/NSSMIC 2013.6829584).

[45] K. K. Ng and S.M. Sze,“Physics of Semiconductor Devices", Wiley, 2006.

[46] M. J. Dean, et al. ,“Low Temperature Electronics", AcademicPress, 2001

[47] Shamgai SICCAS High Technology Corporation http://www.siccas.com/”

[48] M. Alessandroni, et al. “RAdiazione per l’INnovazione 2015”, results from the RAIN15 workshshop,2015.

Acknowledgements

First of all, I would like to express my sincere gratitude to my supervisor Dott. Stefano Miscetti for the continuous support, patience, motivation, and immense knowledge. His guidance helped me in all the time of my thesis.
My sincere thanks also goes to Prof. Fabrizio Petrucci and his very appreciated "pedantic" (:D) corrections, for always having supported me during all my academic career.

I would like to thank Marco and Ivano, for their insightful comments, encouragement and their knowledge. I hope they can pass down to me their talent to stay in lab. I'd like to thank all the LNF group: Raffa and all her precious advices, Simona and Fabio.

Thanks to Valentina, Marco and Riccardo, my dear friends, my little sunshines, this years without you would not have been so special.
Thanks to Marta for always saying to me "dai che sei forte".
Thanks to my beloved friend Adele, for all the time we spent together, for her ability of making things easier and for always saying the right things at the right moment.

Last but not least I would like to thank all my family. There are so many reason to thank all of them, but I have to mention their patience and immeasurable love

And as someone said "*fino a qui tutto bene*"...